# Final report for research project with title: Dynamics of Electrically-Induced Flow of Viscoelastic Fluids (grant number: PE8/906)

George Karapetsas and Vasilis Bontozoglou

July 28, 2015

## Contents

# 1 Summary

The interaction of an externally applied electric field with a liquid can give rise to interesting flow instabilities and pattern formation. For example, it has been demonstrated that the application of an electric field to an initially flat polymer-air or polymer-polymer interface may result in an electrohydrodynamic instability which leads to the formation of columnar structures. This phenomenon could be exploited in order to form well-controlled patterns at the microscale and nanoscale with many practical engineering applications. The scope of the present research project is to achieve fundamental understanding of the electrically-induced flow of viscoelastic liquid films and to investigate the effect of various factors (e.g. the complex fluid rheology, the presence of surface active materials or free charge along the liquid-air or liquid-liquid interfaces, geometric configuration, etc) that may play an important role in such a process.

It is well known that the dynamics and stability of liquid films can be very rich and it is characteristic that despite the fact that the first attempts to address the stability of a simple system such as a clean (without surfactants) Newtonian liquid film under the effect of gravity appear in the literature in the late 50's full understanding of the underlying mechanisms was not achieved until recently. One of the goals of the present study was to expand our understanding on the stability of the liquid films in the presence of surface active materials (surfactants). The reason for this is threefold. On one hand, the interaction of a surfactant-ladden film with an electric field is of interest for controlled pattern formation at the micro- and nano-scale. For example, ionic surfactants may interact with the electric field thereby affecting interfacial concentration and imposing specific patterns in the liquid. On the other hand, surfactants attribute non-Newtonian properties to the liquid, because the free surface attains surface elasticity and surface viscosity. Also, at high surfactant concentrations, micelles may form in the bulk and complicate its rheological behavior, rendering the solution viscoelastic. Finally, the governing equation that describes the conservation of surfactant concentration along the interface is identical to the equation that describes the conservation of free charge in the case of dielectric materials. These systems share many similar characteristics and it is possible to draw conclusions from the analogy between them. To this end, we formulated the Orr-Sommerfeld equation for a surfactant-laden film with appropriate boundary conditions, and solved it numerically for arbitrary disturbances and analytically for long-wave disturbances. The results from our analysis demonstrate the significant effect of surfactant solubility and sorption kinetics on the stability characteristics and provided useful insight in the non-linear dynamics of the flow. The results from this this work have been published to the Journal of Fluid Mechanics. In a subsequent paper that has also been submitted for publication to the Journal of Fluid Mechanics we have investigated the role of surfactants on the mechanism of the long-wave instability in liquid film flows. We have also made announcements to several local and international conferences.

A second goal of this research project was to develop a robust numerical

algorithm capable of handling the flow of viscoelastic material with large interfacial deformations. To account for the viscoelastic effects the constitutive model of choice was the Phan-Thien and Tanner (PTT), considerably more sophisticated than the linear models often used in the literature, which is based on network theory. This differential model can predict normal stresses, a finite extensional viscosity which is extensional hardening with increasing extension rate followed by either a constant extensional viscosity, in the linear version of the model, or extensional thinning in its exponential version and shear thinning. All these effects are observed in the majority of viscoelastic fluids. One of our aims was to make as less assumptions as possible, e.g. to avoid the use of lubrication approximation often encountered in the literature, in order to describe the flow dynamics as accurately as possible. To this end, we solve the governing equations numerically in 2D and we discretize the momentum and continuity equations using the finite element/Galerkin method while the constitutive equation for the stresses are discretized using the streamline upwind PetrovGalerkin (SUPG) method. This scheme has been combined with an elliptic grid generator which is able to follow the large deformations of the flow domain in time. This algorithm has been tested against standard benchmark problems (e.g. the steady viscoelastic extrusion flow) and was proven very robust for single fluid systems; as a side product we also examined the stability of this system and this work has been submitted for publication in the Journal of Non-Newtonian Fluid Mechanics. In order to include the effect of the electric field and the presence of a second phase (i.e. to study the system of two liquids sandwiched between to electrodes or a single liquid under air) we extended our numerical algorithm by introducing two discrete physical domains (one for each phase) fully taking into account the presence of a liquid-liquid interface and the discontinuity that arises in the stress field and the electric displacement (in the presence of free charge along the interface) between the two phases. The development of such an algorithm is very important not only for the purposes of this research project since it can also be used to study a wide variety of two phase flows with numerous industrial and scientific applications. The code has been validated against standard benchmark problems for case with and without the presence of electric fields.

Using the numerical code that has been developed, we have carried out an extensive parametric analysis to determine the effects of the various geometric and rheological parameters on the evolution of the interface and on the fabrication limits of this process. We studied the flow of both Newtonian and viscoelastic films under the action of homogeneous or heterogeneous electric fields imposed by the presence of either flat or patterned electrodes. Attention was focused on the non-linear dynamics of the flow, and it was interrogated in particular how the dynamics is influenced by the rheological characteristics of the material and how in turn it affects the fabrication limits of this process. We have shown that a metastable state of finite amplitude interfacial deformation is possible before eventually the perturbations grow until they reach the top electrode; during the late stages of the flow a coarsening process also takes place. Our non-linear simulations provide a better agreement with experimental observations for the

amplitude of the pseudo-steady state in comparison to the earlier predictions of linear theory.

We have shown that under the influence of a patterned electrode the effect of elasticity is more involved than what is suggested by linear theory for the case of an homogeneous electric field. We find that shear polymeric stresses are destabilizing at early times, as predicted by linear theory, but become stabilizing at later stages of the flow. Normal stresses, on the other hand, become increasingly important as the liquid-air interface deforms, destabilizing the film. Most of the research studies in the literature make use of the lubrication theory which typically neglects the presence of normal stresses. However, we were able to show that at late times normal stresses become dominant and cannot be ignored for the accurate prediction of the flow dynamics, rendering the lubrication approximation invalid. We also found that the fabrication limit on the period of the electrode protrusions appears to depend on the elasticity of the material, contrary to the predictions of linear theory of a constant most dangerous wavelength in the case of a flat electrode (homogeneous electric field). this indicates that for the proper design of suitable mask electrodes and in general for the optimization of the fabrication process, it is important to take into account the material elasticity. Finally, the amplitude of the pseudo-steady interfacial deformations appears to be unaffected by the elasticity of the material and the same is also true for the critical voltage below which these metastable states arise. The results of this work have been published in the Journal of Non-Newtonian Fluid Mechanics and we have also made announcements to several local and international conferences.

Another part of our study was devoted to the study of the electrohydrodynamic instability in a system of a trilayer of liquids. The first step of our work was to develop an efficient numerical algorithm which is capable of simulating multiple-phase flows of Newtonian or viscoelastic liquids inside a channel. To this end, we developed a numerical code able to handle an arbitrary number of phases which was validated against work previously published in the literature. We perform a parametric study to investigate the effect of surface tension, applied voltage, the various rheological parameters such as the viscosity ratios and elasticity of the materials and the various geometry characteristics of the electrodes various rheological parameters. In the case of flat electrodes (homogeneous electric field), it has been found that viscoelasticity has a rather weak effect even for high values of the Wi number (up to 10) and does not play an important role in the deformation of the liquid-air and liquid-liquid interface. We have also considered the case of patterned electrodes and this work is still under progress. Preliminary results of this work have been presented at the 67th Annual Meeting of the APS Division of Fluid Dynamics in San Fransisco, USA.

Finally, in order to study the three dimensional structures often seen in experiments, it was found to be necessary to develop a different numerical algorithm than the one described above, due to computational restrictions in 3D configuration imposed by the use of a sharp interface model. In the literature it has been shown that often in the case of 3D multiphase flows it is more ef-

ficient to use a phase field model instead. Therefore, we have developed a 3D model Navier-Stokes/Cahn-Hilliard (NS/CH) solver for the simulation of two-phase flows in the presence of electric fields. We verified the accuracy of our numerical code against standard benchmark tests for multiphase flows and also compared against the two-dimensional (2d) results for two-phase flow of Newtonian film in the presence of a spatially periodic electric field using the previous sharp-interface approach. In order to improve the efficiency of the present 2d/3d diffuse interface model, the implementation of multigrid solvers, parallelization (MPI, OpenMP), and adaptive mesh refinement have been implemented. A full parametric study of the 3D problem is already under way and the outcome of this work will be published in an international peer-reviewed journal.

In summary the work that has been done within the frame of this research project resulted in the following publications in peer-reviewed international journals:

- G. Karapetsas and V. Bontozoglou, Non-linear dynamics of a viscoelastic film subjected to a spatially periodic electric field J. Non-Newtonian Fluid Mech. 217 (2015) 113
- G. Karapetsas and V. Bontozoglou, The role of surfactants on the mechanism of the long-wave instability in liquid film flows, J. Fluid Mech. 741 (2014) 139-155
- G. Karapetsas and V. Bontozoglou, The primary instability of falling films in the presence of soluble surfactants, J. Fluid Mech. 729 (2013) 123-150
- G. Karapetsas and V. Bontozoglou, Non-linear dynamics of electric field instabilities in liquid trilayers. to be submitted for publication
- C. Dritselis, G. Karapetsas and V. Bontozoglou, Development of Navier-Stokes/Cahn-Hilliard (NS/CH) solver for the simulation of two-phase flows in the presence of electric fields. to be submitted for publication
- D. Pettas, G. Karapetsas, Y. Dimakopoulos and J. Tsamopoulos, On the origin of extrusion instabilities: linear stability analysis of the viscoelastic die swell, accepted for publication in J. Non-Newt Fluid Mech.
- G. Karapetsas and J. Tsamopoulos, On the stick-slip flow from slit and cylindrical dies of a Phan-Thien and Tanner fluid model . II. Linear stability analysis, Phys. Fluids 25 (2013), 093105

the following papers published in conference proceedings:

- G. Karapetsas and V. Bontozoglou, Non-linear evolution of a viscoelastic film under the influence of DC and AC electric fields, 10th Panhellenic Scientific Chemical Engineering Congress, June 2015, Patras, Greece
- D. Pettas, G. Karapetsas, Y. Dimakopoulos and J. Tsamopoulos, Linear stability analysis of the viscoelastic extrusion flow from a planar die, 10th

Panhellenic Scientific Chemical Engineering Congress, June 2015, Patras, Greece

- G. Karapetsas and V. Bontozoglou Non linear evolution of the electrohydrodynamic instability of a Newtonian or viscoelastic film under a spatially periodic electric field FLOW 2014, December 2014, Athens, Greece

- D. Pettas, G. Karapetsas, Y. Dimakopoulos and J. Tsamopoulos Linear stability of the viscoelastic extrusion flow from a slit die FLOW 2014, December 2014, Athens, Greece

and the following announcements in international conferences

- G. Karapetsas and V. Bontozoglou, Non-linear dynamics of viscoelastic liquid trilayers subjected to an electric field, 67th Annual Meeting of the APS Division of Fluid Dynamics, November 2014, San Francisco, USA

- C. Dritselis, G. Karapetsas and V. Bontozoglou, Non-linear dynamics of viscous bilayers subjected to an electric field: 3D phase field simulations, 67th Annual Meeting of the APS Division of Fluid Dynamics, November 2014, San Francisco, USA

- G. Karapetsas and V. Bontozoglou, Non-linear dynamics of the electrohydrodynamic patterning of viscoelastic materials EFMC10 European Fluid Mechanics Conference, September 2014, Copenhagen, Denmark

- G. Karapetsas and V. Bontozoglou, The effect of soluble surfactants on the linear stability of liquid film flow EFMC10 - European Fluid Mechanics Conference, September 2014,Copenhagen, Denmark

- G. Karapetsas and V. Bontozoglou, A numerical study of electrohydrodynamic patterning of viscoelastic materials, 7th Conference of the International Marangoni Association, June 2014, Vienna, Austria

- G. Karapetsas and V. Bontozoglou, The primary instability of falling films in the presence of soluble surfactants, 10th HSTAM 2013 International Congress on Mechanics, 25-27 May 2013, Chania, Greece

- G. Karapetsas and V. Bontozoglou, Linear stability of falling films in the presence of soluble surfactants, 27th Conference of European Colloid and Interface Society, 1-6 September 2013, Sofia, Bulgaria

- G. Karapetsas and V. Bontozoglou, The stabilizing mechanism of surfactants in falling films, 66th Annual Meeting of the APS Division of Fluid Dynamics, 24-26 November 2013, Pittsburgh, Pennsylvania, USA

- G. Karapetsas and J. Tsamopoulos, Linear stability analysis of the stick-slip flow of a viscoelastic fluid following the Phan-Thien Tanner model, 66th Annual Meeting of the APS Division of Fluid Dynamics, 24-26 November 2013, Pittsburgh, Pennsylvania, USA

- G. Karapetsas and V. Bontozoglou, Dynamics of a surfactant-laden falling film, International Focus Workshop: Multiscale Complex Fluid Flows and Interfacial Phenomena, 29 October-1 November 2012, Dresden, Germany

- A. Georgantaki, G. Karapetsas and V. Bontozoglou, Dynamics of an inclined film in the presence of soluble surfactants, 65th Annual Meeting of the APS Division of Fluid Dynamics, 18-20 November 2012, San Diego, California, USA

# 2 Flow stability of liquid films in the presence of surface-active materials

## 2.1 Introduction

The stability of liquid films has attracted the interest of many researchers in the past because of their importance in a broad range of engineering applications. Extensive reviews on the rich dynamics of this system and main developments on the field are given in [1, 2, 3, 4]. Predictions of the critical Reynolds number for the onset of waves on a clean liquid film (without surfactant) were first provided by [5] and [6], but a full understanding of the physical mechanism responsible for this long-wave instability was achieved much later [7, 8], by extending an argument originally proposed by [9]. It is notable that an unequivocal experimental confirmation of the linear prediction was also significantly delayed [10], and that an unexpected strong effect of the channel width was reported very recently by [11] and [12].

It is well known that interfacial instabilities can be significantly affected by the presence of surface-active materials or surfactants (see for example [13, 14]). Wave formation in falling films is no exception and this has been known since the ancient times. Early experimental studies (e.g. see [15, 16, 17]) showed that the addition of even small amounts of surfactants can have a stabilizing influence on the flow, dampening the waves that would otherwise arise on a falling liquid film. The first attempts to investigate the mechanisms that are responsible for the stabilization of the flow were made by [18] and [19] following different routes. [18] treated the liquid-air interface as a two-dimensional Newtonian fluid and examined the effect of various surface properties such as the surface viscosity, surface elasticity and diffusion of surfactant at the interface from the bulk. He presented numerical solutions of the Orr-Sommerfeld equation, albeit using approximate boundary conditions, and concluded that elasticity, which was due to surface tension gradients, was responsible for the stabilization of the liquid film flowing down a vertical wall below a critical value of the Reynolds number, in contrast to the case of clean liquids where the flow is unstable at all Reynolds numbers. [20] and [21] later presented a perturbation solution of the same problem in the limit of small wavenumbers. [19], on the other hand, considered the interface as a 2D viscoelastic fluid and presented an analytical solution of the Orr-Sommerfeld equation assuming long-wave disturbances. Despite the

significant differences between the two approaches, in the case of an insoluble surfactant the analytical prediction was found to be exactly the same, providing a unambiguous confirmation that the elasticity is the mechanism responsible for the stabilization of the flow. The asymptotic analysis for large values of the elasticity parameter by [22] confirmed the findings of the previous works about the existence of a critical Reynolds number and also showed that the presence of surfactants results in the decrease of the growth rate and increase of the wave length of the most unstable mode.

The theoretical results by [18] also suggested that the wave velocity should increase with increasing elasticity of the interface. However, the experimental work of [23] indicated that the free surface velocity actually decreases for increased surfactant concentration and this was later confirmed experimentally and theoretically by [24]. The latter work also noted that surface velocity depends strongly on the surface elasticity and is only mildly affected by surfactant diffusivity and interfacial mass transport.

More recently the linear stability for vertical film flows with diffusion to the surface and desorption of the surfactant to the gas phase was also examined by [25]. They were mostly interested in cases where surface instabilities could be enhanced by the presence of surfactants and for the purposes of their analysis, they have chosen to ignore the kinetics of adsorption and assumed that there is equilibrium at the interface. Enhancement of instability was also shown by [26] to be possible under conditions for evaporating thin films in the presence of non-volatile soluble surfactants. [27] used lubrication theory to derive a reduced order model and examined the linear stability of a similar system taking into account the sorption kinetics at the interface. They were able to recognise four new Marangoni-driven modes and it was shown that the observed modes depend significantly on the sorption kinetics and much less on the equation of state for surface tension.

The effect of insoluble surfactants on the linear stability of a film flowing down a corrugated wall in the limit of vanishing Reynolds number was examined by [28]. Subsequently, [29] presented a numerical solution of the Orr-Sommerfeld eigenvalue problem for finite Reynolds numbers of a film laden with insoluble surfactant flowing on an inclined plane and demonstrated the occurrence of the usual interfacial mode along with a new mode associated to the spatial variation of the surfactant concentration, while the mechanism responsible for the modified instability was investigated by [30, 31]. The same problem was also studied by [32] who presented a systematic analysis of the Orr-Sommerfeld problem of the full Navier-Stokes and concentration equations and also investigated the non-linear dynamics in the unstable regime.

Despite the large number of studies on the role of surfactants on film flows and the fact that this is a very old problem, it appears from the above review that the effects of surfactant solubility and adsorption/desorption kinetics on the primary instability and on the unstable dynamics have not yet been adequately addressed. In addition, there is recent experimental activity that points to a non-trivial influence of these parameters. For example, [33] performed a series of experiments on inclined film flows to study the role of different agents that may

have an important effect on the interfacial tension of water. For the purposes of their study, Georgantaki *et al.* used aqueous solutions of Isopropanol (IP) and Sodium Dodecyl Sulfate (SDS) and found that these two agents exhibit a remarkably different influence on the flow. More specifically, it was shown that, in the case of IP solutions, the inlet disturbances turned into solitary humps preceded by capillary ripples, as would be expected for a clean fluid with similar surface tension as the IP solution. On the contrary, when SDS solutions were used, the dominant structures were sinusoidal travelling waves of small amplitude. These structures were found to be extremely stable for a wide range of frequencies and up to high Reynolds numbers. Also, with respect to the primary instability, the same authors observed a strong stabilization of water films by the addition of small amounts of SDS, whereas previous results with IP solutions [11] had shown no difference in the critical Reynolds number from that of other clear liquids with the same Kapitza number (the definition of $Ka$ is given in section 3 below).

Substances IP and SDS have very different properties, and in a sense represent two extreme examples of soluble agents that modify the surface properties of water. IP is very soluble and decreases significantly the surface tension of its solutions. However, it does not show any particular affinity for the liquid-air interface, and thus may not formally be classified as a surfactant. In contrast, SDS exhibits strong partitioning between the liquid-air interface and the bulk. The behavior of these two agents brackets a whole range of additives that are moderately soluble and show an increasing affinity for the interface, and a theoretical treatment that recovers both limits is evidently welcome. The mechanisms that are responsible for the transition from the behavior of IP to that of SDS are not fully understood, and it is speculated that they may be an outcome of the different solubility and/or sorption kinetics.

The scope of our study is to examine in detail the linear stability of a film laden with a non-volatile, soluble surfactant and to reveal the role of a surfactant of arbitrary solubility in the initiating and the growth mechanism of the long-wave instability in liquid film flow. To this end we perform a systematic analysis of the Orr-Sommerfeld eigenvalue problem of the full Navier-Stokes and concentration equations, taking into account mass exchange by diffusion and convection between the bulk and the interfaces, as well as the effect of sorption kinetics along the liquid-air interface and along the substrate. We focus on surfactant concentrations below CMC and as a result, we ignore possible effects of intrinsic surface viscosity [34], which might be non-negligible at higher concentrations.

## 2.2 The primary instability of surfactant-laden films

### 2.2.1 Problem formulation

We consider the dynamics of liquid films flowing along an infinite planar wall, inclined at an angle $\alpha$ with the horizontal plane (see Fig. 1). The film is laden with a soluble, non-volatile surfactant which may adsorb at the liquid-air in-

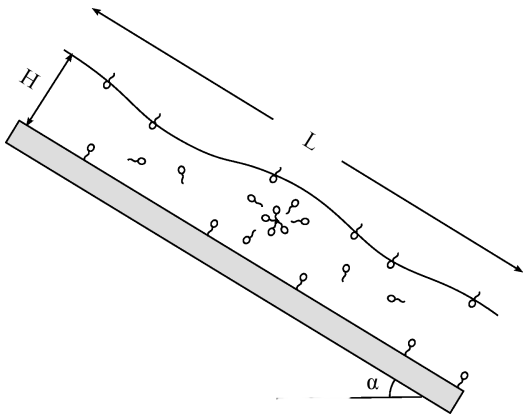


Figure 1: Schematic of a falling film in the presence of soluble surfactants

terface altering the surface tension, or it can exist in the bulk in the form of monomers or it may adsorb at the liquid-solid interface. The fluid is Newtonian with density $\rho$, kinematic viscosity $\nu$ and surface tension $\sigma$; the density and kinematic viscosity are considered constant whereas the surface tension depends on the interfacial concentration of the surfactant.

In order to model two-dimensional dynamics, we use a Cartesian coordinate system $(x, z)$, with $x$ pointing in the streamwise and $z$ in the cross-stream direction. The velocity field is $\mathbf{u} = (u, w)$, where $u$ and $w$ are the velocity components in the streamwise and the cross-stream direction. The liquid-air interface is located at $z = h(x, t)$ and the liquid-solid interface at $z = 0$. The flow is incompressible and governed by the momentum and mass conservation equations, given below:

$$\mathbf{u}_t + \mathbf{u} \cdot \nabla \mathbf{u} + \frac{1}{\rho} \nabla p - \nu \nabla^2 \mathbf{u} - \mathbf{g} = 0, \tag{1}$$

$$\nabla \cdot \mathbf{u} = 0, \tag{2}$$

where $p$ is the pressure, $\nabla$ is the gradient operator and $\mathbf{g} = g(\sin\alpha, -\cos\alpha)$. Unless stated otherwise, the subscripts denote partial differentiation with respect to $x$, $z$ and time $t$.

Solutions of (1) and (2) are obtained subject to the following boundary conditions: Along the free surface, the velocity field satisfies the local force balance between normal and viscous stresses in the liquid. Taking the components of this force balance tangential and normal to the free surface ($z = h(x, t)$) we obtain

$$\mathbf{n} \cdot \tau \cdot \mathbf{t} = \mathbf{t} \cdot \nabla_s \sigma, \tag{3}$$

$$\mathbf{n} \cdot \tau \cdot \mathbf{n} = -p_{air} + 2\kappa\sigma, \tag{4}$$

where $\mathbf{n} = (-h_x, 1)/(1 + h_x^2)^{1/2}$ and $\mathbf{t} = (1, h_x)/(1 + h_x^2)^{1/2}$ denote respectively the outward unit normal and unit tangential vectors on the interface; $2\kappa$ is

the mean curvature of the free surface and $\nabla_s$ is the surface gradient operator, defined as

$$2\kappa = -\nabla_s \cdot \mathbf{n},\ \nabla_s = (I - \mathbf{nn}) \cdot \nabla, \tag{5}$$

and $\tau$ is the total stress tensor,

$$\tau = -pI + \rho\nu \left( \nabla \mathbf{u} + (\nabla \mathbf{u})^T \right), \tag{6}$$

where $I$ is the identity tensor.

In addition, along the moving interface ($z = h(x,t)$) we impose the kinematic boundary condition,

$$h_t + uh_x = w. \tag{7}$$

At the liquid-solid interface ($z = 0$), the usual no-slip, no-penetration conditions are imposed,

$$u = 0,\ w = 0. \tag{8}$$

To account for the presence of soluble surfactants, we utilize the surfactant kinetic model of [35] and [36, 37] that allows in general for two surfactant species in the bulk (monomers and micelle aggregates) and one at each interface. For the present study we consider surfactant concentrations below the critical micelle concentration and thereby we will not account for the presence of micelles but will only consider monomers that may live in the bulk with concentration, $c$. The concentrations of surfactant adsorbed at the liquid-air and liquid-solid interface are denoted respectively by $c_a$ and $c_s$, and they are connected to the local bulk concentration of monomer according to the following kinetic laws

$$S_a + c \underset{k_2}{\overset{k_1}{\rightleftharpoons}} c_a, \tag{9}$$

and

$$S_s + c \underset{k_4}{\overset{k_3}{\rightleftharpoons}} c_s. \tag{10}$$

The terms $S_i$ ($i = a, s$ for the interface and the substrate) represent the fraction of the respective area that is not covered with monomer, and is thus available for adsorption. They are defined as

$$S_i = 1 - \frac{c_i}{c_{i\infty}}\ (i = a, s), \tag{11}$$

where $c_{i\infty}$ ($i = a, s$) are respectively the surfactant concentrations at the liquid-air interface and at the substrate at maximum packing. Note that each "reaction" used for this model is characterized by a rate constant $k_i$, with $i = 1, 2, 3, 4$. The limitation set by the above kinetic laws on the amount of monomer that can be adsorbed at each boundary leads to Langmuir adsorption isotherms [38]. Indeed, equating adsorption and desorption rates, and taking $c$ as the bulk concentration close to the respective interface, we obtain the following expressions for the interfacial concentrations

$$\frac{c_a}{c_{a\infty}} = \frac{c}{c + (k_2 c_{a\infty}/k_1)}\ , \quad \frac{c_s}{c_{s\infty}} = \frac{c}{c + (k_4 c_{s\infty}/k_3)}. \tag{12}$$

In the general case away from equilibrium, we use the above kinetic laws to generate the following fluxes that determine how the surfactant transfers between the different phases:

$$J_{ba} = k_1 c|_{z=h} \left(1 - \frac{c_a}{c_{a\infty}}\right) - k_2 c_a, \tag{13}$$

$$J_{bs} = k_3 c|_{z=0} \left(1 - \frac{c_s}{c_{s\infty}}\right) - k_4 c_s, \tag{14}$$

where $J_{ba}$ and $J_{bs}$ denote the flux of monomers from bulk to liquid-air and liquid-solid interface, respectively.

The behaviour of the various surfactant species is modelled by the following advection-diffusion equations:

$$c_{a,t} + \nabla_s \cdot (\mathbf{u}_s c_a) + c_a \left(\nabla_s \cdot \mathbf{n}\right)(\mathbf{u} \cdot \mathbf{n}) = D_a \nabla_s^2 c_a + J_{ba}, \tag{15}$$

$$c_t + \mathbf{u} \cdot \nabla c = D_b \nabla^2 c, \tag{16}$$

$$c_{s,t} = D_s \nabla_s^2 c_s + J_{bs}, \tag{17}$$

where $\mathbf{u}_s$ is the tangential velocity at the interface defined as $\mathbf{u}_s = (I - \mathbf{nn}) \cdot \mathbf{u}$ and $D_i$ $(i = a, b, s)$ denote the diffusion coefficients of the monomers at the liquid-air interface, in the bulk and at the substrate, respectively.

For the monomers in the bulk we apply the following boundary conditions along the interface and the substrate

$$J_{ba} = -D_b \left(\mathbf{n} \cdot \nabla c\right)_{z=h}, \tag{18}$$

$$J_{bs} = -D_b \left(\mathbf{n} \cdot \nabla c\right)_{z=0}. \tag{19}$$

To complete the description, a constitutive equation that describes the dependence of the interfacial tension on the surfactant concentrations is required. To this end, we use the Sheludko equation of state [39, 40]:

$$\sigma = \sigma_c \left(1 + \frac{c_a}{c_{a\infty}} \left[\left(\frac{\sigma_c}{\sigma_m}\right)^{1/3} - 1\right]\right)^{-3}, \tag{20}$$

where $\sigma_c$ and $\sigma_m$ are the surface tensions of a surfactant-free fluid and that of maximal surfactant concentration, respectively. This model is nonlinear and asymptotes to a minimal surface tension, $\sigma_m$, at high concentrations of adsorbed surfactant, which makes it appropriate for use at high surfactant concentrations, approaching the critical micelle concentration.

The total mass of the surfactant added to the liquid film per unit width, $M_{tot}$, is a conserved quantity, given by

$$\int_0^L \int_0^h c \, dz dx + \int_0^L c_a dx + \int_0^L c_s dx = M_{tot}, \tag{21}$$

where $L$ is the length of the falling film.

### 2.2.2 Scaling

The governing equations and boundary conditions are made dimensionless, using the following scalings:

$$\begin{gathered}(\tilde{x},\tilde{z})=(x,z)/H,\ \tilde{h}=h/H,\ \tilde{t}=tU/H,\ \tilde{\mathbf{u}}=\mathbf{u}/U,\\ p=p_{air}+\rho gH\sin\alpha\tilde{p},\ (\tilde{c}_a,\tilde{c}_s,\tilde{c})=\left(\frac{c_a}{c_{a\infty}},\frac{c_s}{c_{s\infty}},\frac{c}{c_{cmc}}\right),\\ \left(\tilde{J}_{ba},\tilde{J}_{bs}\right)=\left(\frac{J_{ba}}{c_{a\infty}},\frac{J_{bs}}{c_{s\infty}}\right)\frac{H}{U},\ \tilde{\sigma}=\frac{\sigma}{\sigma_c},\ \tilde{M}_{tot}=\frac{M_{tot}}{HLc_{cmc}},\end{gathered}\tag{22}$$

where $H=(3\nu Q/(g\sin\alpha))^{1/3}$ is the height of the Nusselt flat film, Q is the imposed flow rate, $U$ is the corresponding interfacial velocity, $U=gH^2\sin\alpha/(2\nu)$, and $c_{cmc}$ is the critical micelle concentration. The tildes denote dimensionless variables and are henceforth suppressed. Using this scaling, three dimensionless numbers emerge, the Reynolds, Weber and surface Peclet number, respectively

$$Re=\frac{\chi}{2}\sin\alpha,\ We=\frac{Ka}{\chi^{2/3}\sin\alpha},\ Pe_i=ReSc_i\ (i=a,s,b,m),\tag{23}$$

where

$$\chi=\frac{gH^3}{\nu^2},\ Ka=\frac{\sigma_c}{\rho g^{1/3}\nu^{4/3}},\ Sc_i=\frac{\nu}{D_i}(i=a,b,s),\tag{24}$$

correspond to a modified Reynolds number, the Kapitza number and the Schmidt number, respectively. The parametrization shown in Eq. (24) is advantageous for the study of our system since the modified Reynolds number, $\chi$, is the only parameter in Eq. (24) that depends on the film height, which is a measure of the flow rate, whereas $Ka$ and $Sc_i$ $(i=a,b,s)$ depend only on material properties. For a given liquid and surfactant the only free parameters are $\chi$ and $\alpha$ while the rest remain constant. This is very useful for our parametric study, and thus parametrization according to Eq. (24) is preferred over that of Eq. (23), and will be used extensively in the discussion of the results.

Substitution of these scalings into the momentum and mass conservation governing equations yields

$$Re(u_t+uu_x+wu_z)+2p_x-u_{xx}-u_{zz}-2=0,\tag{25}$$

$$Re(w_t+uw_x+ww_z)+2p_z-w_{xx}-w_{zz}+2\cot\alpha=0,\tag{26}$$

$$u_x+w_z=0.\tag{27}$$

The behaviour of the surfactant monomers in the bulk is governed by the following dimensionless equations

$$c_t+uc_x+wc_z=Pe_b^{-1}(c_{xx}+c_{zz}).\tag{28}$$

The above set of equations are subject to the following boundary equations along the interface $(z=h(x,t))$

$$-4u_xh_x+(u_z+w_x)(1-h_x^2)=2We\ \sigma_x\sqrt{1+h_x^2},\tag{29}$$

$$p + \frac{u_x(1-h_x^2) + (u_z + w_x)h_x}{1+h_x^2} = -We\,\sigma \frac{h_{xx}}{(1+h_x^2)^{3/2}}, \tag{30}$$

$$h_t + uh_x = w, \tag{31}$$

$$\begin{aligned} c_{a,t} + uc_{a,x} + \frac{c_a}{1+h_x^2}\left[(u_x + h_x w_x) + h_x(u_z + h_x w_z)\right] = \\ = \frac{1}{Pe_{ca}\sqrt{1+h_x^2}}\left[\frac{c_{a,x}}{\sqrt{1+h_x^2}}\right]_x + J_{ba}, \end{aligned} \tag{32}$$

$$\frac{h_x c_x - c_z}{Pe_b\sqrt{1+h_x^2}} = \beta_a J_{ba}, \tag{33}$$

and along the wall($z = 0$)

$$u = w = 0, \tag{34}$$

$$c_{s,t} = Pe_{cs}^{-1} c_{s,xx} + J_{bs}, \tag{35}$$

$$\frac{c_z}{Pe_b} = \beta_s J_{bs}. \tag{36}$$

The dimensionless expressions for the fluxes are shown below

$$J_{ba} = k_a\left(R_a c|_{z=h}\,(1-c_a) - c_a\right), \tag{37}$$

$$J_{bs} = k_s\left(R_s c|_{z=0}\,(1-c_s) - c_s\right), \tag{38}$$

where the dimensionless parameters $\beta_i$, $k_i$ and $R_i$ $(i = a, s)$ are given by

$$\beta_a = \frac{c_{a\infty}}{Hc_{cmc}},\ \beta_s = \frac{c_{s\infty}}{Hc_{cmc}}, \tag{39}$$

$$k_a = \frac{k_2 H}{U},\ k_s = \frac{k_4 H}{U},\ R_a = \frac{k_1 c_{cmc}}{k_2 c_{a\infty}},\ R_s = \frac{k_3 c_{cmc}}{k_4 c_{s\infty}}. \tag{40}$$

The dimensionless form of the Sheludko equation of state for the surface tension is given by

$$\sigma = \left[1 + c_a\left(\Sigma^{1/3} - 1\right)\right]^{-3}, \tag{41}$$

where $\Sigma = \sigma_c/\sigma_m$. One additional dimensionless parameter will appear in the next section, as a result of the linearization of the equation of state around to base flow. This parameter, the surface elasticity, $E_o$, is related to the derivative of surface tension along the interface (Eq. (29)) and is formally defined by Eq. (66).

At this point, it is instructive to attach physical significance to the various dimensionless parameters just defined, and to draw attention to the ones that will be used more extensively in the discussion of the results. Terms $\beta_i$ $(i = a, s)$ are ratios of maximum total amounts of surfactant in the different phases. More specifically, they compare the maximum amount that can adsorb on each boundary to the maximum amount that can reside in the bulk as monomer. Terms $R_i$ $(i = a, s)$ are ratios of the maximum possible forward and backward

reaction rates for each of the adsorption processes. Their physical significance is further clarified by considering local equilibrium: For example, setting the flux in Eq. (37) equal to zero, results in the expression $c_a = R_a c/(1 + R_a c)$. For $R_a \leq O(1)$, we observe that $c_a < 1$ even when $c = 1$, i.e. the interface remains unsaturated at the maximum possible concentration of monomer in the bulk (remember that $c$ is nondimensionalized with $c_{cmc}$, and $c_a$ with $c_{a\infty}$). On the contrary, for $R_a \gg O(1)$ the interface is practically saturated at bulk concentration well below the critical for the formation of micelles.

Parameters $\beta_i$ and $R_i$ may be combined as follows:

$$\xi_a = \beta_a R_a = \frac{k_1}{H k_2},\ \xi_s = \beta_s R_s = \frac{k_3}{H k_4}. \tag{42}$$

Terms $\xi_i$ $(i = a, s)$ are ratios of the kinetic constants of the forward and backward reaction for each interface-bulk interaction, and thus provide a direct measure of the surfactant solubility in the bulk liquid [41]. For example, $\xi_a << 1$ signifies a highly soluble surfactant, whereas for $\xi_a >> 1$ the surfactant is virtually insoluble and is trapped at the interface. We note that most of the recent theoretical literature refers to insoluble surfactants, and thus $\xi_a >> 1$ is a useful limit for comparisons.

We will be making extensive use of the solubilities, $\xi_i$, in what follows, because some important aspects of the system behavior are not dictated by the parameters $\beta_i$ and $R_i$ independently, but only by their combination $\beta_i R_i$. This is notably the case for the critical Reynolds number and for the concentration for maximum stability (see Eq. (84) and (90) below).

Finally, parameters $k_i$ $(i = a, s)$ are ratios of the time-scale of convection to the time-scale of each of the reverse reactions. For example, $k_a << 1$ means that the desorption reaction is slow compared to convection, and thus a temporary decrease of the bulk concentration near the interface will not lead to significant desorption. Similar comparison for the forward reaction (e.g. extent of adsorption resulting from a temporary local increase in the bulk concentration) is accomplished by the parameter $k_a \beta_a R_a = k_a \xi_a$. Thus, an asymmetry in the adsorption-desorption tendency may be dictated by the value of $\xi_a$, i.e. the solubility of the surfactant. For example, a sparingly soluble surfactant could have $k_a < 1$ and $k_a \xi_a > 1$, and as a result, a temporary decrease of the bulk concentration near the interface will not lead to significant desorption whereas a temporary increase will lead to significant adsorption.

### 2.2.3 Linear stability analysis

*2.2.3.1 Base state*

The set of dimensionless equations and boundary conditions, derived in the previous section, has a trivial solution corresponding to a flat film with uniform surfactant concentration. In the case of a clean fluid, this is also known as the Nusselt flat film solution and its dimensionless form is shown below

$$h_o = 1,\ u_o = 2z - z^2,\ w_o = 0,\ p_o = (1 - z)\cot\alpha. \tag{43}$$

In order for the above solution to remain valid when a soluble surfactant is present, the concentration of all the species should be uniform and at equilibrium

$$(c_a, c_s, c) = (c_{ao}, c_{so}, c_o), \tag{44}$$

where $c_{ao}, c_{so}, c_o$ denote the equilibrium values. The equilibrium surface tension of the liquid-air interface,

$$\sigma_o = \left[1 + c_{ao}\left(\Sigma^{1/3} - 1\right)\right]^{-3}, \tag{45}$$

is also uniform and any variation in concentration would result in surface tension gradients which would drive additional flows. At equilibrium the fluxes should be $J_{ba} = J_{bs} = 0$. Thus using Eq. (37) and (38) we get

$$c_{io} = \frac{R_i c_o}{1 + R_i c_o} \ (i = a, s). \tag{46}$$

We also know that the total mass of the surfactant is given by the following equation

$$c_o + \beta_a c_{ao} + \beta_s c_{so} = M_{tot}. \tag{47}$$

The above equation can be solved numerically with respect to $c_o$ for a given value of $M_{tot}$. Below, we have derived an analytical solution for $c_o$ and $c_{ao}$, assuming that there is no adsorption of surfactant at the substrate, $c_{so} = 0$

$$c_o = \frac{-1 - \xi_a + M_{tot}\,\xi_a/\beta_a + \sqrt{4M_{tot}\,\xi_a/\beta_a + \left(1 + \xi_a - M_{tot}\,\xi_a/\beta_a\right)^2}}{2\xi_a/\beta_a}, \tag{48}$$

$$c_{ao} = \frac{-1 - \xi_a + M_{tot}\,\xi_a/\beta_a + \sqrt{4M_{tot}\,\xi_a/\beta_a + \left(1 + \xi_a - M_{tot}\,\xi_a/\beta_a\right)^2}}{1 - \xi_a + M_{tot}\,\xi_a/\beta_a + \sqrt{4M_{tot}\,\xi_a/\beta_a + \left(1 + \xi_a - M_{tot}\,\xi_a/\beta_a\right)^2}}. \tag{49}$$

The above solution is shown graphically in Fig. 2 as a function of the solubility parameter $\xi_a$ and for various values of $\beta_a$ and $M_{tot}$. As expected, we find that for high values of $\xi_a$ (low solubility) most of the surfactant lives at the interface whereas for low values of $\xi_a$ (high solubility) it prefers to live in the bulk.

In the case of an insoluble surfactant, we simply take

$$c_{ao} = M'_{tot}, \tag{50}$$

where $M'_{tot} = M_{tot}/\beta_a$ and $c_o$ is equal to zero.

*2.2.3.2 Derivation of linearized equations and boundary conditions*

We perform a linear stability analysis by perturbing the flow around the Nusselt flat film solution. To this end we write all variables as the sum of the base state and a small perturbation

$$\phi = \phi_o + \overline{\phi}, \tag{51}$$

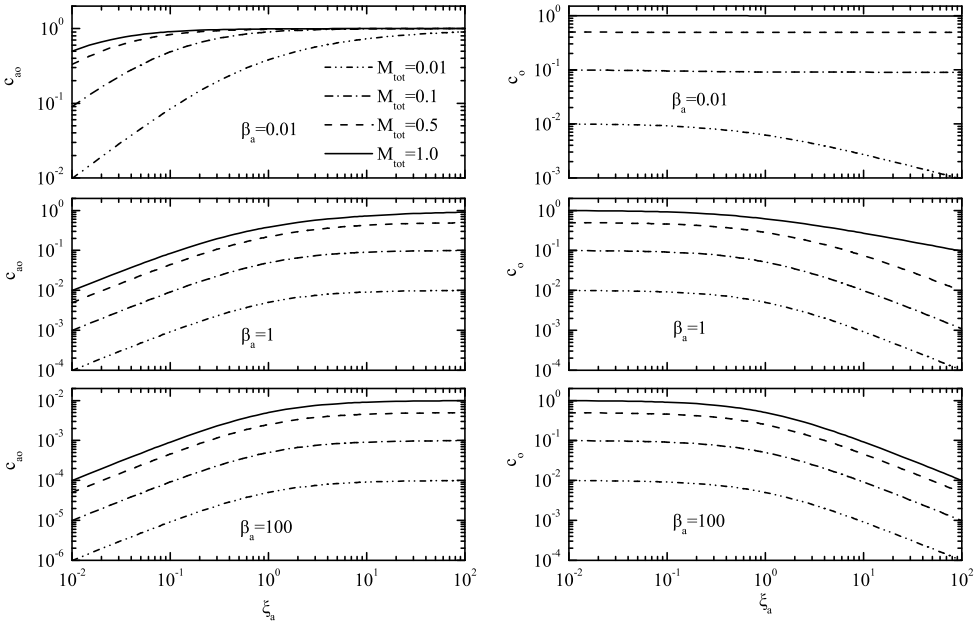


Figure 2: Dependence of monomer surfactant concentration at the interface (left) and in the bulk (right) on the parameter $\xi_a$ for various values of $\beta_a$ and $M_{tot}$. We assume that surfactant does not adsorb at the substrate ($\beta_s = R_s = 0$)

and linearize the governing equations assuming $\overline{\phi} << \phi_o$. We end up with the following linearized disturbance equations

$$Re(\overline{u}_t + \left(2z - z^2\right)\overline{u}_x + 2(1-z)\overline{w}) + 2\overline{p}_x - \overline{u}_{xx} - \overline{u}_{zz} = 0, \tag{52}$$

$$Re(\overline{w}_t + \left(2z - z^2\right)\overline{w}_x) + 2\overline{p}_z - \overline{w}_{xx} - \overline{w}_{zz} = 0, \tag{53}$$

$$\overline{u}_x + \overline{w}_z = 0, \tag{54}$$

$$\overline{c}_t + \left(2z - z^2\right)\overline{c}_x = Pe_b^{-1}(\overline{c}_{xx} + \overline{c}_{zz}), \tag{55}$$

and the following boundary conditions along the interface

$$-2\overline{h} + \overline{u}_z + \overline{w}_x = 2We\,\overline{\sigma}_x, \tag{56}$$

$$\overline{p} + \overline{u}_x - \overline{h}\cot\alpha = -We\,\overline{h}_{xx}\sigma_o, \tag{57}$$

$$\overline{h}_t + \overline{h}_x = \overline{w}, \tag{58}$$

$$\overline{c}_{a,t} + \overline{c}_{a,x} + c_{ao}\overline{u}_x = \frac{\overline{c}_{a,xx}}{Pe_{ca}} + \overline{J}_{ba}, \tag{59}$$

$$\frac{\overline{c}_z}{Pe_b} = -\beta_a\overline{J}_{ba}, \tag{60}$$

and along the wall

$$\overline{u} = \overline{w} = 0, \tag{61}$$

$$\overline{c}_{s,t} = \frac{\overline{c}_{s,xx}}{Pe_{cs}} + \overline{J}_{bs}, \tag{62}$$

$$\frac{\overline{c}_z}{Pe_b} = \beta_s\overline{J}_{bs}. \tag{63}$$

The linearized perturbation fluxes are shown below

$$\overline{J}_{ba} = k_a\left[R_a\left(\overline{c}|_{z=h}\left(1 - c_{ao}\right) - c_o\overline{c}_a\right) - \overline{c}_a\right], \tag{64}$$

$$\overline{J}_{bs} = k_s\left[R_s\left(\overline{c}|_{z=0}\left(1 - c_{so}\right) - c_o\overline{c}_s\right) - \overline{c}_s\right]. \tag{65}$$

It is worth noting the linearization of the equation of state for the surface tension around the base state, $\sigma - \sigma_o = (d\sigma/dc_a)_{c_{ao}}\,(c_a - c_{ao})$, or $\overline{\sigma} = (d\sigma/dc_a)_{c_{ao}}\,\overline{c}_a$. The above derivative may be reframed in terms of the definition of the dimensionless surface elasticity (scaled with surface tension of a clean fluid, $\sigma_c$), $E(c_a)$,

$$E_o = E(c_{ao}) = -\left(\frac{d\sigma}{d\,lnc_a}\right)_{c_{ao}} = -c_{ao}\left(\frac{d\sigma}{dc_a}\right)_{c_{ao}}, \tag{66}$$

so that perturbations in surface tension are replaced by perturbations in surface concentration:

$$\overline{\sigma} = -\frac{E_o}{c_{ao}}\,\overline{c}_a\,,\ \overline{\sigma}_x = -\frac{E_o}{c_{ao}}\,\overline{c}_{a,x}. \tag{67}$$

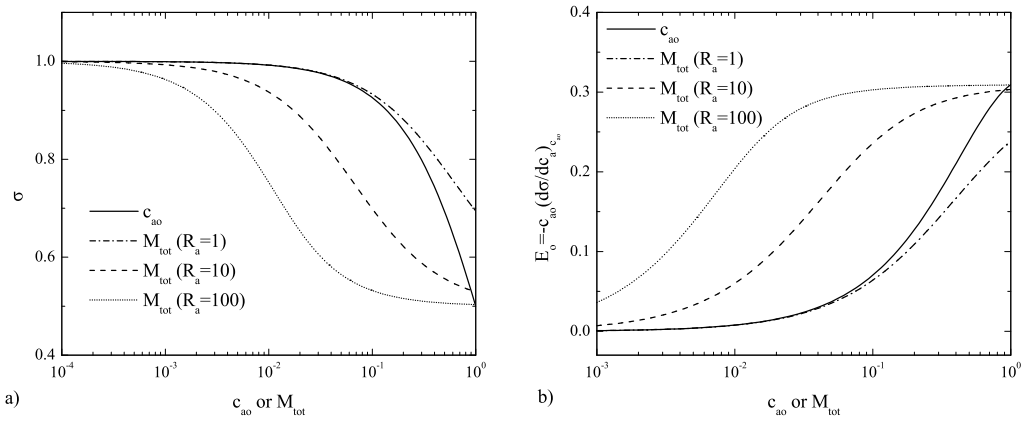


Figure 3: Dependence of surface tension and elasticity on the surfactant concentration for $\beta_a = 0.01$.

Using the dimensionless equation of state, surface elasticity is expressed in terms of the surface concentration by the expression,

$$E_o = \frac{3c_{ao}\left(\Sigma^{1/3}-1\right)}{\left[1+c_{ao}\left(\Sigma^{1/3}-1\right)\right]^4}. \tag{68}$$

Fig. 3 shows respectively the functions $\sigma(c_{ao})$ and $E(c_{ao})$ and their dependence on the interfacial concentration, $c_{ao}$, and the total amount of surfactant, $M_{tot}$. It is evident that the Sheludko equation of state exhibits a smooth approach to the limiting values for a clear and for a saturated interface, and that, in both these limits, the surface elasticity increases smoothly until it saturates for high amounts of surfactant.

The above set of equations is converted into the Orr-Sommerfeld problem of the linearized Navier-Stokes and concentration equations by introducing the following definition for the stream function

$$\overline{u} = \overline{\psi}_z,\ \overline{w} = -\overline{\psi}_x, \tag{69}$$

and seeking disturbances in the form of normal modes. To this end, we write all variables in the following way

$$\begin{pmatrix} \overline{\psi}(x,z,t) \\ \overline{c}(x,z,t) \\ \overline{c}_a(x,t) \\ \overline{c}_s(x,t) \end{pmatrix} = \begin{pmatrix} \Psi(z) \\ C(z) \\ C_a \\ C_s \end{pmatrix} exp(\lambda t + ikx), \tag{70}$$

and end up with the following set of equations

$$Re\left[\left(\lambda + ik\left(2z - z^2\right)\right)\left(\Psi_{zz} - k^2\Psi\right) + 2ik\Psi\right] = \Psi_{zzzz} - 2k^2\Psi_{zz} + k^4\Psi, \quad (71)$$

$$Pe_b\left[\lambda + ik\left(2z - z^2\right)\right]C = C_{zz} - k^2 C. \quad (72)$$

These equations are subject to the following boundary conditions along the interface

$$\begin{aligned}\Psi_{zzz} - 3k^2\Psi_z - Re(\lambda + ik)\Psi_z = \\ = ik\left[k^2 We\sigma_o + \cot\alpha\right]\left[\Psi_{zz} + k^2\Psi + 2ikWe\frac{E_o}{c_{ao}}C_a\right],\end{aligned} \quad (73)$$

$$(\lambda + ik)\left[\frac{1}{2}\left(\Psi_{zz} + k^2\Psi\right) + ikWe\frac{E_o}{c_{ao}}C_a\right] + ik\Psi = 0, \quad (74)$$

$$(\lambda + ik + \frac{k^2}{Pe_{ca}})C_a = -ikc_{ao}\Psi_z + k_a\left[R_a\left(C(1 - c_{ao}) - c_o C_a\right) - C_a\right], \quad (75)$$

$$\frac{C_z}{Pe_b} = -\beta_a k_a\left[R_a\left(C(1 - c_{ao}) - c_o C_a\right) - C_a\right], \quad (76)$$

and along the wall

$$\Psi_z = 0, \quad (77)$$

$$\Psi = 0, \quad (78)$$

$$(\lambda + \frac{k^2}{Pe_{cs}})C_s = k_s\left[R_s\left(C(1 - c_{so}) - c_o C_s\right) - C_s\right], \quad (79)$$

$$\frac{C_z}{Pe_b} = \beta_s k_s\left[R_s\left(C(1 - c_{so}) - c_o C_s\right) - C_s\right]. \quad (80)$$

For the case of an insoluble surfactant ($\xi_a >> 1$) that does not adsorb to the substrate, the above system readily reduces to the equations presented by [32].

*2.2.3.3 Analytic predictions by long-wave expansion*

For the case of a soluble surfactant and for no adsorption of the surfactant at the substrate, it is possible to perform a long-wave expansion of the above set of equation for $k \to 0$. To this end, we follow a similar procedure as in [32] and seek a solution of this form

$$\begin{pmatrix}\Psi \\ C \\ C_a\end{pmatrix} = \begin{pmatrix}\Psi^0 \\ C^0 \\ C_a^0\end{pmatrix}\lambda^0 + \begin{pmatrix}\Psi^1 \\ C^1 \\ C_a^1\end{pmatrix}\lambda^1 ik + \begin{pmatrix}\Psi^2 \\ C^2 \\ C_a^2\end{pmatrix}\lambda^2 k^2 + O(k^3). \quad (81)$$

Substituting in Eq. (71)-(80) and assuming $C_s = \beta_s = k_s = R_s = 0$, we expand the resulting equations in series of $k$ and derive the following expression for the eigenvalue of the most unstable mode

$$\lambda = -2ik + \left(\frac{8}{15}Re - 6Ma\frac{\xi_a(c_{ao} - 1)^2}{3\xi_a(c_{ao} - 1)^2 + 4} - \frac{2}{3}\cot\alpha\right)k^2, \quad (82)$$

where $Ma$ is the Marangoni number defined as

$$Ma = E_o We = -c_{ao} \left( \frac{d\sigma}{dc_a} \right)_{c_{ao}} We = \frac{3c_{ao} \left( \Sigma^{1/3} - 1 \right)}{\left[ 1 + c_{ao} \left( \Sigma^{1/3} - 1 \right) \right]^4} \frac{Ka}{\chi^{2/3} \sin \alpha}. \quad (83)$$

The imaginary part of Eq. (82) gives the expected result that long-wave disturbances travel with phase speed equal to twice the free surface velocity. The real part of (82) indicates that the onset of instability occurs when the coefficient of $k^2$ vanishes. Therefore the critical Reynolds number is given by the following expression

$$Re_c = \frac{5}{4} \cot \alpha + \frac{15}{4} Ma \frac{3\xi_a (c_{ao} - 1)^2}{3\xi_a (c_{ao} - 1)^2 + 4} \quad (84)$$

where $c_{ao}$ is given by Eq. (49). We note that Eq. (84) is implicit in $Re_c$ or $\chi_c$, because of the appearance of these dimensionless numbers in the definition of $Ma$ in Eq. (83). An explicit expression may be derived only for a vertical film, and is as follows:

$$\chi_c = 2\, Re_c = \left[ \frac{15}{2}\, E_o\, Ka\, \frac{3\xi_a (c_{ao} - 1)^2}{3\xi_a (c_{ao} - 1)^2 + 4} \right]^{3/5}. \quad (85)$$

In the limit of an insoluble surfactant ($\xi_a = \beta_a R_a >> 1$), Eq. (84) reduces to

$$Re_c = \frac{5}{4} \cot \alpha + \frac{15}{4} Ma \quad (86)$$

in agreement with the expression given by [32]. For a clear liquid, $Ma = 0$, both equations lead to $Re_c = (5/4) \cot \alpha$, the well known prediction for a Newtonian falling film [5, 6]. It is interesting to note that this prediction is also recovered in the limit of an interface saturated with a mildly soluble surfactant ($c_{a0} \to 1$, $\xi_a$ finite), as well as in the limit of a very soluble surfactant ($\xi_a << 1$). The latter prediction is in agreement with the data of [33], who performed experiments with the highly soluble Isopropanol and observed a behavior representative of a clear liquid with reduced surface tension.

*2.2.3.4 Numerical method for arbitrary wavelength*

The Orr-Sommerfeld eigenvalue problem, which consists of equations (71)-(80), cannot be solved analytically for arbitrary wavenumbers. The discretization of the governing equations is performed using a finite-element/Galerkin method, and we approximate all the variables through the use of quadratic Lagrangian basis functions $\phi_i$. Applying the divergence theorem, the weak form of the governing equations becomes

$$\int_0^1 \left[ \left[ Re \left[ \left( \lambda + ik \left( 2y - y^2 \right) \right) \left( \Phi_y - k^2 \Psi \right) + 2ik\Psi \right] + 2k^2 \Phi_y - k^4 \Psi \right] \phi_i + \right. \\ \left. + \Phi_y \frac{d\phi_i}{dy} \right] dy - \left[ \Phi_y \phi_i \right]_0^1 = 0, \quad (87)$$

$$\int_0^1 \left( \Phi\phi_i + \Psi_y \frac{d\phi_i}{dy} \right) dy - \left[ \Psi_y \phi_i \right]_0^1 = 0, \tag{88}$$

$$\int_0^1 \left[ \left( Pe_b \left[ \lambda + ik \left( 2y - y^2 \right) \right] + k^2 \right) C\phi_i + C_y \frac{d\phi_i}{dy} \right] dy - \left[ C_y \phi_i \right]_0^1 = 0. \tag{89}$$

Note that the fourth order partial differential equation for $\Psi$ has been decomposed into two second order differential equations by introducing a new variable, $\Phi = \Psi_{yy}$. At the edge nodes we impose the boundary conditions that are given by Eq. (73-80). The resulting system of algebraic equations is solved numerically with the help of the LAPACK library. The computational domain is discretized using 50 elements in all the computations presented in this paper; numerical checks showed that increasing the number of elements further led to negligible changes.

### 2.2.4 Discussion

*2.2.4.1 The hydrodynamic instability mode*

In the present section, we will examine the effect of various parameters contained in our model of a soluble surfactant. Thus, we will identify the range of physical phenomena that may be described by this model. In particular, we wish to set the present flow in perspective with the two limiting cases of (a) a clear liquid, and (b) a liquid doped with an insoluble surfactant. The latter appears to have attracted most of the attention in the recent theoretical literature on film flow with surfactants, and as a result the extent and significance of differences caused by surfactant solubility are presently unclear.

The effect of inertia on the stability of surfactant-laden falling films is demonstrated in Fig. 4. The values of parameters used are mentioned in the caption, and constitute a reasonable base case. In particular, we assume that the surfactant adsorbs only at the liquid-air interface and not on the solid substrate. Shown in Fig. 4 is the dispersion relation for increasing values of the modified Reynolds number, $\chi$. Beyond a certain threshold, $\chi_c$, the flow becomes unstable; below this threshold all modes are stable. For the case shown, the critical $\chi$ is equal to 3.74.

It is evident from Fig. 4 that the instability is a long-wave one, and that, for each unstable $\chi$, a wavenumber with maximum growth rate (the most dangerous mode) may be identified. The variation with $\chi$ of the wavenumber and the growth rate of the most dangerous mode at neutral stability is shown respectively for various inclinations in Fig. 5a,b. The conclusion that the instability is a long-wave one, magnifies the significance of the analytic result, Eq. (84). Thus, we will be making frequent use of it in the subsequent discussion. However, the behavior of higher wavenumbers is still very important, because these harmonics enter into mode interactions that dictate the non-linear evolution of the interface.

To further examine the effect of inclination angle, we present in Fig. 6a neutral stability curves for various inclinations. As expected the most unstable

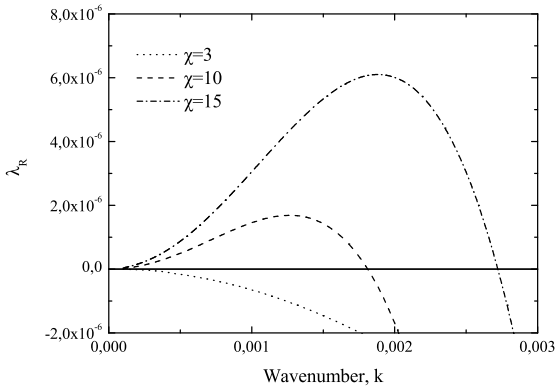


Figure 4: Dispersion curves for different values of $\chi$. The rest of the parameters are $\alpha = 90^o$, $Ka = 3000$, $\Sigma = 2$, $M_{tot} = 0.1$, $\beta_a = 0.01$, $R_a = 1$, $k_a = 0.01$, $\beta_s = R_s = k_s = 0$, $Sc_a = Sc_s = 100$ and $Sc_b = 10$.

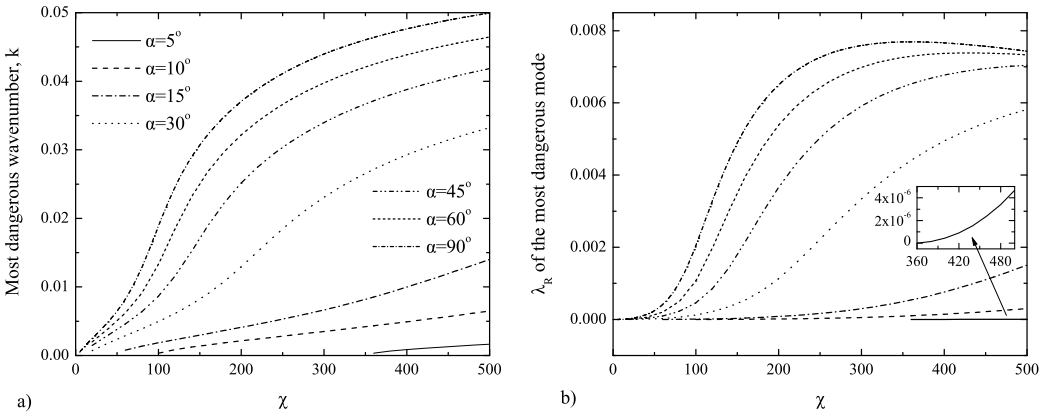


Figure 5: Dependence of a) the wavenumber and b) the growth rate of the most dangerous mode on $\chi$. The rest of the parameters remain the same as in Fig. 4.

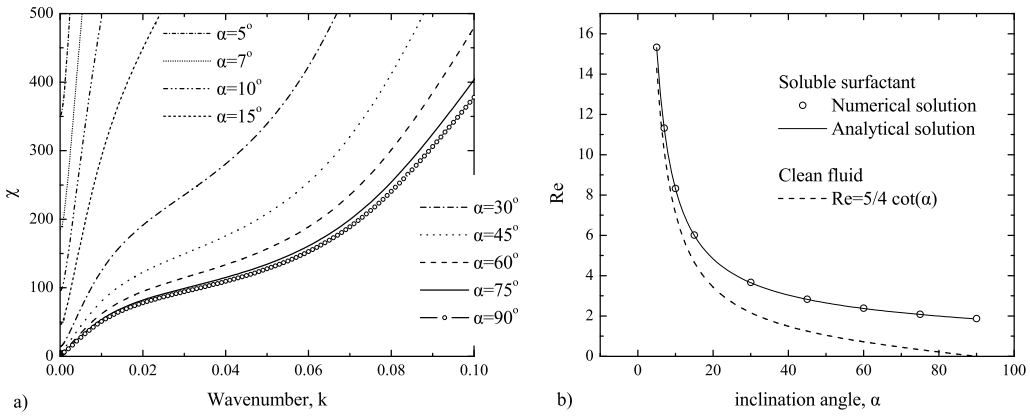


Figure 6: a) Neutral curves for various inclination angles b) Dependence of critical $Re$, on the inclination angle; comparison of analytical solution (Eq. 84) and numerical results for $k = 10^{-4}$. The rest of the parameters remain the same as in Fig. 4.

case is for $\alpha = 90^o$. For low values of $\alpha$ the flow remains stable up to rather high values of the modified Reynolds number, $\chi$, and the critical $\chi$ increases abruptly with decreasing wavelength of the perturbations. Fig. 6b presents the dependence of the critical $Re$, on inclination for $k = 10^{-4}$. The agreement with the analytical prediction, Eq. (84), serves as a check of the accuracy of the numerical solution. Also shown in Fig. 6b is the prediction for a clear liquid. With decreasing inclination, differences between the two liquids gradually decrease, because the term $(5/4)\cot\alpha$ grows in significance compared to the Marangoni correction. Thus, hitherto we concentrate on the most interesting case of a vertical film.

*2.2.4.2 Parametric behavior of the critical conditions*

We start by considering the critical conditions, which correspond to the onset of long-wave disturbances, i.e. $k \to 0$. A question of evident interest is the effect on stability of the total amount of surfactant contained per unit area of the channel. To this end, we present in Fig. 7a the critical $\chi_c$ as a function of $M_{tot}$, for three different values of the solubility parameter, $\xi_a$. The lines in this figure depict the analytical solution (Eq. 84) while the points depict the numerical solution which is in very good agreement with analytical solution testifying thus once again for its accuracy.

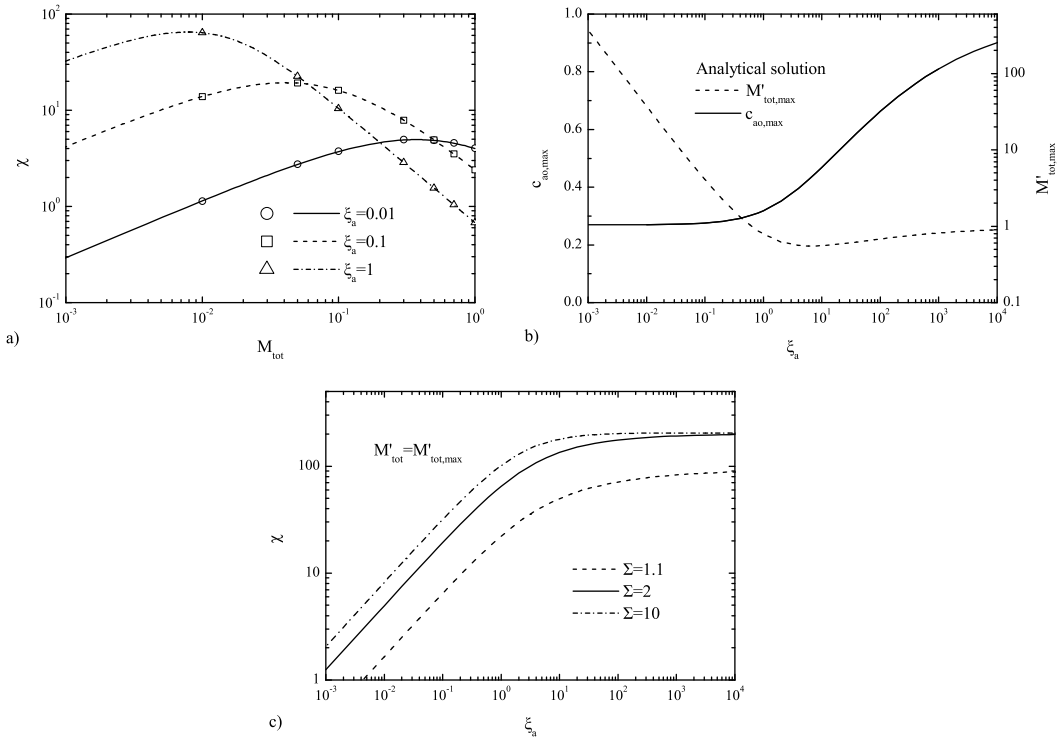


Figure 7: a) Dependence of critical $\chi$ on $M_{tot}$; comparison of analytical solution (Eq. 84) and numerical results for $\alpha = 90^o$, $\beta_a = 0.01$ and $k = 10^{-4}$. b) Evaluation of $M'_{tot,max}$ and $c_{ao,max}$ for maximum stability of the flow as function of $\xi_a$, using the analytical solution (Eq. 84) for $\alpha = 90^o$. c) Evaluation of $\chi_{c,max}$ for maximum stability of the flow as function of $\xi_a$, using the analytical solution (Eq. 84) for $\alpha = 90^o$. The rest of the parameters remain the same as in Fig. 4.

It is notable that the dependence on $M_{tot}$ is not monotonic, exhibiting maximum stabilization at an intermediate value $M_{tot,max}$, below the CMC. For very small, as well as for large values of $M_{tot}$, the critical $\chi_c$ approaches the limit of the clean fluid. This is somewhat counter-intuitive because one would expect that the more surfactant is present in the system the more stable the system would be. However, we should keep in mind that it is not the amount of surfactant that stabilizes the flow, but actually the Marangoni stresses, which are related to the elasticity of the interface. When the surfactant exhibits significant solubility, the behavior is further complicated because of two competing effects; with increasing amount of surfactant, the dimensionless elasticity, $E_o$, grows as depicted in Fig. 3. At the same time, the growth in bulk concentration provides higher driving force for mass transfer with the interface, leading to the attenuation of surface tension gradients. As a result, when the adsorbed surfactant at the liquid-air interface approaches saturation, surface tension gradients decrease and therefore the Marangoni effects become less significant. This is also reflected in Eq. (84) where the second term on the right hand side is proportional to $c_{ao}-1$; for an interface saturated with a soluble surfactant ($\xi_a$ not very large), the expression for the critical Reynolds reduces to the Newtonian limit.

The parametric variation of the curves in Fig. 7a with $\xi_a$ motivates investigation of two complementary issues: how does the location and how does the magnitude of the maximum in the critical conditions depend on surfactant solubility. Thus, in the following, we study $M_{tot,max}$ and $\chi_{c,max}$ as a function of $\xi_a$. Starting with the former, we note that the value of $M_{tot,max}$ can be easily determined by solving the equation $d\chi_c/dM_{tot}=0$, which for $\alpha=90^o$ and after some manipulation results in the following expression

$$8E_o+(c_{ao}-1)\left[3\xi_a(c_{ao}-1)^2+4\right]\frac{dE_o}{dc_{ao}}=0. \tag{90}$$

The solution of Eq. (90) provides the surface concentration, $c_{ao,max}$, that results in maximum stabilization, for a surfactant with solubility $\xi_a$. It is noteworthy that $c_{ao,max}$ depends solely on $\xi_a$, and not independently on $\beta_a$ and $R_a$. According to the model adopted for surface elasticity, (68), $E_o$ is a function of $c_{ao}$ and $\Sigma$, so Eq. (90) needs to be solved numerically.

The variation of the value of $c_{ao,max}$ with surfactant solubility is shown in Fig. 7b. For an insoluble surfactant ($\xi_a\to\infty$), the flow is most stable with a saturated interface ($c_{ao}\to 1$). This is readily explained by Eq. (86), in combination with the monotonic dependence of $E_o$ on $c_{ao}$. However, with increasing surfactant solubility, mass trasfer between the bulk and the interface (leading to attenuation of surface tension gradients) grows in significance, and, as a result, maximum stabilization is achieved at lower values of $c_{ao,max}$. For a highly soluble surfactant ($\xi_a\to 0$), the most stable interfacial concentration reaches a plateau $c_{ao,max}\approx 0.28$.

An alternative way of plotting the above result, also shown in Fig. 7b, is in terms of the rescaled total amount of surfactant, $M'_{tot,max}=M_{tot,max}/\beta_a$. This rescaling makes all data for different values of $\beta_a$ collapse on to the single curve

shown. We note that $M_{tot}$ and $M'_{tot}$ represent the total amount of surfactant, scaled respectively with the maximum capacity of the bulk and of the interface. An interesting observation from Fig. 7b is that the amount of surfactant, $M'_{tot,max}$, corresponding to $\chi_{c,max}$ is not a monotonic function of the solubility $\xi_a$; a minimum arises for moderate values of $\xi_a$, which indicates that optimum results may be achieved with smaller quantities of a slightly soluble surfactant than with an insoluble one.

The variation in the magnitude of the maximum, $\chi_{c,max}$, with surfactant solubility is shown in Fig. 7c for three different values of parameter $\Sigma$, which is a measure of the strength of the surfactant and its ability to decrease the surface tension of the liquid-air interface. We note that $\chi_{c,max}$ represents the optimum stabilization of the flow that can be achieved with surfactant of solubility $\xi_a$, and corresponds to the addition of amount $M_{tot,max}$. It is observed that, for soluble surfactants, $\chi_{c,max}$ increases with the decrease in solubility. However, below a moderate solubility, the curves reach an asymptotic limit, indicating that slightly soluble surfactants are equally efficient as insoluble ones.

An interesting observation from Fig. 7c is that there is a maximum stabilization that may be achieved, irrespective of the increase in $\Sigma$, which in the present case (and for $Ka = 3000$) is approximately $\chi_{c,max} \leq 200$. This conclusion depends on the specific model used for surface tension variation. The stability problem for insoluble surfactant and a vertical film may be solved analytically with the present model, and gives the result

$$\chi_{c,insoluble} = \left[ \left( \frac{45}{2} \right) Ka \frac{\Sigma^{1/3} - 1}{\left[ 1 + \left( \Sigma^{1/3} - 1 \right) \right]^4} \right]^{3/5} \quad \text{for } 1 < \Sigma < 64/27,$$
$$\text{and} \tag{91}$$
$$\chi_{c,insoluble} = \left( \frac{1215}{512} Ka \right)^{3/5} \quad \text{for } \Sigma > 64/27.$$

The above equation may be considered a special case of the general result for an insoluble surfactant ([18]; [22]),

$$\chi_{c,insoluble} = \left( \frac{15}{2} \, Ka \, E_o \right)^{3/5}. \tag{92}$$

The aforementioned discussion, and the observation that the curves in Fig. 7a intersect, indicates that, for a specific total amount of surfactant, the dependence of critical conditions on surfactant solubility may be non-monotonic. Indeed, Fig. 8a shows the critical $\chi$ as a function of $\xi_a$ for different values of $R_a$ and for $M_{tot} = 0.1$. In all shown cases, $\chi_c$ exhibits a strong maximum at moderate values of $\xi_a$. Therefore, for a specific amount of surfactant, the moderately soluble one appears more efficient in stabilizing the flow than the insoluble one. Fig. 8b shows again the dependence of critical $\chi$ on $\xi_a$, keeping now constant the value of $\beta_a$. For small values of $\beta_a$, we observe again a non-monotonic dependence, whereas for larger values of $\beta_a$ the critical $\chi$ reaches a plateau in the

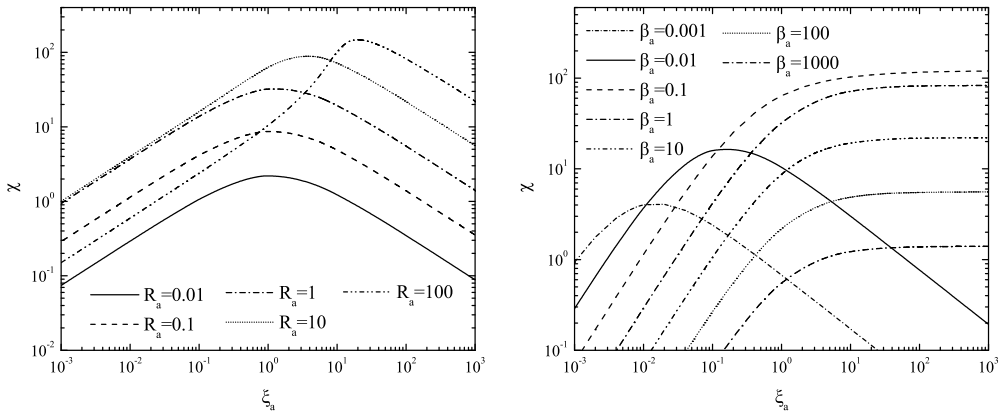


Figure 8: Dependence of critical value of $\chi$ on the solubility parameter $\xi_a$ as predicted by the analytical solution (Eq. 84) for different values of $R_a$ and for $\alpha = 90^o$, $M_{tot} = 0.1$. The rest of the parameters remain the same as in Fig. 4, except for $\beta_a$ in Fig. 8a which varies as $\xi_a/R_a$, and for $R_a$ in Fig. 8b which varies as $\xi_a/\beta_a$.

limit of high $\xi_a$. This should come as no surprise because for large values of $\beta_a$ the capacity of the interface to adsorb monomers is very large and for the specific value of $M_{tot}$ the resulting interfacial concentration is very small (see also Fig. 2). The non-monotonic behaviour is recovered again when considering higher values of $M_{tot}$.

*2.2.4.3 Parametric behavior for disturbances of finite wavelength*

Having analysed the limit $k \to 0$, we now focus on the behavior of disturbances of finite wavelength. The addition of one more lengthscale complicates significantly the dynamics. Among other effects, sorption kinetics -which is included in the modelling but did not appear in the limit of infinite wavelength- now becomes potentially important. Given the complexity of behavior, we first perform an extensive parametric study and describe the results purely phenomenologically. Then, we sketch the key physical mechanisms that we believe determine the dynamics, and attempt some qualitative comparisons with available experimental observations.

*2.2.4.3.1 Effect of the total amount of surfactant*

Figs. 9a,b show the critical modified Reynolds number, $\chi$, as function of disturbance wavenumber for different amounts of surfactant, $M_{tot}$. Fig. 9a is a magnification of Fig. 9b at small values of $\chi$ and $k$. It is evident that the addition of a small amount of surfactant results in drastic stabilization of practically all disturbances of finite length.

In the small wavenumber range, and with increasing amount of surfactant, the neutral curves in Fig. 9a,b tend to accumulate around a rough asymptote with slope $\approx 10^4$. The variation at higher wavenumbers is more complex, and eventually becomes non-monotonic. More specifically, an inflection point appears, which above $M_{tot} = 0.3$ leads to a local maximum in $\chi$; a possible mechanism for this behavior is described in section 2.2.4.4, below. Further increase in the amount of surfactant renders higher wavenumbers progressively less stable.

Fig. 9c presents the dispersion curves for the same values of $M_{tot}$ as in Fig. 9a,b, and for a specific value of $\chi = 50$. We observe that the addition of relatively small amounts of surfactant affects drastically the stability of the film, decreasing significantly the growth rate of the disturbances, as well as the range of the unstable modes. This result indicates that, in the presence of surfactants, instabilities will need considerably longer time to develop. The non-monotonic effect of $M_{tot}$ that was discussed in Fig. 7 is also apparent here. For the given value of $\chi$, the growth rate of the disturbances (and in particular the most dangerous one) decreases for small values of $M_{tot}$, reaches a minimum around $M_{tot} = 0.5$ and increases again for larger values of $M_{tot}$. Similar is also the behaviour of the wavenumbers of the most dangerous mode and of the cut-off.

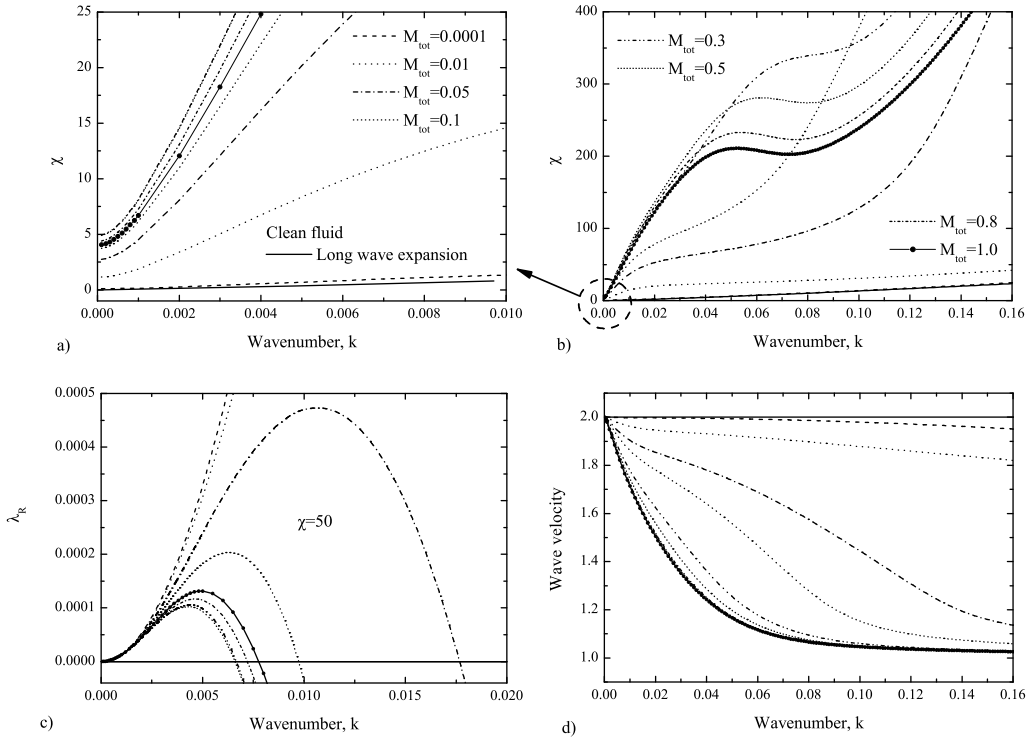


Figure 9: a) Neutral curves for different values of $M_{tot}$; comparison with analytical solution for a clean fluid ($Re_c = \frac{5}{4}(\cot\alpha + Wek^2)$ or equivalently $\chi_c = \frac{5}{2}(\cot\alpha + Wek^2)/\sin\alpha$). b) Zoom of Fig. 9a for $0 < k < 0.01$. c) Dispersion curves for different values of $M_{tot}$ and for $\chi = 50$. d) Wave velocity of the marginally unstable mode at neutral stability as a function of the wavenumber, $k$, for different values of $M_{tot}$. The rest of the parameters remain the same as in Fig. 4.

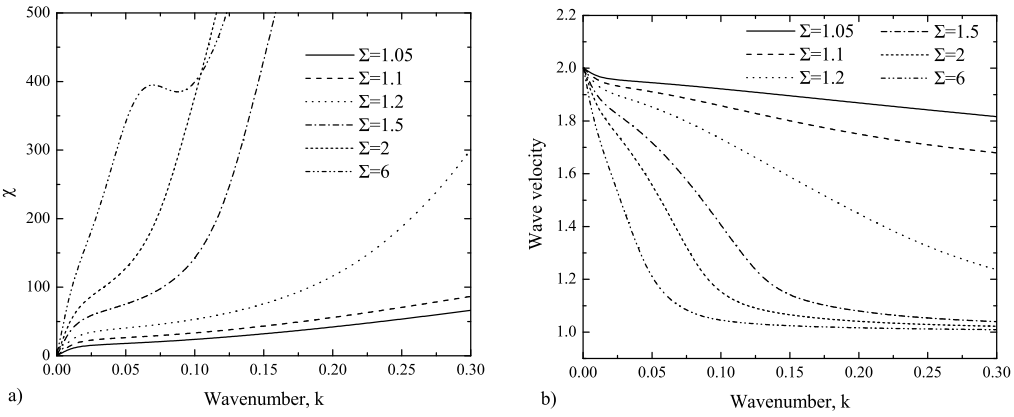


Figure 10: a) Neutral curves and b) dependence of the wave velocity on the wavenumber for different values of $\Sigma$. The rest of the parameters remain the same as in Fig. 4.

Finally, Fig. 9d presents the wave velocity of the marginally unstable mode at neutral stability as a function of the wavenumber and for different amounts of surfactant. In agreement with previous experimental and theoretical studies [23, 24], we find that the addition of surfactant decreases the wave velocity, and more so the higher the wavenumber. It is also notable that the variation with $M_{tot}$ is strictly monotonic, reaching an asymptotic limit for high surfactant concentrations. Therefore, the wave velocity appears to depend directly on the surface concentration of the soluble surfactant, and not on the surface elasticity, as determined by the combination of stretching and diffusion/convection, which was discussed extensively in relation to Fig. 7 and 8.

*2.2.4.3.2 Effect of surface tension and surfactant strength*

In Fig. 10a neutral curves are presented for various values of $\Sigma$ to examine the effect of Marangoni stresses. This parameter can be seen as a measure of the strength of the surfactant. Increasing $\Sigma$, while keeping $Ka$ (i.e. $\sigma_c$) constant means that the difference $\sigma_c - \sigma_m$ increases and therefore the surface tension gradients become stronger. The increase of the elasticity of the interface due to the induced Marangoni stresses stabilizes the flow and the critical $\chi_c$ increases. For low and moderate values of $\Sigma$, $\chi_c$ increases monotonically with the wavenumber of the disturbance. We find, though, that for large $\Sigma$ this is not always the case. Fig. 10b shows the phase velocity of the marginally unstable

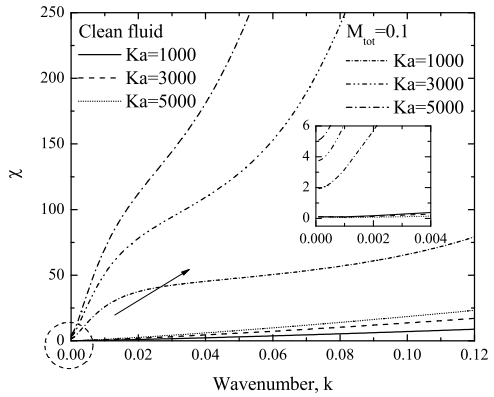


Figure 11: Neutral curves for different values of $Ka$. The rest of the parameters remain the same as in Fig. 4.

mode, and indicates that it decreases drastically with the increase of $\Sigma$. In combination with Fig. 9d, we conclude that the amount and the strength of the surfactant have a similar effect on the phase speed of the disturbances.

Fig. 11 shows the effect of Kapitza number for a surfactant-laden liquid, along with the corresponding neutral curves of a clean liquid. Though the values of $Ka$ plotted are high (and thus the effect of capillary forces on the stabilization of finite wavenumber disturbances in a clean liquid is significant), we note that, with the addition of surfactant, the critical $\chi$ rises by more than an order of magnitude. Another interesting observation is that the dependence of critical $\chi$ on $Ka$ persists even for $k = 0$ (see the insert of Fig. 11 for a zoom close to zero $k$), although it is well known that for a clean fluid and for $k = 0$ the critical Reynolds number is independent of $Ka$ ($Re_c = \frac{5}{4}\cot\alpha$). This observation is in agreement with the analytic result, see Eq. (84). One way to see why the value of $Ka$ has such a strong impact on the stability of the surfactant-laden flow is by considering that increasing Kapitza number is like increasing the surface tension of the clean fluid, $\sigma_c$. For a given value of $\Sigma$ (in our case $\Sigma = 2$) this would mean that the difference in surface tensions between a clean interface and a fully contaminated one would increase proportionally and therefore the Marangoni effects would become more important. This trend is in agreement with theoretical studies in the literature for insoluble surfactants [29, 32] where it was shown that the critical Reynolds number is proportional to the Marangoni number.

*2.2.4.3.3 Effect of surfactant solubility*

In Fig. 7 and 8, we have examined the role of surfactant solutility, $\xi_a$, in the limit $k \to 0$. Presently, we want to examine its effect for non-zero wavenumbers.

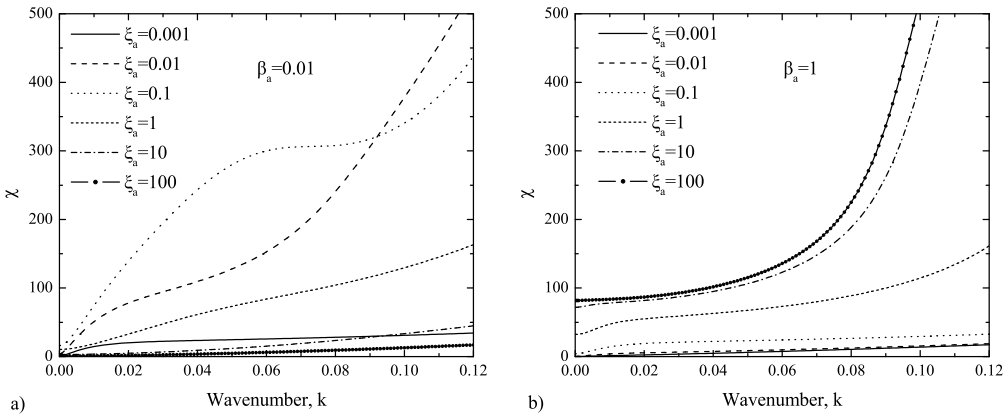


Figure 12: Neutral curves for different values of $\xi_a$ for a) $\beta_a = 0.01$ and b) $\beta_a = 1$. The rest of the parameters remain the same as in Fig. 4.

To this end, we keep constant the total amount of surfactant ($M_{tot} = 0.1$) and the value of $\beta_a$, which is a measure of the amount of surfactant that can be adsorbed at the interface, and vary the value of $\xi_a$ to examine the effect of surfactant solubility. For $\beta_a = 0.01$ (shown in Fig. 12a), the effect of $\xi_a$ on critical $\chi$ appears to be rather complex for finite wavelengths. More specifically, we observe that for the lowest value of $\xi_a = 0.001$ ($R_a = 0.1$), the critical $\chi$ remains fairly constant for a wide range of wavenumbers, apart from a small region close to $k = 0$. Increasing the value of $\xi_a$ to 0.01 ($R_a = 1$) the flow significantly stabilizes for short wavelength disturbances. Futher increase of $\xi_a$ may lead to situations where the system can be more stable to large wavelength disturbances and at the same time less stable to short wavelenths (e.g. compare neutral curves for $\xi_a = 0.01$ and $\xi_a = 0.1$). For even higher values of the solubility parameter, $\xi_a$, the critical $\chi$ decreases significantly and for the highest value of $\xi_a$ the system behaves as a clean liquid; the neutral curves for $\xi_a = 100$ and that of a clean fluid coincide, for the range of wavenumbers shown in the figure, but are not shown here for clarity. This happens because for $\xi_a = 100$ (and for the specific amount of surfactant, $M_{tot} = 0.1$) the interface becomes saturated with surfactant (see also Fig. 2) and therefore the induced surface tension gradients are not important; this result is in agreement with the predictions of our analytical expression in the limit of $k \to 0$ (see Eq. 84 and relevant discussion above). For $\beta_a = 1$ (shown in Fig. 12b) the picture is somewhat simpler, because the dependence of critical $\chi$ on $\xi_a$ is in this range monotonic. Nevertheless, we should note that the non-monotonic dependence is recovered again for higher values of $M_{tot}$.

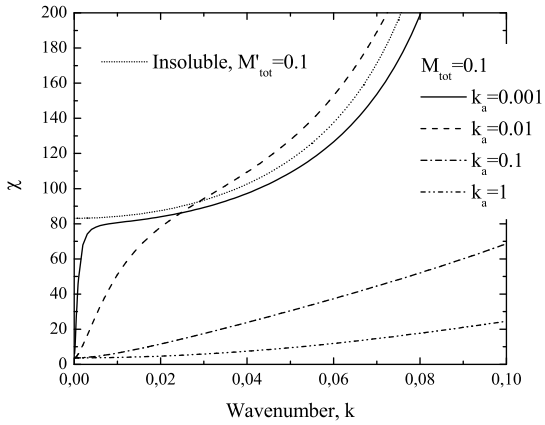


Figure 13: Neutral curves for different values of $k_a$. The rest of the parameters remain the same as in Fig. 4.

*2.2.4.3.4 Effect of sorption kinetics at the liquid-air interface*

Next, we consider the role of sorption kinetics at the liquid-air interface, which is potentially of central importance, and which has typically been neglected in simplified treatments of the problem. Thus, in Fig. 13 we examine the parametric effect of $k_a$ on the curves of neutral stability for the reference case of Fig. 4. It is expected that for long-wave perturbations ($k << 1$) the kinetics will not be very important because there will always be enough time for the different species to reach equilibrium around the interface. Indeed, as it can be seen in Fig. 13, for $k = 0$ the critical $\chi$ is the same for all values of $k_a$. This result is in direct agreement with the analytical expression that has been derived in the limit of $k \to 0$ (see Eq. 84), where there is no dependence of the critical $Re$ on the value of $k_a$.

However, we see that, for disturbances with larger wavenumbers, this is clearly not the case. In particular, we plot in Fig. 13 the result for an insoluble surfactant, and observe that, for the lowest value of $k_a$ shown, the neutral curve for the soluble surfactant follows it very closely, for all wavenumbers except for a very narrow range around zero. We should note at this point that to enable such a comparison between a soluble and an insoluble surfactant we have selected two cases with identical levels of interfacial concentration, $c_{ao}$. The similarity between the case of a soluble and an insoluble surfactant for large wavenumbers may be readily understood by considering that, when the kinetics are relatively slow and the disturbances have short wavelength, there will not be enough time for the species to approach equilibrium, and the system will behave as though the monomers that have been adsorbed at the liquid-air interface are isolated

from the monomers in the bulk. The general trend with faster kinetics is for the soluble surfactant to become less stabilizing than the insoluble one for all wavenumbers. It is noteworthy however that, there exists a range of moderate kinetics for which high-wavenumber disturbances are stabilized more efficiently with soluble than with the insoluble surfactant (see $k_a = 0.01$ and $k > 0.03$).

*2.2.4.3.5 Effect of surfactant adsorption at the solid substrate*

Next we examine how the adsorption of surfactant at the solid substrate may affect the stability of the flow. To this end, we vary the relevant parameters that control the behavior of the substrate. The effect of soprtion kinetics, $k_s$, is examined in Fig. 14a and shown to be negligible. On the contrary, the variation of $\beta_s$, which is shown in Fig. 14b, appears to have significant impact on the flow stability. These two figures indicate that the substrate acts as a surfactant reservoir, and its dynamics are relatively unimportant.

For the specific parameters that have been used in Fig. 14b, increasing the value of $\beta_s$, (i.e. increasing the capacity of the substrate to adsorb surfactant) leads to stabilization of the flow. This behavior may be understood by considering that the surfactant that adsorbs at the substrate is subtracted from the total amount residing in the bulk and at the liquid-gas interface. We already know, however, that in the absence of adsorption at the substrate, the stability of our system depends non-monotonically on the total amount of surfactant (see Fig. 7 and the relevant discussion for the effect of $M_{tot}$). Since this total amount of surfactant varies with the adsorbability of the substrate, we deduce that different substrates may also affect the flow stability in a non-monotonic way.

This is confirmed in Fig. 14c, where we have plotted the critical $\chi$ as a function of the parameter $\beta_s$. For all values of $\xi_s$ (which expresses the relative solubility in the bulk *with respect to adsorption on the substrate*), the flow acquires maximum stability for intermediate values of $\beta_s$. For low values of $\beta_s$, critical $\chi$ tends to the limit of no adsorption at the substrate, whereas for high $\beta_s$ the capacity of the substrate to adsorb surfactant increases drastically and this leads to a decrease of $\chi_c$ as a large amount of surfactant is essentially removed from the system. It is noted in particular, that the decline of $\chi_c$ occurs at roughly constant $\beta_s$ ($\beta_s \approx 10^{-1}$), and is steeper the higher the value of $\xi_s$. These observations indicate that, when surfactants are to be used in order to stabilize the flow in various applications, it is also very important to pay special attention to the affinity of the selected surfactant with the substrate in hand.

*2.2.4.3.6 Effect of surfactant diffusivity*

Finally, Fig. 15 presents neutral curves for various values of the Schmidt number $Sc_a$ and $Sc_b$. It is evident that the effect of diffusion does not play any important role in the stability of the flow.

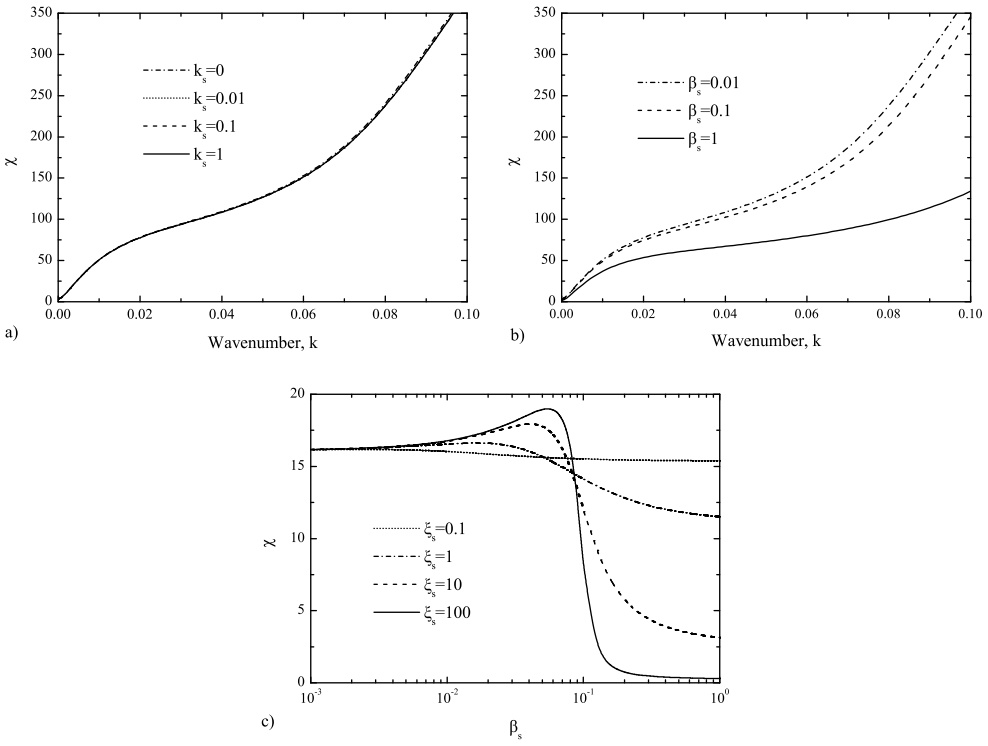


Figure 14: Effect of the adsorption of surfactant at the substrate. Neutral curves for $R_s = 1$ and various values of a) $k_s$ for $\beta_s = 0.01$, $R_s = 1$ and b) $\beta_s$ for $k_s = 0.1$, $R_s = 1$. c) Critical $\chi$ as a function of $\beta_s$ for various $\xi_s$ for $k_s = 0.1$. The rest of the parameters remain the same as in Fig. 4.

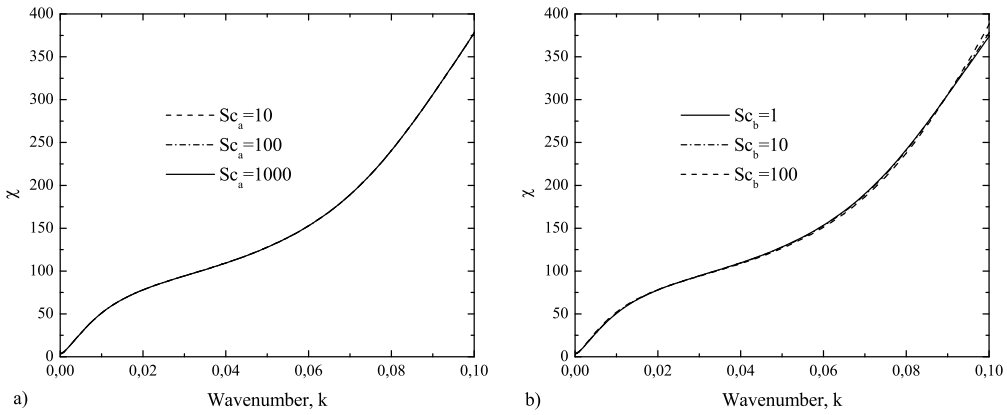


Figure 15: Neutral curves for different values of a) $Sc_a$ and b) $Sc_b$. The rest of the parameters remain the same as in Fig. 4

*2.2.4.4 Postulation of mechanisms and interpretation of experiments*

We conclude the above presentation of the effect of various system parameters with a discussion of possible mechanisms that operate in the case of soluble surfactants. Then, we attempt to interpret recent experimental observations that motivated this study, in the light of the present findings. With respect to potential mechanisms, we identify four key components: (i) *The effect of solubility in enhancing mass exchange between the interface and the bulk.* It appears that this mechanism determines the critical conditions that correspond to very long waves, and may lead to optimal behavior of moderately soluble surfactants. (ii) *The direct effect of disturbance wavenumber.* With increasing wavenumber, gradients in surface concentration of surfactant are expected to intensify, because variations take place on a shorter lengthscale. In addition to this, mass exchange -which mitigates gradients according to (i)- is weakened, because there is less time for the approach to equilibrium. (iii) *The effect of disturbance phase velocity.* We have observed that surfactant decreases drastically the phase velocity at high wavenumbers. Though we do not have a full understanding of the mechanism by which the flow stabilizes, we may plausibly assume that, as the wave moves downstream, it continuously sweeps surfactant by convection, thus inducing stabilizing surface tension gradients. This effect is expected to weaken by the decrease in phase velocity. The above components (ii) and (iii), that operate at high wavenumbers, have a competing effect, and their interplay could be responsible for the non-monotonic dependence of the critical conditions on wavenumber, which was observed at high amount/strength of surfactant (see

Fig. 9b and 10a). (iv) *The effect of phase shift between disturbances at the interface.* An understanding of the interaction between disturbances in height, velocity, surface concentration and shear stress would probably help unify the above components and delineate the complete stabilization mechanism. Work will be undertaken in this direction, following the approach of [8].

Returning to the experiments by [11] and [33], and in particular to the effect of soluble surfactant SDS, we note the following: Strong stabilization of liquid film flow was observed by the addition of small amounts of SDS, and the effect maximized at concentrations in the order of 10% of the critical micelle concentration, and then gradually receded. This behavior agrees qualitatively with the prediction for the critical conditions of a moderately soluble surfactant, as exhibited for example by Fig. 7a.

The dominant structures observed, even deep in the unstable regime, were sinusoidal travelling waves of small amplitude. Only at very high $Re$ in combination with very low-frequency inlet forcing, were non-sinusoidal structures observed, and these differed in shape from the solitary waves encountered in clean liquids. These observations are in accord with the predictions of the present study. In particular, it was shown that small amounts of soluble surfactant decrease drastically both the range and the growth rate of unstable wavenumbers (Figs. 9a,c). Smaller growth rate means that energy input from the mean flow to the unstable wavenumbers will be slower. This effect will further intensify, as the experimental inlet frequency remains constant while the cut-off frequency decreases. In addition, higher harmonics (which are sustained by energy input from the dominant mode through non-linear coupling, and which contribute to the shape of the final free-surface structures) have typical ampitudes of order inversly proportional to their damping rates. Thus, with the displacement of the entire dispersion curve to lower values, the magnitude of higher harmonics declines as well. The combination of all these effects, explains the experimentally observed persistence of nearly sinusoidal waves.

### 2.2.5 Conclusions

We investigated the linear stability of a film flowing down a solid substrate in the presence of a soluble surfactant. We used a detailed surfactant model, which considers monomers dissolved in the bulk and adsorbed with Langmuir kinetics at the gas/liquid and the solid/liquid interfaces. The Navier-Stokes equations for the liquid motion and the advection-diffusion equations for surfactant concentrations were linearized around the base flow, resulting in an Orr-Sommerfeld eigenvalue problem that was solved analytically in the limit of long-wave disturbances, and numerically for arbitrary wavelength using a finite element method.

The instability was shown to be a long-wave one, and the derived analytic solution for $k \to 0$ indicated that, among all the model parameters, critical conditions depend only on the solubility of the surfactant and on its interfacial concentration. An interesting finding was that, for a given total amount of surfactant, a moderately soluble one may produce stronger stabilization than the insoluble one. Optimum conditions were also found to vary with solubility,

the insoluble surfactant maximizing its performance at the tightest interfacial packing, whereas the soluble one at a fraction of it. These observations were explained by the competing effect of mass exchange between the interface and the bulk, which short-circuits surface tension gradients, and thus attenuates Marangoni stresses.

Disturbances of finite wavelength were considered next, and the additional lengthscale was observed to cause an escalation in complexity. Small amounts of soluble surfactant stabilize drastically the entire spectrum by shrinking the unstable range of wavenumbers, and by decreasing their growth rate and phase velocity. However, the effect maximizes at intermediate amounts and then drops again. For a fixed amount of surfactant, the role of solubility was shown to be highly non-trivial, and to depend strongly on the relative capacity of the interface and the bulk, $\beta_a$. Sorption kinetics at the gas-liquid interface was found to play a key role at finite wavelengths, with very slow kinetics leading to a virtually frozen interface and an insoluble-like behavior. Finally, it was shown that the adsorption capacity of the solid substrate may also have a significant effect.

In an attempt towards mechanistic understanding of the stabilization offered by a soluble surfactant, some factors contributing to the magnitude of interfacial gradients of surfactant concentration were proposed. These include mass exchange with the bulk, and wavelength and phase velocity of travelling disturbances. Finally, predictions by the present study appear to interpret convincingly some recent experimental observations on the effect of soluble surfactant SDS.

## 2.3 The role of surfactants on the mechanism of the long-wave instability in liquid film flows

### 2.3.1 Problem formulation and scaling

We study the dynamics of liquid films flowing along an infinite planar wall, inclined at an angle $\alpha$ with the horizontal plane (see Fig. 16). The film is laden with a soluble, non-volatile surfactant which may adsorb at the liquid-air interface altering surface tension, or it can exist in the bulk in the form of monomers. The fluid is Newtonian with constant density $\rho$ and kinematic viscosity $\nu$, and with surface tension, $\sigma$, which depends on the interfacial concentration of surfactant, $\Gamma$, through a constitutive equation $\sigma = \sigma(\Gamma)$. For the present purposes of a linear analysis, we do not have to consider a specific constitutive law for surface tension. We define, however, the surface elasticity $E(\Gamma)$

$$E(\Gamma) = -\frac{d\sigma}{d\,(ln\,\Gamma)}. \tag{93}$$

which contains the dependence of surface tension on interfacial surfactant concentration; a specific expression for $E(\Gamma)$ can be derived once the constitutive equation is specified.

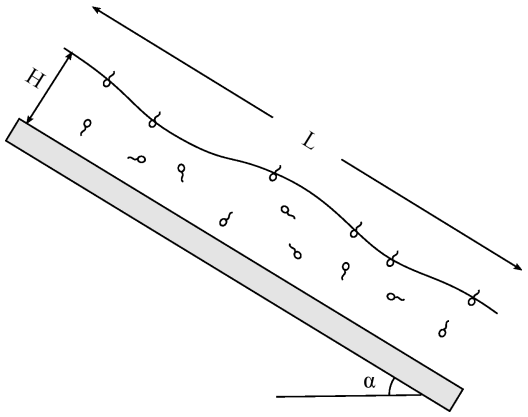


Figure 16: Schematic of a falling film in the presence of soluble surfactants.

In order to model two-dimensional dynamics, we use a Cartesian coordinate system $(x, z)$, with $x$ pointing in the streamwise and $z$ in the cross-stream direction. The velocity and pressure fields are respectively $\mathbf{u} = (u, w)$ and $p$. The liquid-air interface is located at $z = h(x, t)$ and the liquid-solid interface at $z = 0$. The flow is governed by the continuity and momentum conservation equations, subject to the zero-velocity boundary condition at the solid wall and the kinematic and dynamic boundary conditions at the free surface. The latter includes both a normal contribution due to surface tension and a tangential one due to the variation of surface tension along the free surface.

To account for the presence of soluble surfactants, we utilize a simplified version of the kinetic model of [35] and [36, 37]. Surfactant partitioning between the bulk concentration, $c$, and the interfacial one, $\Gamma$, is described by a Langmuir model, with $\Gamma_\infty$ the interfacial concentration at maximum packing and $k_1$, $k_2$ the constants of the first-order adsorption and desorption kinetics. Mass conservation of adsorbed and dissolved surfactant is modelled by two advection-diffusion equations, one for the interface and one for the bulk. The net flux of monomer between interface and bulk is given by the kinetic model, and appears as a term in the equation of the interface and as a boundary condition in the equation of the bulk. The above physical model is the same as in [42], where we refer the reader for a more detailed description.

The governing equations and boundary conditions are made dimensionless, using the following scaling:

$$\begin{gathered}(\tilde{x}, \tilde{z}) = (x, z)/H,\ \tilde{h} = h/H,\ \tilde{t} = tU/H,\ \tilde{\mathbf{u}} = \mathbf{u}/U, \\ p = p_{air} + \rho g H \sin\alpha\, \tilde{p},\ (\tilde{\Gamma}, \tilde{c}) = (\Gamma, Hc)/\Gamma_\infty, \\ \tilde{J}_{ba} = J_{ba}\frac{H}{U\Gamma_\infty},\ \tilde{\sigma} = \frac{\sigma}{\sigma_c}, \tilde{M_{tot}} = \frac{M_{tot}}{L\Gamma_\infty}\end{gathered} \tag{94}$$

$J_{ba}$ denotes the net flux of surfactant at the interface and $M_{tot}$ is the total amount of surfactant that is present in our system. As a characteristic length

we use the height of the Nusselt flat film, $H = (3\nu Q/(g\sin\alpha))^{1/3}$, where $Q$ denotes the imposed flow rate. The velocities are scaled with the corresponding interfacial velocity, $U = gH^2\sin\alpha/(2\nu)$, and $\sigma_c = \sigma(\Gamma = 0)$ is the surface tension of the clean liquid. Tildes denote dimensionless variables and are henceforth suppressed.

Introducing the above scaling, the continuity and momentum conservation equations become,

$$u_x + w_z = 0. \tag{95}$$

$$Re(u_t + uu_x + wu_z) + 2p_x - u_{xx} - u_{zz} - 2 = 0, \tag{96}$$

$$Re(w_t + uw_x + ww_z) + 2p_z - w_{xx} - w_{zz} + 2\cot\alpha = 0, \tag{97}$$

where $Re = \frac{gH^3\sin\alpha}{2\nu^2}$ is the Reynolds number. Unless stated otherwise, the subscripts denote partial differentiation with respect to $x$, $z$ and time $t$.

The components of the dynamic boundary condition tangential and normal to the free surface are respectively

$$-4u_xh_x + (u_z + w_x)(1 - h_x^2) = 2We\ \sigma_x\sqrt{1 + h_x^2}, \tag{98}$$

$$p + \frac{u_x(1 - h_x^2) + (u_z + w_x)h_x}{1 + h_x^2} = -We\ \sigma\frac{h_{xx}}{(1 + h_x^2)^{3/2}}, \tag{99}$$

where $We = \frac{\sigma_c}{\rho g H^2\sin\alpha}$ is the Weber number. In addition, we impose at the liquid-solid interface ($z = 0$), the usual no-slip, no-penetration conditions, $u = w = 0$, and along the moving interface ($z = h(x,t)$) the kinematic boundary condition $h_t + uh_x = w$.

The dimensionless form of surfactant conservation in the bulk becomes

$$c_t + uc_x + wc_z = Pe_b^{-1}(c_{xx} + c_{zz}), \tag{100}$$

where $Pe_b = Re\frac{\nu}{D_b}$ is the Peclet number in the bulk, with $D_b$ the surfactant diffusivity in the bulk. The above equation is subject to the following boundary conditions, along the interface ($z = h(x,t)$)

$$\frac{h_xc_x - c_z}{Pe_b\sqrt{1 + h_x^2}} = J_{ba}, \tag{101}$$

and along the wall($z = 0$)

$$c_z = 0. \tag{102}$$

Surfactant conservation at the interface is modelled by the following advection-diffusion equation

$$\Gamma_t + u\Gamma_x + \Gamma\nabla_s\cdot\mathbf{u} = \frac{\nabla_s^2\Gamma}{Pe_a} + J_{ba}, \tag{103}$$

where $Pe_a = Re\frac{\nu}{D_a}$ is the interfacial Peclet number, with $D_a$ the surfactant diffusivity at the interface, and $\nabla_s$ is the surface gradient, defined as $\nabla_s = (I - \mathbf{nn}^T)\cdot\nabla$. It is noted that the derivation of Eq. (103) involves some subtle points related to the movement of the interface and the definition of the time

derivative [43]. Another version of this equation has been repeatedly quoted incorrectly in the literature but as was shown by [43] Eq. (103) is actually more appropriate.

Finally, the dimensionless expression for the net adsorption flux in Eqs. (101) and (103) is

$$J_{ba} = k_a \left[\xi_a c|_{z=h} \left(1 - \Gamma\right) - \Gamma\right]. \tag{104}$$

where $k_a = \frac{k_2 H}{U}$ and $\xi_a = \frac{k_1}{k_2 H}$. The physical significance of these parameters is as follows: Term $k_a$ is the ratio of the time-scale of convection to the time-scale of desorption. For example, $k_a << 1$ means that the backward reaction is slow compared to convection, and thus a temporary decrease of the bulk concentration near the interface will not lead to significant desorption. Term $\xi_a$ is the ratio of the kinetic constants of the forward and backward reaction for the interface-bulk interaction, and thus provides a direct measure of surfactant solubility in the bulk [41]. More specifically, $\xi_a << 1$ signifies a highly soluble and $\xi_a >> 1$ a sparingly soluble surfactant.

### 2.3.2 Linearization and normal mode analysis

The above set of governing equations and boundary conditions has a trivial solution corresponding to a flat film with uniform surfactant concentration. In the case of a clean fluid, this is also known as the Nusselt flat film solution and its dimensionless form is shown below

$$\bar{h} = 1,\ \bar{u} = 2z - z^2,\ \bar{w} = 0,\ \bar{p} = (1 - z)\cot\alpha, \tag{105}$$

where an overbar denotes the base state. In order for the above solution to remain valid when a soluble surfactant is present, the concentrations should be uniform and at equilibrium. Imposing these conditions leads to,

$$\bar{c} = \frac{\bar{\Gamma}}{\xi_a \left(1 - \bar{\Gamma}\right)}, \tag{106}$$

and given that the total mass of the surfactant, $M_{tot}$, is conserved and evaluated by the following expression

$$\bar{c} + \bar{\Gamma} = M_{tot}, \tag{107}$$

it is possible to derive an analytical expression for $\bar{c}$ and $\bar{\Gamma}$ as function of the parameters $M_{tot}$ and $\xi_a$ [42].

We perform a linear stability analysis by perturbing the flow around the above flat film solution. To this end we write all variables as the sum of the base state and a small perturbation

$$\phi = \bar{\phi} + \phi', \tag{108}$$

and linearize the system assuming $\phi' << \bar{\phi}$. We also apply the relevant boundary conditions around the mean elevation of the interface, $z = 1$, by expanding the variables in Taylor series as follows

$$\phi|_{z=h} = \bar{\phi}|_{z=h} + \phi'|_{z=h} = \left(\bar{\phi}|_{z=1} + h' \frac{\partial \bar{\phi}}{\partial z}|_{z=1}\right) + \phi'|_{z=1} + O(h'^2). \tag{109}$$

The set of linearized equations and boundary conditions is analysed by considering the normal modes:

$$\begin{pmatrix} h'(x,t) \\ u'(x,z,t) \\ w'(x,z,t) \\ p'(x,z,t) \\ c'(x,z,t) \\ \Gamma'(x,t) \\ J'_{ba}(x,t) \end{pmatrix} = \begin{pmatrix} \hat{h} \\ \hat{u}(z) \\ \hat{w}(z) \\ \hat{p}(z) \\ \hat{c}(z) \\ \hat{\Gamma} \\ \hat{J}_{ba} \end{pmatrix} exp[ik(x - Ct)], \tag{110}$$

where $k = 2\pi H/\lambda$ is the dimensionless wavenumber of the disturbance with wavelength $\lambda$, and $C$ is the complex eigenvalue, $C = C_r + iC_i$, with $C_r$ the dimensionless phase velocity scaled with the Nusselt film surface velocity $U$ and $kC_i$ the growth rate. The final system of normal-mode disturbance equations is

$$Re[ik(\bar{u} - C)\hat{u} + \bar{u}_z\hat{w}] + 2ik\hat{p} + k^2\hat{u} - \hat{u}_{zz} = 0, \tag{111}$$

$$ikRe(\bar{u} - C)\hat{w} + 2\hat{p}_z + k^2\hat{w} - \hat{w}_{zz} = 0, \tag{112}$$

$$ik\hat{u} + \hat{w}_z = 0, \tag{113}$$

$$Pe_b ik(\bar{u} - C)\hat{c} + k^2\hat{c} - \hat{c}_{zz} = 0, \tag{114}$$

and the following boundary conditions are applied along the mean interfacial elevation ($z = 1$)

$$\hat{u}_z(1) + ik\hat{w}(1) + \bar{u}_{zz}(1)\hat{h} + 2ikWe\,\frac{\bar{E}}{\bar{\Gamma}}\hat{\Gamma} = 0, \tag{115}$$

$$\hat{p}(1) - \hat{h}\cot\alpha + ik\hat{u}(1) - k^2We\,\bar{\sigma}\hat{h} = 0, \tag{116}$$

$$ik[\bar{u}(1) - C]\hat{h} - \hat{w}(1) = 0, \tag{117}$$

$$(\bar{u}(1) - C)ik\hat{\Gamma} + \bar{\Gamma}ik\hat{u}(1) + \frac{k^2\hat{\Gamma}}{Pe_a} - \hat{J}_{ba} = 0, \tag{118}$$

$$\hat{J}_{ba} = \frac{-\hat{c}_z(1)}{Pe_b} = k_a\left[\xi_a\left[(1 - \bar{\Gamma})\hat{c}(1) - \bar{c}\hat{\Gamma}\right] - \hat{\Gamma}\right], \tag{119}$$

and along the wall ($z = 0$)

$$\hat{u}(0) = \hat{w}(0) = 0, \tag{120}$$

$$\hat{c}_z(0) = 0. \tag{121}$$

In the above $\bar{\sigma}$ denotes the surface tension that corresponds to the base state surface concentration $\bar{\Gamma}$ and

$$\bar{E} = -\bar{\Gamma}\left(\frac{d\bar{\sigma}}{d\bar{\Gamma}}\right)_{\bar{\Gamma}}. \tag{122}$$

### 2.3.3 Long-wave expansion

*2.3.3.1 Initiating mechanism*

The physical system considered has been shown [42] to be susceptible to a long-wave instability. The mechanism for this instability can be identified in the ordered problems that arise from a regular expansion of the normal-mode amplitudes in the limit $k \to 0$. More specifically, we posit

$$\hat{u} = u_0 + ku_1 + k^2 u_2 + O(k^3), \tag{123}$$

$$\hat{w} = kw_1 + k^2 w_2 + O(k^3), \tag{124}$$

$$\hat{p} = p_0 + kp_1 + k^2 p_2 + O(k^3), \tag{125}$$

$$C = C_0 + kC_1 + k^2 C_2 + O(k^3), \tag{126}$$

$$\hat{c} = c_0 + kc_1 + k^2 c_2 + O(k^3), \tag{127}$$

$$\hat{\Gamma} = \Gamma_0 + k\Gamma_1 + k^2 \Gamma_2 + O(k^3), \tag{128}$$

$$\hat{J}_{ba} = J_{ba,0} + kJ_{ba,1} + k^2 J_{ba,2} + O(k^3), \tag{129}$$

$$\hat{h} = h_0 + kh_1 + k^2 h_2 + O(k^3), \tag{130}$$

We are interested in the 'interfacial mode' that is triggered by a deflection of the free surface, and which is known to be the unstable one [29, 32]; the aforementioned papers have shown for an insoluble surfactant that a 'concentration mode' also exists, which is stable and actually not related to the surfactant property (see Appendix). Thus, we normalize the system of equations by assuming that $h_0 = 1$ and $h_1 = h_2 = 0$, implying that all perturbation amplitudes to be subsequently calculated are proportional to the amplitude, $h_0$, of the free surface deformation. The lack of an $O(k^0)$ term in the expansion of $\hat{w}$ in the long-wave limit is a direct consequence of continuity, Eq. (113).

At order $O(k^0)$, we combine the normal mode momentum equations, the force balance at the interface and the wall boundary condition,

$$u_{0zz} = 0\,,\ u_0(0) = 0\,,\ u_{0z}(1) = -\bar{u}_{zz}(1) = 2\,,\ p_{0z} = 0\,,\ p_0(1) = \cot\alpha, \tag{131}$$

and obtain the well-known leading order perturbation to the base flow,

$$u_0(z) = 2z\,,\ p_0(z) = \cot\alpha. \tag{132}$$

As explained by [7] and [8], when the interface deforms, a nonzero shear stress, $\bar{u}_{zz}(1)h'$, results from the base flow because of the local curvature of its velocity profile at the interface. Therefore, a perturbation shear stress develops that exactly cancels the above, and this drives the longitudinal flow perturbation $u_0(z)$.

In order to solve for the concentrations, we combine at order $O(k^0)$ mass conservation in the bulk and at the interface, and no-penetration at the wall, and obtain

$$c_{0zz} = 0\,,\; c_{0z}(0) = 0\,,\; \frac{c_{0z}(1)}{Pe_b} = -J_{ba,0}. \tag{133}$$

Therefore,

$$c_0(z) = \frac{\Gamma_0}{\xi_a(1-\bar{\Gamma})^2} = \text{constant}. \tag{134}$$

Eqs. (133) and (134) state that, at zero order, convection is negligible and the interface is in equilibrium with the bulk. This is reasonable, given that in the limit $k \to 0$ variations along the wavelength become very slow, and the resistance to mass transfer in the cross-stream direction diminishes.

It is also notable that the concentrations are not fully determined at order $O(k^0)$. This happens because the initial deformation of the interface does not trigger by itself any change in the concentration of surfactant (the dilation of the interface is second-order in the deformation amplitude, i.e. linearly negligible). As will be shown next, it is actually the leading order flow perturbation, $u_0(1)$, that disturbs the interfacial concentration, and this occurs through a convective contribution that appears at order $O(k^1)$.

Next, we consider the normal mode, mass conservation equations at order $O(k^1)$ and obtain,

$$Pe_b\, i(\bar{u} - C_0)c_0 = c_{1zz}\,,\; c_{1z}(0) = 0\,,\; \frac{c_{1z}(1)}{Pe_b} = -J_{ba,1}, \tag{135}$$

and

$$(\bar{u}(1) - C_0)i\Gamma_0 + i\bar{\Gamma}u_0(1) = -\frac{c_{1z}(1)}{Pe_b}. \tag{136}$$

The leading order wave velocity, $C_0$, is derived from the kinematic boundary condition, Eq. (117),

$$i(\bar{u}(1) - C_0) = w_1(1) \;\Rightarrow\; C_0 = \bar{u}(1) + iw_1(1). \tag{137}$$

From continuity, Eq. (113), we obtain

$$w_{1z} + iu_0 = 0 \;\Rightarrow\; w_1(z) = -iz^2, \tag{138}$$

and therefore we deduce that

$$C_0 = 2. \tag{139}$$

Integrating Eq. (135), we obtain the $O(k^1)$ amplitude of the bulk concentration perturbation

$$c_1(z) = i\,c_0\left[Pe_b\left(\frac{3}{4} - z^2 + \frac{z^3}{3} - \frac{z^4}{12}\right) + \frac{4}{3(1-\bar{\Gamma})k_a\xi_a} - i\,\frac{\Gamma_1}{\Gamma_0}\right]. \tag{140}$$

Eq. (136) may now be solved, using (134), (139) and (140), to obtain the zero-order perturbation in the interfacial concentration of surfactant,

$$\Gamma_0 = 2\bar{\Gamma}\left(\frac{3\xi_a(1-\bar{\Gamma})^2}{3\xi_a(1-\bar{\Gamma})^2+4}\right), \tag{141}$$

and, through Eq. (134), also the zero-order perturbation to the bulk concentration.

Analysis of Eq. (136) provides an understanding of the initiating mechanism of concentration perturbation. We focus first on the two terms on the lhs, which balance exactly in the case of an insoluble surfactant. The second term represents convective transport of the mean interfacial concentration because of the variation along the wave of the leading order flow perturbation, $u_0(1)$. This term disrupts the uniform interfacial concentration; more specifically, it produces a flux that is maximum at the back node and minimum at the front node ("back" and "front" are in reference to the crest of surface displacement), and as a result, it moves surfactant away from the trough and towards the crest. Thus, a perturbation $\Gamma_0$ with maximum at the crest and minimum at the trough arises, whose convective transport by the mean flow is expressed by the first term on the lhs of Eq. (136). The perturbation in $\Gamma$ is such that the two convective fluxes, combined with mass exchange with the bulk (the rhs term), balance. We should note at this point that in the case of insoluble surfactants, the concentration was shown by [31] to be in-phase with the surface displacement and we see that, at leading order, this is true for soluble surfactants as well.

Equivalently, we may consider a reference frame that renders the wave stationary, and in this case the interfacial velocity is given by

$$u|_{z=h} - C_0 = [\bar{u}(1) - C_0] + u'(1), \tag{142}$$

and since $u'(1) = \hat{u}(1)h' = u_0(1)h' + O(k^2)$ and $u_0(1) = 2$ we obtain

$$u|_{z=h} - C_0 = -1 + 2h' + O(k^2). \tag{143}$$

Therefore, the interfacial streamwise velocity has a magnitude which is maximum at the trough and minimum at the crest of the interfacial displacement (see Fig. 17). Given that the system is at steady state in this reference frame (and thus the flux of surfactant is the same at every streamwise location), we conclude that the interfacial concentration varies inversely to the interfacial velocity, i.e. it is maximum at the crest and minimum at the trough.

It is noted that the three fluxes in Eq. (136) have the same phase, which lags $90^o$ behind the displacement (as it will be shown below, $c_1(z)$ is pure imaginary). Therefore, the perturbation in surfactant concentration is at leading order in-phase with the interface displacement, a result that is directly evident from Eq. (141); as will be shown later, the phases start to deviate at order $O(k^1)$. Eq. (141), also indicates that the leading order effect of surfactant solubility is to decrease the magnitude of concentration perturbation at the interface (it is recalled that $\xi_a >> 1$ corresponds to a sparingly soluble, and $\xi_a << 1$ to a highly soluble surfactant).

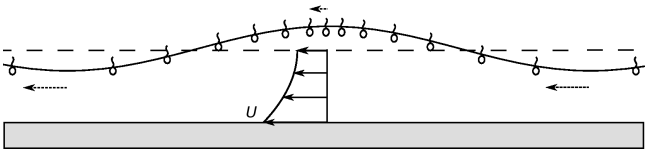


Figure 17: A disturbance to the free surface. The dotted arrows depict the direction and magnitude of the interfacial velocity at various positions, assuming a moving frame of reference that renders the wave stationary. The long-dash line is the undisturbed free surface position and the line arrows depict the mean velocity profile in this reference frame.

The effect of surfactant solubility becomes more evident by evaluating directly the rate of mass transfer between the bulk and the interface, i.e. the rhs of Eq. (136). Using Eq. (140), we obtain

$$J_{ba,1} = -\frac{c_{1z}(1)}{Pe_b} = \frac{i\,8\bar{\Gamma}}{3\xi_a(1-\bar{\Gamma})^2+4} \tag{144}$$

We observe that the transfer rate of surfactant is $90^o$ out of phase with the displacement (see Fig. 18), i.e. at the front node (with respect to the crest) transfer of surfactant is from the interface towards the bulk, and at the back node it is from the bulk towards the interface. This is precisely the opposite effect from the convective transport by the leading order flow perturbation, as described above. Thus, exchange with the bulk opposes transport by the flow perturbation, and therefore diminishes the perturbation in interfacial concentration of surfactant. In the limit of a highly soluble surfactant ($\xi_a \to 0$) $J_{ba,1} = i\,2\bar{\Gamma}$ and $\Gamma_0 = 0$, i.e. the two fluxes become exactly equal and opposite, and as a result interfacial gradients (and Marangoni stresses) disappear altogether.

*2.3.3.2 Effect of surfactant on the growth mechanism*

We proceed to calculate the $O(k^1)$ longitudinal velocity perturbation, $u_1(z)$, which is evaluated from the x-momentum Eq. (111)

$$u_{1zz} = 2ip_0 + Re[i(\bar{u}-C_0)u_0 + \bar{u}_z w_1]\,, \tag{145}$$

subject to the boundary conditions of zero velocity at the wall, $u_1(0) = 0$, and tangential force balance at the interface,

$$u_{1z}(1) = -2i\frac{We\,\bar{E}}{\bar{\Gamma}}\Gamma_0. \tag{146}$$

Eqs. (145) and (146) contain the essence of the growth mechanism. Following [8], we recall that Eq. (145) represents a balance between viscous stress gradient, $u_{1zz}$, and the pressure and inertial stresses that contribute to the flow

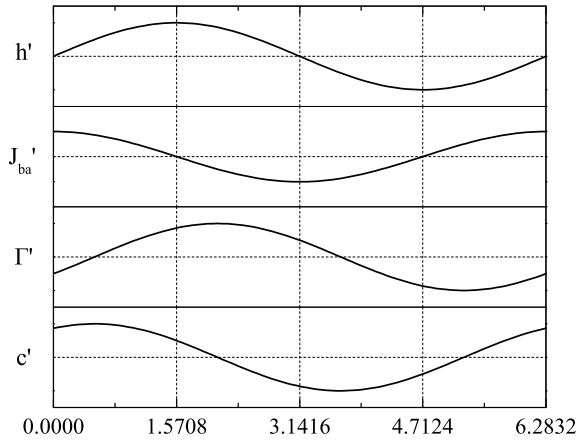


Figure 18: Spatial wave forms of the film height, $h'$, interfacial flux, $J'_{ba}$, interfacial concentration, $\Gamma'$, and concentration in the bulk, $c'$.

$u_1$. Term $p_0 = \cot\alpha$ is positive, thus pressure is in-phase with interface deformation i.e. maximum below the crest and minimum below the trough. This distribution is stabilizing, draining liquid away from the crests and towards the troughs. On the contrary, the two inertial stresses, representing advection of flow perturbations by the base state velocity relative to the moving disturbance, are negative and therefore destabilizing. In particular, the dominant negative contribution, $-Re\,C_0 u_0$, corresponds to temporal acceleration by the wave motion, whereas the remaining terms represent convective acceleration and sum up to a slightly stabilizing contribution. Thus, the unsteadiness associated with the moving disturbance is the cause of the instability.

The role of surfactant is given by the boundary condition (146), which represents the contribution to the flow $u_1$ due to Marangoni stresses. More specifically, integration of (145) subject to (146) gives

$$u_1(z) = i\left[Re\left(\frac{z^4}{6} - \frac{2z^3}{3} + \frac{4z}{3}\right) - \cot\alpha\left(2z - z^2\right) - 4\,We\,\bar{E}\left(\frac{3\xi_a(1-\bar{\Gamma})^2}{3\xi_a(1-\bar{\Gamma})^2 + 4}\right) z\right], \tag{147}$$

which indicates that the $O(k^1)$ longitudinal velocity perturbation is $90^o$ out of phase with the displacement, attaining extrema at the nodes of the travelling wave. The last term on the rhs of Eq. (147) represents the additional flow perturbation caused by the Marangoni stresses at the interface. Its coefficient is negative, and thus it is maximum at the front node and minimum at the back node with respect to the crest, i.e. it drives liquid away from the crest This is the expected effect of the Marangoni stresses that are induced by the

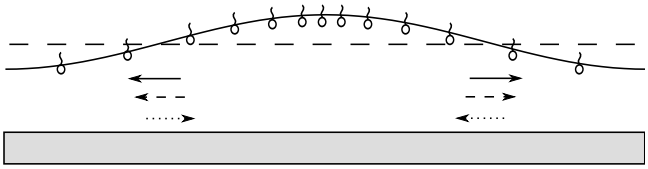

Figure 19: A disturbance to the free surface. The line-arrow depicts the action of Marangoni stresses (stabilizing), the dash-arrow depicts the action of pressure (stabilizing) and the dot-arrow depicts the action of inertia terms (destabilizing) in Eq. (147). The long-dash line is the undisturbed free surface position.

leading order perturbation in $\Gamma$, Eq. (141), given that $\Gamma_0$ is in-phase with surface displacement, i.e. maximum at the crests and minimum at the troughs. The action of each of the terms of Eq. (147) is depicted schematically in Fig. 19.

The contribution to the complex eigenvalue at order $O(k^1)$ is determined from the kinematic boundary condition (117) at order $O(k^2)$

$$C_1 = i w_2(1). \tag{148}$$

The cross-stream velocity $w_2$ is calculated by integration of the continuity equation, $w_{2z} + i u_1 = 0$, subject to $w_2(0) = 0$. Substituting $u_1$ from Eq. (147), we obtain,

$$w_2(z) = \cot\alpha \left(\frac{z^3}{3} - z^2\right) + Re \left(\frac{2z^2}{3} - \frac{z^4}{6} + \frac{z^5}{30}\right) - 2\,We\,\bar{E} \left(\frac{3\xi_a(1-\bar{\Gamma})^2}{3\xi_a(1-\bar{\Gamma})^2 + 4}\right) z^2. \tag{149}$$

Combining Eqs. (148) and (149), we obtain

$$C_1 = i \left[-\frac{2}{3}\cot\alpha + \frac{8}{15} Re - 2\,We\,\bar{E} \left(\frac{3\xi_a(1-\bar{\Gamma})^2}{3\xi_a(1-\bar{\Gamma})^2 + 4}\right)\right]. \tag{150}$$

Therefore, the growth rate of the disturbance is -to this order- equal to

$$kC_i = \frac{8}{15} k^2 \left[Re - \frac{5}{4}\cot\alpha - \frac{15}{4}\,We\,\bar{E} \left(\frac{3\xi_a(1-\bar{\Gamma})^2}{3\xi_a(1-\bar{\Gamma})^2 + 4}\right)\right], \tag{151}$$

and the critical condition for instability, determined by setting $C_i = 0$, is found to be

$$Re_{c,0} = \frac{5}{4}\cot\alpha + \frac{15}{4}\,We\,\bar{E} \left(\frac{3\xi_a(1-\bar{\Gamma})^2}{3\xi_a(1-\bar{\Gamma})^2 + 4}\right), \tag{152}$$

a result originally derived by [42]. In the limit of an insoluble surfactant ($\xi_a >> 1$) Eq. (152) is in agreement with the expression given by [30, 32].

It is interesting to note that, for typical constitutive models $\sigma = \sigma(\Gamma)$, the last term on the rhs of Eq. (152) is in general a non-monotonic function of $\bar{\Gamma}$. Thus, moderately soluble surfactants exhibit maximum stabilization at intermediate concentrations. Using as an indicative example the Sheludko model

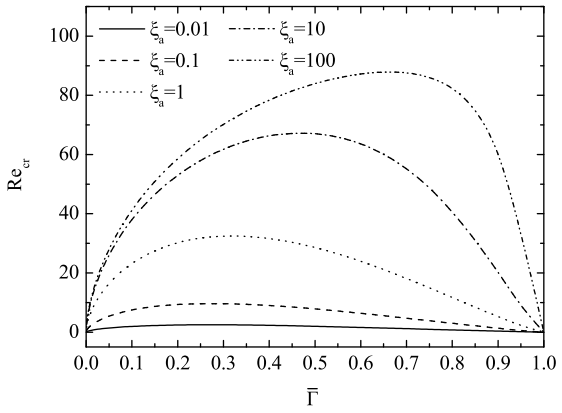


Figure 20: Dependence of the critical Reynolds number on the interfacial concentration, $\bar{\Gamma}$ for different values of $\xi_a$. The dependence of surface tension on the interfacial concentration was modelled using the equation of state suggested by [39]; $\bar{\sigma} = \left[1 + \bar{\Gamma}\left(\Sigma^{1/3} - 1\right)\right]^{-3}$; in this case $\bar{E}$ is given by $\bar{E} = 3\bar{\Gamma}\left(\Sigma^{1/3} - 1\right)\left[1 + \bar{\Gamma}\left(\Sigma^{1/3} - 1\right)\right]^{-4}$. The rest of the parameters are: $\alpha = 90^o$, $Ka = 3000$, $\Sigma = 2$; $\Sigma = \sigma_c/\sigma_m$, where $\sigma_c$ and $\sigma_m$ denote the surface tensions of a surfactant-free fluid and that of maximal surfactant concentration, respectively.

[39] and a vertical wall ($\cot\alpha = 0$), we find that the dependence of critical $Re$ on surface concentration of surfactant varies parametrically with surfactant solubility as shown in Fig. 20. At small values of $\xi_a$, the maximum in $Re_{cr}$ occurs around $\bar{\Gamma} \approx 0.27$, whereas with increasing $\xi_a$ (decreasing solubility), the maximum gradually drifts towards $\bar{\Gamma} = 1$.

*2.3.3.3 Higher-order terms*

*2.3.3.3.1 Interfacial concentration for non-zero wavenumbers*

The above procedure may be continued to higher orders, at the expense of rapidly increasing algebraic complexity. For example, integrating the $O(k^2)$ terms of (114) and combining with the boundary conditions (118) at order $O(k^2)$ and (119) at order $O(k^1)$, we obtain the first order amplitude of the interfacial concentration, $\Gamma_1$

$$\Gamma_1 = -i\frac{\Gamma_0^2}{\bar{\Gamma}}\left[\frac{8}{9k_a\xi_a^2(1-\bar{\Gamma})^3} + \frac{1}{(1-\bar{\Gamma})^2\xi_a}\left(\frac{1}{2Pe_b} + \frac{37}{105}Pe_b\right) + \frac{1}{2Pe_a} - \left(\frac{1}{90(1-\bar{\Gamma})^2\xi_a} - \frac{7}{120}\right)Re + \frac{\bar{E}We}{3(1-\bar{\Gamma})^2\xi_a + 4} - \frac{\cot\alpha}{12}\right] = -i\frac{\Gamma_0^2}{\bar{\Gamma}}f(\kappa,\mu), \tag{153}$$

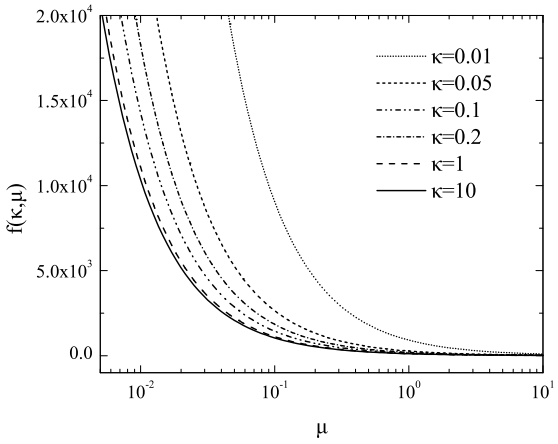


Figure 21: Dependence of the function $f(\kappa, \mu)$ on the value of $\mu$ for various values of $\kappa$. Typical values have been used for the rest of the dimensionless parameters: $Re = 100$, $We = 100$, $Pe_b = 100$, $Pe_a = 1000$, $\bar{E} = 0.3$, $\alpha = 90^o$

where the terms in the squared brackets have been grouped in the function $f(\kappa, \mu)$, with $\kappa = 3k_a\xi_a(1-\bar{\Gamma})$ and $\mu = 3\xi_a(1-\bar{\Gamma})^2$. The parametric variation of the function $f(\kappa, \mu)$ is presented in Fig. 21 for typical values of the dimensionless parameters and for the case of a vertical wall. Eq. (153) indicates that the effect of adsorption modelling at order $O(k^1)$ and beyond is conveniently described by the parameters $\kappa$ and $\mu$, which are related respectively to the speed of adsorption kinetics and to the solubility of the surfactant. (In particular, we recall from Eq. (104) that $k_a\xi_a = k_1/U$, therefore, $k_a\xi_a >> 1$ means that the interface is always at equilibrium with the bulk, and $k_a\xi_a << 1$ means that the exchange between interface and bulk is negligible, i.e. the interfacial concentration is "frozen"). With appropriate selection of the ranges of these parameters, one may examine various particular cases. For example, for an insoluble surfactant ($\kappa \sim O(1)$, $\mu >> O(1)$), we obtain the expression,

$$\Gamma_1 = -i\bar{\Gamma}\left(\frac{7}{30}Re + \frac{2}{Pe_a} - \frac{1}{3}\cot\alpha\right) \tag{154}$$

We note from Eqs. (153) and (154) that $\Gamma_1$ is purely imaginary, and - according to Eq. (140)- so is $c_1(z)$ and in particular $c_1(1)$. Thus, the phases of the adsorbed and free concentrations at the interface, start at order $O(k^1)$ to deviate from the phase of the interface deformation. More specifically, the phases of the interfacial and bulk concentration, up to this order, are given by

the expressions:

$$\tan\phi_\Gamma = \frac{\mathrm{Im}[\hat{\Gamma}]}{\mathrm{Re}[\hat{\Gamma}]} = \frac{-ik\Gamma_1}{\Gamma_0} + O(k^2), \tag{155}$$

$$\tan\phi_c = \frac{\mathrm{Im}[\hat{c}]}{\mathrm{Re}[\hat{c}]} = \frac{-ikc_1(1)}{c_0} + O(k^2). \tag{156}$$

The direction in which the maximum in $\Gamma'$ moves depends on the sign of $\Gamma_1$. For an insoluble surfactant, Eq. (154) shows that $\Gamma_1$ is negative for all cases of practical interest, therefore the maximum moves ahead of the deformation crest. The same holds also for the general result, Eq. (153), which also contains negative terms. Indeed, the parametric variation of $f(\kappa,\mu)$ depicted in Fig. 21 shows that for all values of $\kappa$, $f(\kappa,\mu) > 0$ and the maximum in surface concentration precedes the deformation crest.

Using Eq. (140), we can readily show that the phase of the concentration in the bulk is related to that of the interfacial concentration by

$$\tan\phi_c = \tan\phi_\Gamma + \frac{4k}{3(1-\bar{\Gamma})k_a\xi_a} + O(k^2) = \tan\phi_\Gamma + \frac{4k}{\kappa} + O(k^2). \tag{157}$$

Therefore, $c$ is in-phase with $\Gamma$ when the adsorption kinetics are fast enough ($\kappa >> 1$), but lags behind it for moderate and slow kinetics. An example of the latter case is provided by the time traces of deformation, flux and concentrations depicted in Fig. 18.

*2.3.3.3.2 Wave velocity and growth rate for non-zero wavenumbers*

Next, we calculate an improved prediction for the phase velocity, $C_r$, valid up to order $O(k^2)$. By using the kinematic boundary condition, Eq. (117), at order $O(k^2)$, we obtain an expression for $C_2$, which is real and thus contributes only to $C_r$. The final result is

$$C_r = 2 - k^2\left[2 + \frac{32}{63}Re\left(Re - \frac{5}{4}\cot\alpha\right) + We\bar{E}\frac{\Gamma_0}{\bar{\Gamma}}\left(\frac{\Gamma_0}{\bar{\Gamma}}f(\kappa,\mu) - \frac{19}{20}Re\right)\right] + O(k^4) \tag{158}$$

In the limit of a clean liquid ($\bar{E} = 0$), Eq. (158) agrees with the result by [44]. In the limiting case of an insoluble surfactant, Eq. (158) may be further simplified, and after some algebra we obtain,

$$C_r = 2 - k^2\left[2 + \frac{32}{63}Re\left(Re - \frac{5}{4}\cot\alpha - \frac{15}{4}We\bar{E}\right) + We\bar{E}\left(\frac{5}{21}Re + \frac{2}{Pe_a} - \frac{\cot\alpha}{3}\right)\right] \tag{159}$$

It is concluded from Eq. (159) that for vertical films disturbances of finite wavelength travel slower than the long-wave ones. In particular, it is noted that, from the two terms in parentheses inside the brackets, the first one contains $Re - Re_{c,0}$ and is thus positive beyond the primary threshold, and for $\alpha = 90^o$ the second contains only two positive terms ($5Re/21$ and $2/Pe_a$).

We follow a similar procedure at order $O(k^3)$ and evaluate $C_3$, which is purely imaginary and contributes only to the growth rate. Since the growth rate to this order is given by $kC_i \approx C_1 k^2 + C_3 k^4$, we determine the critical condition for instability for non-zero wavenumbers ($k \neq 0$) by setting $C_i = 0$. As the resulting expression is implicit in $Re$, we derive an analytic solution by positing the expansion

$$Re_c = Re_{c,0} + k^2\, Re_{c,2}. \tag{160}$$

The result in the general case of a surfactant of arbitrary solubility is very cumbersome and will not be presented here. Instead, we quote only the limiting case of a vertical wall ($\alpha = 90^o$) and an insoluble surfactant:

$$Re_{c,0} = \frac{15}{4} We \bar{E}, \tag{161}$$

and

$$Re_{c,2} = \frac{5\bar{\sigma}}{4} We + \left( \frac{4825}{1344} - \frac{1}{Pe_a^2} \right) Re_{c,0} + \frac{5}{6Pe_a} Re_{c,0}^2 + \frac{3637}{30888} Re_{c,0}^3. \tag{162}$$

For a clean fluid ($\bar{E} = 0$), this expression reduces to $Re_c = \frac{5}{4} We k^2$ in agreement with what we know from literature [44]. With the addition of surfactant, $Re_{c,0}$ increases from zero and, for typical examples, may eventually reach values of order $10^2$. Thus, the last three terms on the rhs of Eq. (162) (and in particular the third) dominate the first one, and dictate the behavior at non-zero wavenumbers. As a consequence, we expect short wave disturbances to stabilize drastically in comparison to the clean fluid.

### 2.3.4 Conclusions

We extended the analysis for the physical mechanism proposed by [7] and [8] for the initiation and growth of a long-wave instability in liquid film flow, in order to account for the presence of a surfactant of arbitrary solubility in the bulk. The zero order, longitudinal flow perturbation (which is known to result from the perturbation shear stress which develops along the deformed interface) was shown to produce a convective flux that disrupts the uniform interfacial concentration of surfactant. As a consequence of mass conservation, this convective flux builds up an interfacial concentration gradient that, at leading order, is in-phase with the deformation of the interface. The stabilizing effect of the resulting Marangoni stresses appears in the first order flow perturbation, as an additional term assisting gravity in draining fluid from the deformation crest.

The effect of surfactant solubility is apparent in the analytic expression derived for the critical conditions, and indicates that the interfacial concentration gradient, which is responsible for the Marangoni stresses, decreases with increasing solubility. This behavior is explained by considering mass exchange between the interface and the bulk, which at first order is $90^o$ out of phase with the deformation, and contributes a flux that opposes the effect of the zero order flow perturbation. More specifically, it drains surfactant from the node preceding the deformation crest and brings surfactant to the node following it.

It is observed that, for a specific surfactant (constant value of the solubility parameter, $\xi_a$), the extent of flow stabilization is a non-monotonic function of surfactant concentration at the interface, i.e. the critical Reynolds, $Re_{c,0}$ number attains maxima at intermediate values of $\Gamma$. This is explained in terms of the aforementioned mass exchange with the bulk solution, which intensifies as the amount of surfactant increases.

Higher-order terms are calculated (at the expense of rapidly escalating algebraic complexity) and provide information on the effect of disturbances of finite wavelength. Apart from surfactant solubility, which remains of central importance, the speed of adsorption/desorption at the interface starts to play a role. This is clearly an effect of finite wavelength, given that for disturbances of infinite length there is always enough time for the bulk to reach equilibrium with the temporally varying interfacial concentration. As the disturbance becomes shorter, the bulk concentration may lag in phase with respect to the interface. The magnitude of this lag depends exclusively on the dimensionless parameter $\xi_a k_a$, which is the ratio of the characteristic times of convection and adsorption.

Finally, the first correction due to finite wavelength is calculated for the phase velocity of the disturbance and for the critical Reynolds number of the primary instability. The expressions are very cumbersome, and are presented and discussed mainly for the case of an insoluble surfactant. Compared to the results at this order for a clean liquid, the phase velocity is found to decrease with wavenumber, and the critical Reynolds is found to increase strongly.

# 3 Non-linear dynamics of a viscoelastic film subjected to a spatially periodic electric field

## 3.1 Indroduction

The interaction of an externally applied electric field with a liquid can give rise to interesting flow instabilities and pattern formation [45]. The work of Russel and co-workers [46, 47, 48, 49, 50] has demonstrated that the application of an electric field to an initially flat polymer-air or polymer-polymer interface results in an electrohydrodynamic (EHD) instability leading to the formation of columnar structures. These instabilities can be used in order to form well-controlled patterns at the microscale and nanoscale with many practical engineering applications.

The electrically-induced flow of thin liquid films has attracted the interest of many theoretical studies. More specifically, Schaffer *et al.* [47] used the lubrication approximation to determine the dependence of the fastest growing linear mode on system parameters for a polymer-air interface. Lin *et al.* [48] conducted experimental as well as theoretical work to study the dependence of pattern wavelength on the viscosity ratio in two-layer polymeric systems. Their modelling study predicts the wavelength to be independent of the viscosity ratio for perfect dielectric fluids. Pease & Russel [51] considered the stability of the interface between a leaky dielectric liquid and air and showed that the

presence of conductivity exerts a destabilizing influence leading to patterns of smaller wavelength and much larger growth rates. Shankar & Sharma [52] also conducted a linear stability analysis using lubrication theory and their results indicate that, in contrast to the perfect dielectric case, for leaky dielectrics, increasing the viscosity ratio has a profound influence on the pattern wavelength.

More recently, Heier *et al.* [53] were interested in systems with heterogeneous electric fields and showed through experiments that it is possible to achieve a steady state with finite interfacial deformation when Maxwell stresses in the fluids and surface tension are balanced. They also developed a linear model and were able to derive an expression for the critical voltage beyond which the amplitude grows exponentially in qualitative agreement with their experiments. However, it should be noted that according to Heier *et al.* [53] linear theory severely underestimates the amplitude of the steady finite deformations in comparison with experimental observations.

The nonlinear evolution of two leaky dielectric layers in a homogeneous electric field was examined by Craster & Matar [54] showing that initially small perturbations grow under the action of the destabilizing electrical forces and eventually their amplitude saturates in the non-linear regime to give rise to spatially periodic patterns. Two-dimensional numerical simulations using the lubrication theory helped in elucidating the interfacial evolution, the role of the initial thickness ratio and the effect of patterned "masks" on the observed three-dimensional patterns [55, 56, 57, 58]. Several studies have also been devoted in the investigation of the stability and dynamics of bilayers under air or another viscous liquid [59, 60, 61, 62, 63]. Finally, the effect of AC fields has been taken into account through linear stability analysis and non-linear simulations by Roberts & Kumar [64] and Gambhire & Thaokar [65].

As discussed above, the surface instability of a Newtonian fluid under the effect of electric field has been studied extensively by several researchers and it is now well understood. The dynamics of fluids with complex rheology, however, has received much less attention in the literature. The first attempt to take into account the polymer viscoelasticity in electrically-induced flows was made by Wu & Chou [66]. These researchers used the lubrication theory and performed a linear stability analysis of a initially static thin polymer film underneath a flat electrode using the Oldroyd-B consitutive equation for the elastic stresses. Their results have shown that the polymer elasticity destabilizes the system and when the Deborah number is large enough, a resonant phenomenon appears as a result of the interaction between the two destabilizing mechanisms (the electrostatic force and the polymer elasticity). Later on, Tomar *et al.* [67] used a linear constitutive equation for the stresses (Jeffreys model) and presented a linear stability analysis taking also into account the effect of inertia. Interestingly, they found that in the presence of a small amount of inertia the wavelength of the fastest growing mode (i.e. the dominant lengthscale of the instability) is independent of the rheological properties such as relaxation time and solvent viscosity whereas the growth rate is affected significantly. Their findings were confirmed recently by Espin *et al.* [68] using an asymptotic expansion. The latter authors also examined the viscoelastic effects under the influence of AC

fields and found that the impact is largest when the relaxation time and oscillation time scale are comparable. In the case of AC fields, it is shown that the wavelength is also affected contrary to the predictions of linear theory for the case of DC fields [67]. The rheological characteristics of the fluid were also shown to play a role in the case of trilayers, indicating that its effect on the evolution of two coupled interfaces is more involved than a purely kinetic role [69]. It should be noted here that the aforementioned studies for viscoelastic fluids considered homogeneous electric fields (flat electrodes) and the linear stability analysis was performed around a quiescent base state. However, in the case of a patterned mask the field becomes heterogeneous and growth generates a time-dependent base state for which linear or weakly non-linear stability analysis is difficult necessitating the use of time-dependent simulations.

As was noted above, most of the research studies in the literature employ linear theory, which is valid only for small disturbances. One crucial issue, however, is not only to predict the band of unstable wavenumbers in the linear regime but also to determine accurately the behavior of the system in the non-linear regime. For the latter, the majority of the research groups make use of the lubrication theory in order to interpret experimental results. Pease & Russel [70, 71] argued, however, that in many cases the experiments were carried out for conditions under which the lubrication approximation is not strictly valid. They compared the predictions of a generalised model with those of lubrication theory against experimental results and found a better agreement with the former. Very recently, a detailed comparison was also presented by Gambhire & Thaokar [65] for both DC and AC fields, which indicated large deviations for the predicted wavelength. Moreover, in the case of viscoelastic fluids, the deficiencies of the lubrication approximation are expected to be enhanced due to the significant underestimation of normal stresses and to the fact that non-linear viscoelastic effects are not taken into account.

Examples of fully non-linear simulations without making use of the lubrication approximation are the works of [72, 73, 74, 75] who studied primarily cases involving heterogeneous electric fields. Yang *et al.* [74], motivated by the work of Heier *et al.* [53], considered a sinusoidally patterned top electrode and performed non-linear simulations using a bounary/finite element method to determine the critical parameters for instability of the liquid film. Their results indicate that linear analysis can significantly over-predict the critical voltage for instability. Li *et al.* [75] were also interested in heterogeneous electric fields and investigated the effect of various geometric features of the patterned electrode to determine the fabrication limits of this process using a diffuse interface method.

The scope of this work is to investigate the non-linear dynamics of a viscoelastic material under the influence of an heterogeneous electric field taking fully into account the viscoelastic effects. We avoid making any assumptions, such as using lubrication approximation, in order to describe the flow dynamics as accurately as possible. We perform two-dimensional transient numerical simulations, using the finite element method combined with an elliptic grid generation scheme for the determination of the unknown position of the interface. The viscoelasticity of the polymeric film is taken into account using the affine

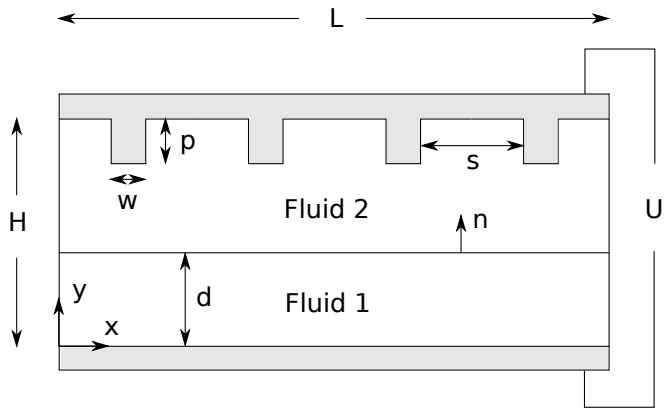


Figure 22: Schematic of the flow geometry

Phan-Thien Tanner model. We perform an extensive parametric analysis to determine the effects of the various geometric and rheological parameters on the evolution of the interface and on the fabrication limits of this process. Our results indicate that the elasticity of the material does not affect the critical voltage for instability but affects the fabrication limit on the period of the top electrode protrusions. We also discuss about the validity of lubrication theory in the case of viscoelastic materials.

The remainder of this chapter is organized as follows. In Section 3.2, we describe the system of governing equations and outline the numerical method used for its numerical solution. The results are presented and discussed in Section 3.3. Finally, the concluding remarks are given in Section 3.4.

## 3.2 Problem formulation

We consider the dynamics of two perfect dielectric fluids sandwiched between two rigid, and impermeable electrodes. The electrodes can be either flat or periodically patterned as shown in Fig. 42; $w$ and $p$ denote the width and the height of the protrusions, respectively, and $s$ denotes the spacing between the protrusions. The bottom fluid is considered to be a polymeric viscoelastic film surrounded by a Newtonian liquid, with initial thickness, $d$. Both fluids, which are initially stationary, are taken to be incompressible with the lower (upper) fluid having a density $\rho_1$ ($\rho_2$), dielectric constants $\epsilon_1$ ($\epsilon_2$); these properties are assumed to be constant. The viscosity of the upper fluid is also constant and denoted by $\mu_2$. The viscoelastic fluid has a zero-shear viscosity $\mu_1 = \mu_s + \mu_p$, where $\mu_s$ and $\mu_p$ are the viscosities of the solvent and the polymer, respectively, and relaxation time $\lambda$. The surface tension of the liquid-liquid interface, $\sigma$, is assumed to be constant. The top and bottom electrodes are maintained at constant potentials $\phi_2(y = H(x)) = U$ and $\phi_1(y = 0) = 0$, respectively.

We scale all lengths with the maximum distance between the top and bottom

electrodes, $H_m$, velocities with $V^* = \epsilon_o U^2/(\mu_1 H_m)$, pressure and stresses with $\mu_1 V^*/H_m$ and electric potential with the potential difference $U$. Substituting this scaling into the governing equations and boundary conditions, the dimensionless groups that emerge are the Reynolds number, $Re = \rho_1 V^* H_m/\mu_1$, the Stokes number, $St = \rho_1 g H_m^2/(\mu_1 V^*)$, the capillary number, $Ca = \mu_1 V^*/\sigma$, the Weissenberg number, $Wi = \lambda V^*/H_m$, which is a measure of the elasticity of the polymeric liquid, the density ratio, $D_i = \rho_i/\rho_1$, the viscosity ratio, $M_i = \mu_i/\mu_1$, and the solvent viscosity ratio of the polymer liquid, $\beta = \mu_s/\mu_1$.

Inserting the previously defined characteristic quantities into the momentum and mass conservation equations, we obtain:

$$D_i \mathrm{Re}\left(\frac{\partial \mathbf{v}_i}{\partial t} + \mathbf{v}_i \cdot \nabla \mathbf{v}_i\right) - \nabla \cdot T_i + \mathrm{St}\mathbf{e}_z = 0, \tag{163}$$

$$\nabla \cdot \mathbf{v}_i = 0, \tag{164}$$

where $\nabla$ denotes the gradient operator, subscript $i$ indicates the corresponding fluid, $\mathbf{v}_i$ is the velocity vector and $T_i$ is the total stress tensor given by

$$T_i = -P_i I + \tau_i + m_i. \tag{165}$$

Here $P_i$ denotes the pressure, $I$ is the identity tensor and $\tau_i$ the extra stress tensor

$$\tau_1 = \tau_{p,1} + 2\beta M_1 \gamma_1, \tag{166}$$

$$\tau_2 = 2M_2 \gamma_2. \tag{167}$$

Note that for the viscoelastic material the extra stress tensor is split into a purely viscous part, $2\beta M_1 \gamma_1$, and a polymeric contribution, $\tau_{p,1}$. $\gamma_i$ denotes the rate of strain tensor

$$\gamma_i = \frac{1}{2}\left(\nabla \mathbf{v}_i + \nabla \mathbf{v}_i^T\right). \tag{168}$$

The Maxwell stress tensor, denoted by $m_i$, describes the interaction of fluid $i$ with the electric field, $\mathbf{E}_i$, and is defined as

$$m_i = \epsilon_i \mathbf{E}_i \mathbf{E}_i - \frac{1}{2}\epsilon_i \mathbf{E}_i \cdot \mathbf{E}_i I. \tag{169}$$

Note that due to the absence of free charge from the bulk of the fluid and since $\epsilon_1$ and $\epsilon_2$ are spatially independent, $\nabla \cdot m_i = 0$. Therefore it becomes evident that Maxwell stresses will not have any contribution in eq. (202) but nevertheless enter the problem through the interfacial boundary conditions. The Maxwell stresses depend on the local intensity of the electric field. Under the electrostatic approximation and for an electrically neutral fluid, Maxwell's equations reduce to the following set of equations

$$\nabla \cdot (\epsilon_i \mathbf{E}_i) = 0, \tag{170}$$

$$\nabla \times \mathbf{E}_i = 0. \tag{171}$$

Since the electrical field is irrotational, we can define a potential function $\phi_i$ such that

$$\mathbf{E}_i = -\nabla\phi_i. \tag{172}$$

By combining eq. (209) and eq. (211) we get the following equation

$$\nabla \cdot (\epsilon_i \nabla\phi_i) = 0. \tag{173}$$

To complete the description, a constitutive equation that describes the rheology of the viscoelastic material is required in order to determine the polymeric part of the extra stress tensor. As such, we use the following differential model that has been proposed by [76]

$$Y(\tau_{p,1})\tau_{p,1} + \mathrm{Wi}\hat{\tau}_{p,1} = 2(1-\beta)M_1\gamma_1. \tag{174}$$

The symbol $\hat{}$ over the viscoelastic stress denotes the Gordon-Schowalter derivative defined as

$$\hat{X} = \frac{\partial X}{\partial t} + \mathbf{v}_1 \cdot \nabla X - (\nabla\mathbf{v}_1 - \xi_s\gamma_1)^T \cdot X - X \cdot (\nabla\mathbf{v}_1 - \xi_s\gamma_1), \tag{175}$$

where $X$ is any second order tensor. Two forms of the PTT model are in common use, the linearised form [76], where the function $Y(\tau_{p,1})$ is

$$Y(\tau_{p,1}) = 1 + \frac{a_{PTT}\mathrm{Wi}}{(1-\beta)M_1} tr(\tau_{p,1}), \tag{176}$$

and the exponential form [77]

$$Y(\tau_{p,1}) = \exp\left[\frac{a_{PTT}\mathrm{Wi}}{(1-\beta)M_1} tr(\tau_{p,1})\right]. \tag{177}$$

In the present study we have used the exponential form of the PTT model. Both versions of the PTT model have two parameters, $\xi_s$ and $a_{PTT}$. The first one is related to the non-affine motion of the polymer chains with respect to the macroscopic motion of the continuum. By setting $\xi_s$ equal to zero no such motion or slip is allowed; for the rest of the paper $\xi_s$ will be considered to be zero. The Gordon-Schowalter derivative reduces to the upper convective one and the fluid model is referred to as the affine PTT model. The second parameter, $a_{PTT}$, imposes an upper limit to the elongational viscosity, which increases as this parameter decreases, while it introduces elongational thinning. Moreover $a_{PTT}$ is related to the shear-thinning behavior of the model. The predictions for the elongational and shear viscosity of this model for various values of $a_{PTT}$ appear in Fig. 9 of [42]. By setting both $a_{PTT} = 0$ and $\xi_s = 0$, the PTT model reduces to the Oldroyd-B model. Retaining the zero values for $a_{PTT}$ and $\xi_s$ and additionally setting $\beta = 0$, the PTT model reduces to the UCM model.

In order to solve accurately and efficiently the flow inside the viscoelastic material we employ the elastic viscous split stress EVSS-G formulation [78, 79].

This method consists of splitting the polymeric part of the extra stress tensor into a purely elastic and a viscous part

$$\tau_{p,1} = \Sigma + 2(1-\beta)M_1\gamma_1. \tag{178}$$

Moreover, an independent interpolation of the components of the velocity gradient tensor is introduced

$$G = \nabla \mathbf{v}_1. \tag{179}$$

The former splitting ensures the elliptic nature of the momentum equations even in the absence of a solvent ($\beta = 0$), while the latter substitution makes the approximations in the constitutive equation of the elastic stress and the velocity gradient compatible to each other. This scheme has been used with success in the past [42, 80, 81] permitting the calculations up to very high Weissenberg numbers.

### 3.2.1 Boundary conditions

Solution of the above set of equations is determined subject to the following boundary conditions.

On the solid walls we apply the usual no-slip and no-penetration boundary conditions while on the two edges of the physical domain ($x = 0, L$) we apply periodic conditions.

Along the liquid-liquid interface the velocity is continuous

$$\mathbf{v}_1 = \mathbf{v}_2, \tag{180}$$

and the flow field satisfies the local interfacial force balance between the stresses in both liquids

$$\mathbf{n} \cdot T_1 = \mathbf{n} \cdot T_2 + \frac{2\mathcal{H}\mathbf{n}}{\mathrm{Ca}}, \tag{181}$$

where $\mathbf{n}$ denotes the unit normal pointing towards the upper liquid, $2\mathcal{H}$ is the mean curvature of the interface

$$2\mathcal{H} = -\nabla_s \cdot \mathbf{n}, \tag{182}$$

and $\nabla_s$ is the surface gradient operator, defined as

$$\nabla_s = (I - \mathbf{nn})\,\nabla. \tag{183}$$

In addition, along the moving interface we impose the kinematic boundary condition,

$$\frac{\partial f}{\partial t} + \mathbf{v}_i \cdot \nabla f = 0, \tag{184}$$

where $f$ describes the position of the interface. A balance of the normal and tangential component of the electric field gives the continuity of the potentials and the electric displacement across the interface

$$\phi_1 = \phi_2, \tag{185}$$

$$\mathbf{n} \cdot (\epsilon_1 \nabla \phi_1) = \mathbf{n} \cdot (\epsilon_2 \nabla \phi_2). \tag{186}$$

Finally to complete our model we have to set a datum pressure and as such, we impose a zero value to the pressure at a node of the top electrode, $P(x = 0, y = 1) = 0$. Initially the film is considered to be static and the liquid-air interface is flat; no initial perturbation is applied.

### 3.2.2 Elliptic grid generation

The above set of equations is combined with an elliptic grid generation scheme capable of following the deformations of the physical domain. This method has been successfully applied in flows that exhibit large deformations in steady state [80] and transient calculations [82, 83, 84]. The grid generation scheme consists of a system of quasi-elliptic partial differential equations, capable of generating a boundary fitted discretization of the deforming domain occupied by the liquid. With this scheme the physical domain $(x, y)$ is mapped onto a computational one $(\eta, \xi)$. A fixed computational mesh is generated in the latter domain while, through the mapping, the corresponding mesh in the physical domain follows its deformations. The mapping is based on the solution of the following system of quasi-elliptic partial differential equations

$$\nabla \cdot (\alpha \cdot \nabla \eta) = 0 \tag{187}$$

$$\nabla \cdot \left[ \left( \delta \sqrt{\frac{x_\xi^2 + y_\xi^2}{x_\eta^2 + y_\eta^2}} + (1 - \delta) \right) \nabla \xi \right] = 0 \tag{188}$$

where

$$\alpha = \begin{pmatrix} 1 & 0 \\ 0 & a \end{pmatrix}, \; a \geq 1. \tag{189}$$

The subscripts denote differentiation with respect to the indicated variable. The parameter $a$ forces the $\xi$-coordinate lines to be equidistant in the $y$-direction and $\delta$ is a parameter that controls the smoothness of the mapping relative to the degree of orthogonality of the mesh lines. These parameters are adjusted by trial and error; here we set $a = 100$ and $\delta = 0.1$. For a more detailed description of this method the interested reader may refer to [85, 86, 87].

In order to solve the above system of differential equations, appropriate boundary conditions must be imposed. On the fixed boundaries, we impose the equations that define their position, and the remaining degrees of freedom are used for optimally distributing the nodes along these boundaries. Along the moving liquid-liquid interface we simply impose the kinematic equation.

We should note here that special care was taken for the mesh near the interface. In order to resolve adequately the flow, a more refined mesh around this region is needed. To this end, we have introduced a local refinement scheme using the h-method [88]. In order to illustrate the quality of the resulting mesh produced following our method we present in Fig. 43 a typical grid; here we show for clarity the domain $1 < x < 3$.

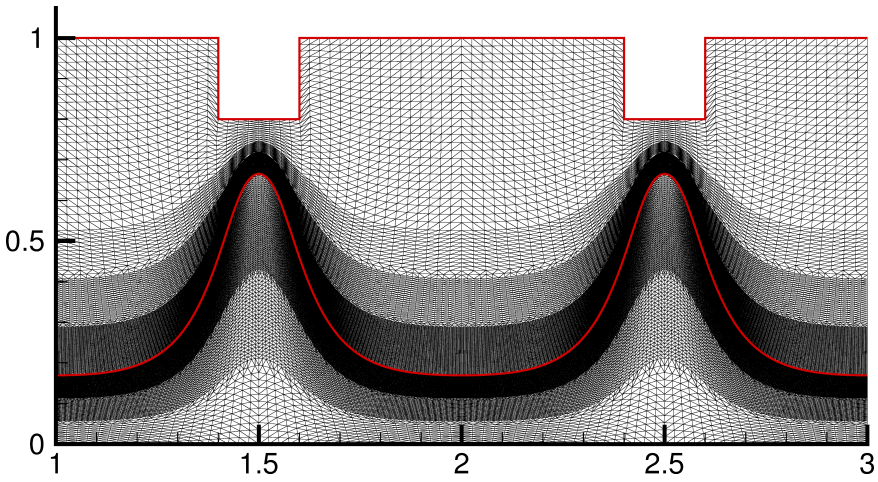


Figure 23: (Color online) Typical grid with 3 levels of local refinement adjacent to the liquid-liquid interface for Wi = 0, Ca = 30, $d = 0.3$, $s = 0.8$, $p = 0.2$, $w = 0.2$, $L = 4$ at time $t = 26.04$.

In order to solve numerically the governing equations along with the elliptic grid equations, we used the mixed finite element method; this numerical scheme has been used with success in the past [82, 80, 81, 83, 42]. Detailed information about the weak formulation of all the equations is given in the 3.5. Finally, the set of algebraic equations is integrated in time with the implicit Euler method introducing an automatic adaptation of the time step for ensuring the convergence of the above iteration scheme and optimizing code performance.

## 3.3 Results

As shown in Fig. 42 we consider a periodically patterned electrode as a mask to induce the fabrication of similar structures in the liquid. For the purposes of this study we will consider that the width and the height of the protrusions are $w = 0.2$ and $p = 0.2$, respectively. Since the effect of these geometric characteristics have been discussed in detail for the case of a Newtonian liquid by [75], we will keep these values constant and focus our attention on the remaining parameters of our model. The size of the domain will be considered to be $L = 4(s + w)$ unless stated otherwise. For the rest of the paper we will also consider creeping flow conditions and set $Re = 10^{-5}$, ignore gravitational effects, $St = 0$, and consider density and viscosity ratios typical of liquid-air systems, $D_2 = 0.001$, $M_2 = 0.001$.

### 3.3.1 Newtonian fluid

To set the stage for the discussion that follows, it is useful to examine first the case of a Newtonian fluid ($Wi = 0$). In Fig. 24 we present contour plots for the

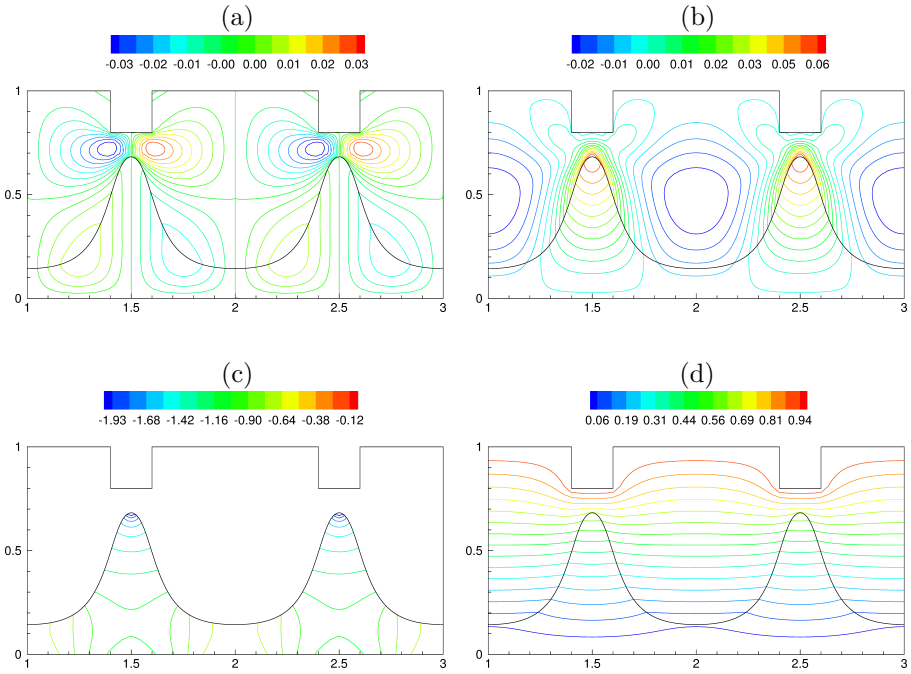


Figure 24: (Color online) Contour plots of (a) $v_x$, (b) $v_y$, (c) $P$ and (d) electric potential at $t = 26.04$ for $Wi = 0$, $Ca = 30$, $\epsilon_1 = 2.5$, $\epsilon_2 = 1$, $d = 0.3$, $s = 0.8$, $p = 0.2$, $w = 0.2$, $L = 4$.

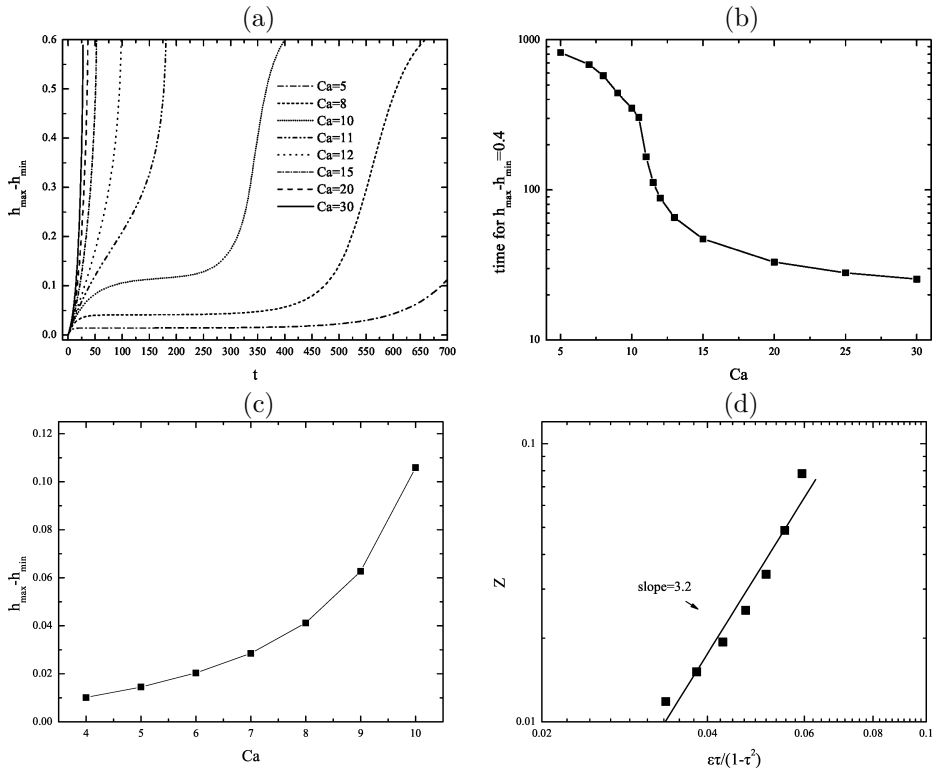


Figure 25: (a) Evolution of the amplitude for various Ca. (b) Time that is needed for $h_{max} - h_{min} = 0.4$ as a function of the Ca number. Dependence of (c) $h_{max} - h_{min}$ on Ca at $t = 100$ for various Wi and (d) the dimensionless amplitude $Z$ on $\epsilon\tau/(1-\tau^2)$. The remaining parameters are Wi $= 0$, $\epsilon_1 = 2.5$, $\epsilon_2 = 1$, $d = 0.3$, $s = 0.8$, $p = 0.2$, $w = 0.2$, $L = 4$

velocity field, pressure and electric potential at $t = 26.04$ for $Ca = 30$, $d = 0.3$ and $s = 0.8$; for clarity we present here only part of our computational domain ($1 \leq x \leq 3$). The liquid film is initially flat and quiescent. Upon the application of voltage the liquid experiences non-uniform electrostatic forces, due to the spatial heterogeneity of the electric field that is created by the top electrode, and liquid is drawn towards the protrusions, destabilizing the liquid-air interface. The flow field appears to be symmetric around the protrusions giving rise to symmetric structures that follow closely the geometrical characteristics of the top electrode. The pressure varies mainly inside the liquid phase (see Fig. 24c) and becomes minimum at the crest, whereas in the gas phase it remains almost constant (approximately equal to the datum pressure) due to the fact that the viscosity of the gas is very small. The contour lines of the electric potential are depicted in Fig. 24d. The deflection of the equipotential lines at the liquid-air interface is due to the difference of dielectric properties of the materials.

For the given set of parameters the height of the interface below the protrusions increases continuously until the liquid comes into contact with the top electrode; the simulation is stopped before we actually reach that point. Heier *et al.* [53] have shown that by manipulating the combined effect of Maxwell stresses and surface tension it is possible to achieve a steady state interfacial deformation avoiding contact with the top electrode. In order to investigate this possibility, we examine in Fig. 25a the parametric effect of the capillary number, $Ca$, in the temporal evolution of the maximum amplitude of the interfacial perturbation. Recall that $Ca$ compares electric to capillary stresses. For the lowest $Ca$ we confirm that the amplitude initially grows and then saturates, indicating that electric and capillary forces balance exactly. This situation evidently corresponds to a static equilibrium, as there is no driving force for flow. The equilibrium amplitude increases with $Ca$ as depicted in Fig. 25c, and its maximum values are in the order of 10% of the electrode spacing.

According to the linear theory developed by Heier *et al.* [53] the dimensionless amplitude $Z = \zeta_0 \sqrt{k^2(1-d+d/\epsilon_p)/Ca}$, where $\zeta_0 = (h_{max} - h_{min})/2$ and $k = 2\pi/(s+w)$ should depend linearly on $\epsilon\tau/(1-\tau^2)$, where $\epsilon = p/[2(1-d+d/\epsilon_p)]$ and $\tau = (1-1/\epsilon_p)\sqrt{Ca/[k^2(1-d+d/\epsilon_p)^3]}$. Heier *et al.* [53] correlated experimental data of $Z$ by a power-law dependence on $\epsilon\tau/(1-\tau^2)$, and found that the exponent is not equal to one -as expected from their linear theory- but actually is much higher, approximately equal to 4.5. The results of our non-linear calculations, plotted in terms of the above dimensionless parameters, are shown in Fig. 25b. We observe that the correlation by a power-law is not completely satisfactory, as the slope in log-log coordinates gradually increases. However, an approximate value for the exponent is 3.2, which is significantly higher than the linear prediction and a bit lower than the experimental value.

The long-time results depicted in Fig. 25a indicate that the equilibrium state is not stable but is eventually destroyed and some peaks reach the upper electode. The process by which the interface disintegrates is shown in Fig. 26 for $Ca = 8$ and involves loss of the spatial periodicity imposed by the electode spacing. We note however that the time-scale for this process is at low $Ca$ an order of magnitude higher than the time-scale for growth of the equilibrium amplitude. Thus, the equilibrium state may actually be considered as metastable.

Increasing the $Ca$ number, the effect of surface tension becomes less significant and the destabilization of the interface takes place sooner. Plotting the time that is needed for $h_{max} - h_{min} = 0.4$ (a convenient arbitrary criterion) it is possible to evaluate the threshold in the $Ca$ number beyond which the metastable state is not observed (see Fig. 25b) and we find that for the given set of parameters it is approximately equal to $Ca \approx 10$. According to linear theory [53, 74] the critical $Ca$ can be evaluated using the following expression

$$Ca_{cr} = k^2 \frac{[\epsilon_p(1-p/2-d)+d]^3}{\epsilon_p(\epsilon_p-1)^2}, \tag{190}$$

where $k$ is the wavenumber of the interfacial perturbation which is assumed to largely follow the pattern of the top electrode. For the given set of parameters

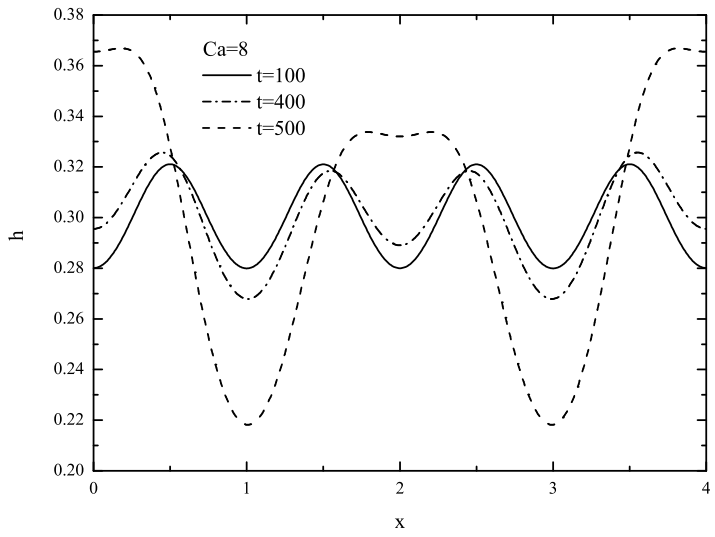


Figure 26: Profiles of the liquid-air interface for Ca = 8 at t=100,400,500. Wi = 0, $\epsilon_1 = 2.5$, $\epsilon_2 = 1$, $d = 0.3$, $s = 0.8$, $p = 0.2$, $w = 0.2$, $L = 4$

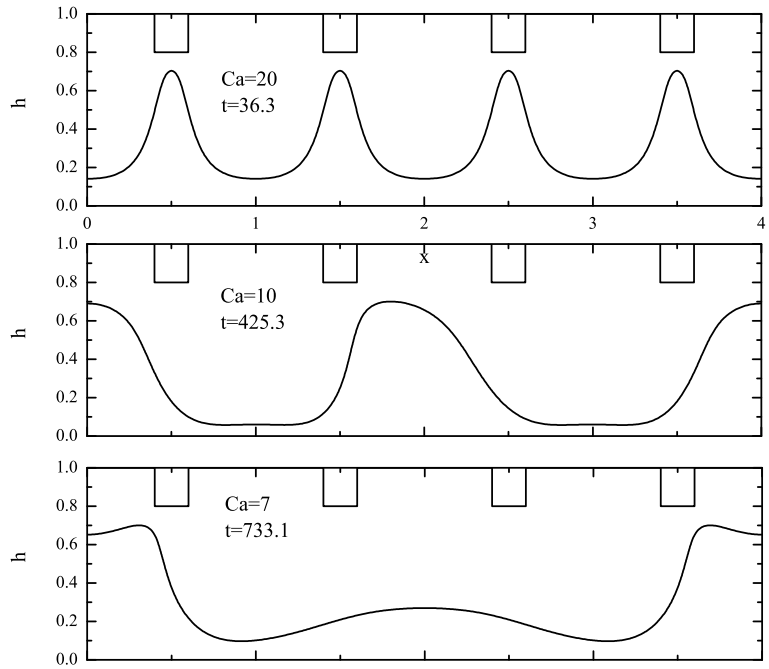


Figure 27: Long time profiles of the liquid-air interface for various Ca and for Wi = 0, $\epsilon_1 = 2.5$, $\epsilon_2 = 1$, $d = 0.3$, $s = 0.8$, $p = 0.2$, $w = 0.2$, $L = 4$

and assuming that the dimensionless wavelength of the initial disturbance is approximately equal to $s + w$, we get $Ca_{cr} = 40.89$. It appears that linear theory significantly over-predicts the critical voltage and this was also found to be true in the non-linear simulations presented by [74].

The loss of interfacial periodicity that is observed in the evolution of the metastable equilibrium appears to be a more general characteristic of the present problem. In support of this argument, we present in Fig. 27 the long-time profiles of the liquid-air interface for three different values of the $Ca$ number. We observe that for values higher than the 'critical' $Ca$ the deformation of the interface remains periodic, following closely the spatial periodicity imposed by the top electrode, during the entire evolution toward formation of columnar structures. On the other hand, for low $Ca$ the spatial periodicity of the interface is eventually destroyed, despite the initial periodicity of the metastabe state. The evolution is always a coarsening process similar to the one described in [89]. More specifically, some pillars expand at the expense of shrinkage of their neighbours and this is essentially an Ostwald ripening phenomenon.

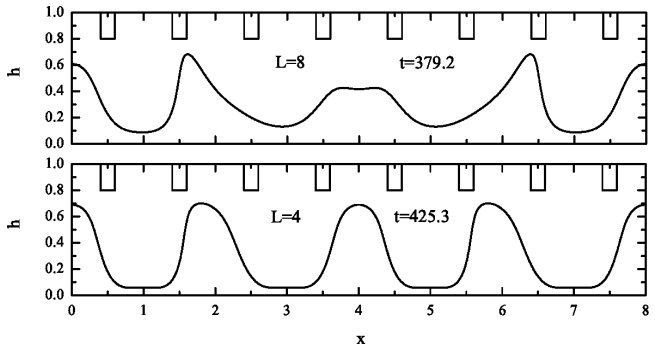


Figure 28: Long time profiles of the liquid-air interface for different sizes of the computational domain for Wi = 0, Ca = 10, $\epsilon_1 = 2.5$, $\epsilon_2 = 1$, $d = 0.3$, $s = 0.8$, $p = 0.2$, $w = 0.2$

The mechanism responsible for the ripening process can be rationalized as follows. Initially, the wavelength of the interface perturbation is imposed by the pattern of the electrode which induces non-uniform Maxwell stresses to the interface. Note that for the parameters that have been used in this study the wavelength is 2-5 times smaller than the wavelength of the fastest growing mode which is predicted by linear theory for flat electrodes. Even though this represents a barrier which is set by the effect of surface tension it can be overcome due the effect of the heterogeneous electric field. For cases that growth is sufficiently fast, the mode which is imposed by the patterned electrode will dominate and the pattern of the electrode will be replicated in the film retaining its periodic structure. On the other hand, if growth is relatively slow or the system reaches equilibrium the mode of the natural wavelength, which is dominated by the effect of surface tension, is given the time to grow and eventually dominate the flow.

One question that arises is whether these non-periodic solutions are physically meaningful or are affected in any way by the size of our domain and the application of periodic conditions at the edges. To investigate this, we have repeated the calculations for $Ca = 10$ doubling the size of the computational domain and the long-time profile of the interfacial height is presented in Fig. 28. Note that the solution for the short domain have been extended periodically in the $x$-direction. Comparing the results for the two domains we find that, although the profiles present some similarities, they are far from identical. Nevertheless, we observe that in both cases the structures evolve by a rough doubling of the spatial periodicity that results from merging of neighbouring crest, with the growing hump "hesitating" between the respective electrode protrusions. Still, we are unable to conclude if the evolution by period-doubling is a general trend or is dictated by the imposed periodic boundary conditions. For $Ca = 20$ the solutions using the sort or long domain are identical and are not presented here for conciseness.

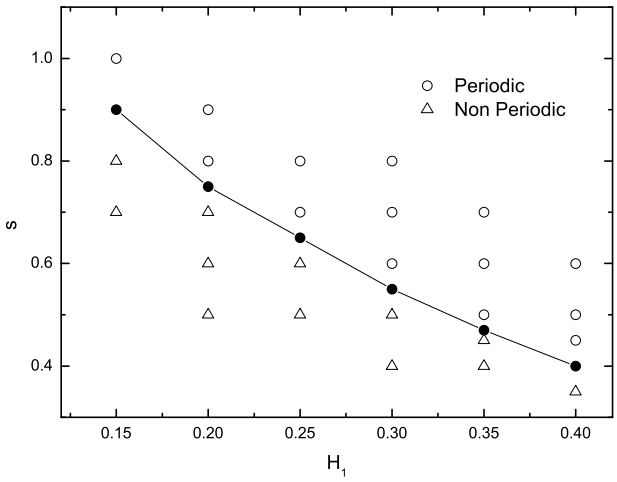


Figure 29: Flow map for Wi = 0, Ca = 20, $\epsilon_1 = 2.5$, $\epsilon_2 = 1$, $p = 0.2$, $w = 0.2$, $L = 4(s + w)$.

In practice in order to produce well-ordered polymeric micro-structures over large distances it is important to operate in conditions where the induced structures are periodic. Apart from using the applied voltage to control the induced patterns, as shown above, it is also possible to tune the film thickness and the geometrical characteristics of the top electrode such as the periodicity of the protrusion as well as their width and depth. In Fig. 29 we depict a flow map to investigate the various flow patterns that may arise for various distances of the protrusions and different mean initial thickness of the polymer. Our calculations indicate the existence of two different regimes. The circles denote the regime where the induced structures are periodic whereas the triangles correspond to non-periodic solutions. These are separated by a curve with filled circles which is used to indicate near critical conditions. To determine whether the pattern is periodic or not, we evaluate the standard deviation of the position of each peak from the mean value, $\bar{h}_p$, when the highest peak has reached $h = 0.7$. If the standard deviation is lower than 0.001 then the structure is considered periodic whereas for higher values the structure is considered to be non-periodic. From fig. 29 we deduce that increasing the initial film thickness, $d$, the minimum distance of the protrusions decreases significantly and therefore the fabrication limit of the induced patterns decreases as well. A similar configuration to ours was studied recently by Li *et al.* [75] using a diffuse interface method and it would be useful to compare their predictions for the period limit of the protrusions against our calculations using the sharp interface approach. For the fluid

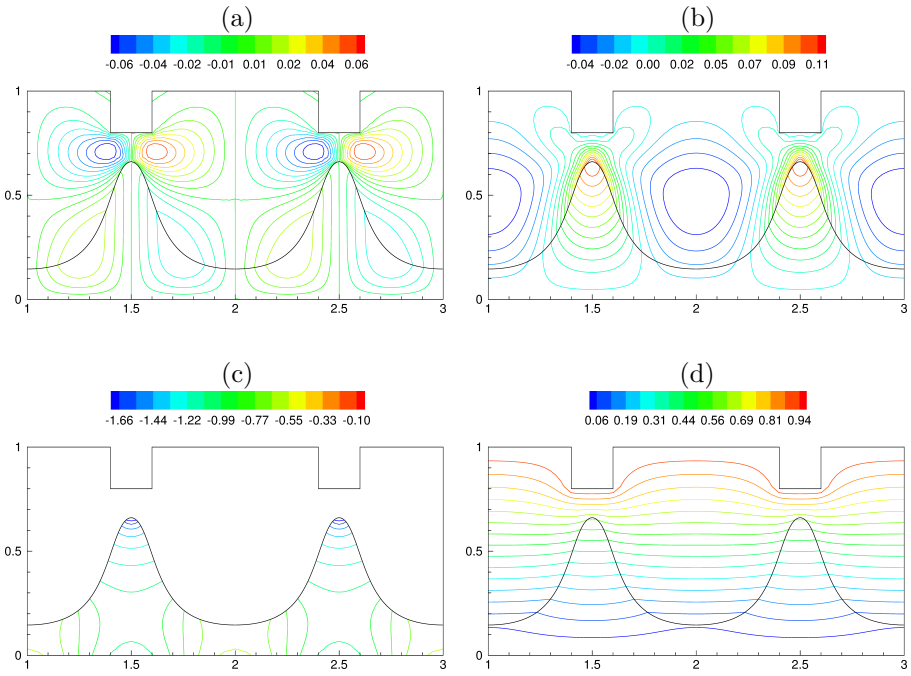


Figure 30: (Color online) Contour plots of (a) $v_x$, (b) $v_y$, (c) P and (d) electric potential at $t = 28.44$ for $Wi = 2$, $Ca = 20$, $\beta = 0$, $a_{PTT} = 0.05$, $\epsilon_1 = 2.5$, $\epsilon_2 = 1$, $d = 0.3$, $s = 0.8$, $p = 0.2$, $w = 0.2$, $L = 4$.

properties ($\sigma = 0.038$ N/m) and applied voltage (70 V) that were used by Li *et al.* [75] we deduce that Ca $\approx 11.4$. For this set of parameters we get that the predicted critical distance between the electrode protrusions is approximately equal to $s = 0.85$ which is in very good agreement with the predictions presented by these authors.

### 3.3.2 Viscoelastic fluid

Next we proceed with our investigation taking into account the effect of viscoelasticity of the polymeric film by studying the case of a PTT fluid. To start with, we present in Fig. 30 contour plots for the velocity field, pressure and electric potential at $t = 28.44$ for $Wi = 2$, $Ca = 20$, $d = 0.3$ and $s = 0.8$; for clarity we present here only part of our computational domain ($1 \leq x \leq 3$). As in the case of the Newtonian fluid for the given set of parameters we end up with a symmetric flow field around the protrusions and the induced structures are also symmetric. The velocity in the normal direction at the crest is higher and as a result the crest reaches the same height sooner for the case of the viscoelastic fluid than a Newtonian fluid with similar surface tension. Though this trend agrees with the findings of linear theory (which suggests that the

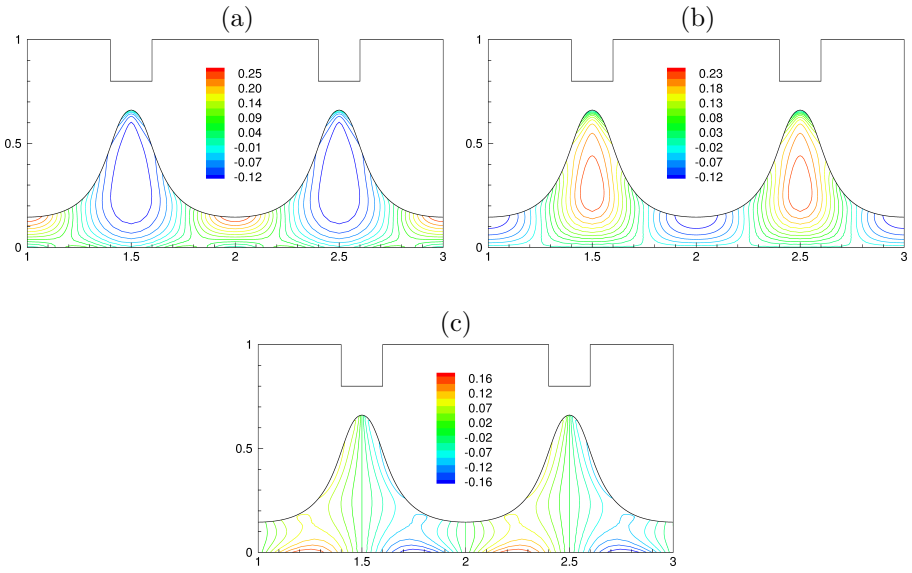


Figure 31: (Color online) Contour plots of (a) $\tau_{p,xx}$, (b) $\tau_{p,yy}$ and (c) $\tau_{p,xy}$ at $t = 28.44$ for $Wi = 2$, $Ca = 20$, $\beta = 0$, $a_{PTT} = 0.05$, $\epsilon_1 = 2.5$, $\epsilon_2 = 1$, $d = 0.3$, $s = 0.8$, $p = 0.2$, $w = 0.2$, $L = 4$.

growth rate increases with the elasticity of the material [66, 67]), the behavior at finite deformations is presently interpreted differently in terms of the normal and shear stresses.

Iso-contours of the polymeric part of the stress components at an advanced stage of interfacial deformation is depicted in Fig. 31. The values of these components along the interface are plotted in Fig. 32 for two different times, corresponding to early (linear) and advanced (nonlinear) stage of the pillar growth. (We note that the contour lines given here and subsequently in this paper have been derived from the raw data without any post-processing for smoothing them. In spite of the sharp variations of stress components near the crests of the film, these contour lines remain smooth throughout the simulations. Apparently $\tau_{p,xx}$ and $\tau_{p,yy}$ develop boundary layers on the front, the accurate resolution of which required the local mesh refinement described earlier.)

As intuitively expected -and also concluded from Fig. 31b- the normal stress, $\tau_{p,yy}$, is extentional in the core of the crest and thus resists elongation of the pillar. However, Fig. 32 indicates that the relative intensity of this resistance decreases with deformation, as $\tau_{p,yy}$ is proportional to deformation at the linear stage but strongly displaced towards lower values later. The explanation of this relaxation is provided by the behavior of the normal stress $\tau_{p,xx}$, which retains negative -i.e. compressive- values along the core of the pillar. The compressive $x$-component acts to thin the pilar and thus relaxes polymeric stresses in the $y$-direction. Finally, the shear component $\tau_{p,xy}$ also resists deformation according

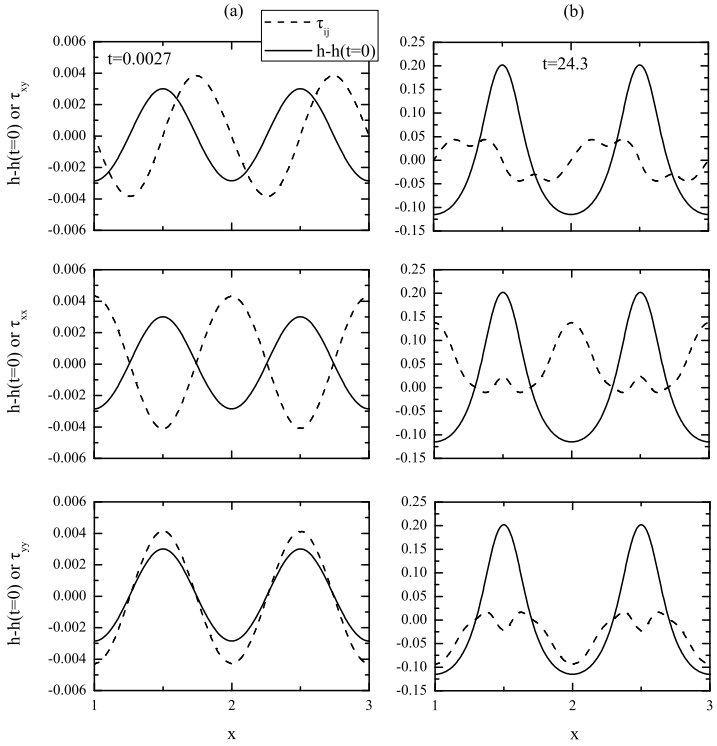


Figure 32: Interface height disturbance and profiles of $\tau_{p,xy}$, $\tau_{p,xx}$ and $\tau_{p,yy}$ along the interface at (a) $t = 0.0027$ (b) $t = 24.3$. The remaining parameters are the same as in Fig. 30.

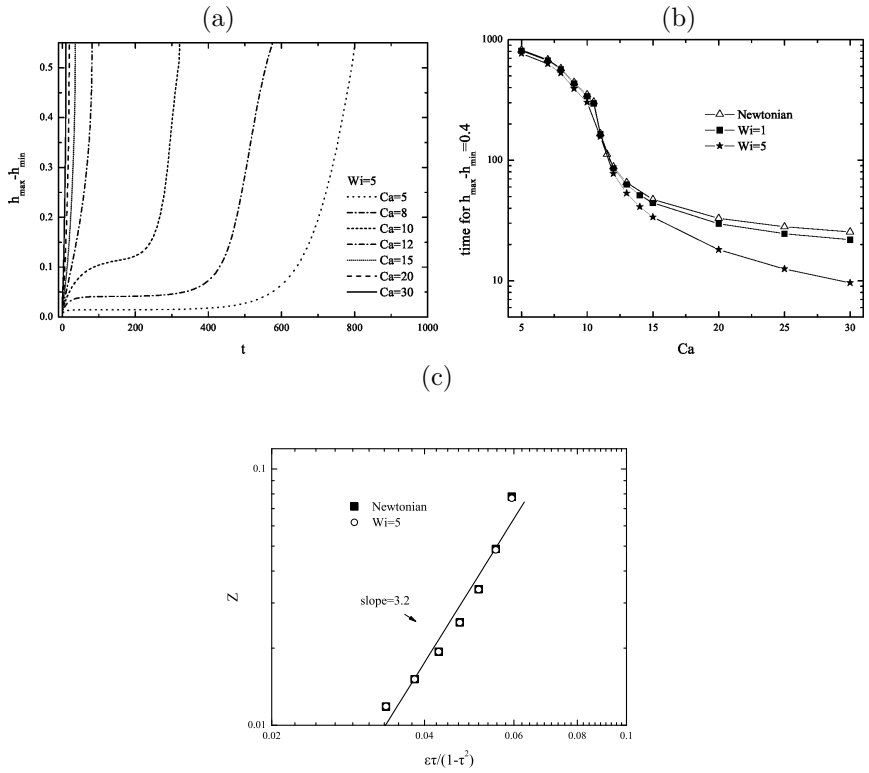


Figure 33: (a) Evolution of the amplitude for various Ca and for Wi = 5. (b) Time that is needed for $h_{max} - h_{min} = 0.4$ as a function of the Ca number for various Wi. (c) Dependence of the dimensionless amplitude $Z$ on $\epsilon\tau/(1-\tau^2)$. The remaining of the parameters are $\beta = 0$, $a_{PTT} = 0.05$, $\epsilon_1 = 2.5$, $\epsilon_2 = 1$, $d = 0.3$, $s = 0.8$, $p = 0.2$, $w = 0.2$, $L = 4$.

to Fig. 31c, and thus has a stabilizing role for highly deformed pillars.

It is noteworthy that according to Wu & Chou [66], who employ the lubrication approximation for analysis of the initial stages of deformation growth, the $xy$-component is the only one that survives in the linear limit and has a destabilizing effect. As it is shown in Fig. 32, this is actually true only at the very early stages of the flow. The magnitudes in Fig. 31c indicate that at finite growth normal stresses are dominant, being roughly two times larger than the $xy$ stress component. Thus, the usual assumption of reduced order models based on the lubrication approximation -according to which the normal stresses are negligible- is clearly not valid at the late stages of the flow.

In Fig. 33a we examine the effect of the capillary number, $Ca$, and present the evolution of the maximum amplitude of the interfacial perturbation for $Wi = 5$. Similarly to the case of a Newtonian fluid, for low $Ca$ numbers we find that the

amplitude initially grows and reaches a metastable state of a quasi-static low amplitude deformation, before eventually the pillars start growing again and reach the top electrode ; as in the case of Newtonian fluids, the amplitude is found to increase with $Ca$ (see Fig. 33c). We note that the power-law exponent of the dependence of the dimensioless amplitude $Z$ on $\epsilon\tau/(1-\tau^2)$ is not affected by the elasticity of the material. This indicates that the difference with the experimental value found in [53] should perhaps be attributed to the presence of free charge along the liquid-air interface which is not taken into account by our model. For higher values of the $Ca$ number, the amplitude continuously grows until the liquid reaches the protrusions.

In Fig. 33b, we evaluate the threshold in the $Ca$ number for the appearance of the metastable states for three different values of the $Wi$ number in a similar manner to Fig. 25b. We find that the time spent in the metastable state is not affected by the elasticity of the material and this is also reflected in the value of the 'critical' $Ca$ number which is $Ca \approx 10$ independent of the value of the $Wi$ number. On the other hand, we find that for high $Ca$ the time that is needed to achieve $h_{max} - h_{min} = 0.4$ decreases considerably with $Wi$; This characteristic growth time is further reduced with increase of $Ca$ as the role of surface tension becomes less significant. The above behavior is probably due to the effect of shear and elongational thinning which is attributed to the PTT fluid by the finite value of the parameter $a_{PTT}$. When the capillary number is well beyond its critical value, the growth rate of the disturbances is large, resulting in high rates of deformation. High deformation rates render the effect of shear and elongational thinning -which facilitate growth of the pillars- gradually more significant.

The effect of the $Ca$ number on the induced structures for the case of a viscoelastic fluid with $Wi = 1$ is presented in Fig. 34 where we plot the long-time profiles of the liquid-gas interface. Clearly, we find that decreasing the value of $Ca$ and as the critical $Ca$ for destabilization is approached the spatial periodicity of the structures is lost similarly to the case of a Newtonian fluid (see Fig. 27). Next, we keep the $Ca$ number constant and vary the value of $Wi$. In the case of the Newtonian fluid the interface exhibits a periodic structure with pillars of equal size. With increasing $Wi$ number a coarsening process takes place with the central pillars growing faster drawing fluid from their neighbours. It appears therefore that the bulk elasticity of the viscoelastic material has a similar effect to surface tension, which can also be interpreted as the elasticity of the interface, and does not affect only the growth rate but also the wavelength of the disturbances. However it should be noted that the effect of the bulk elasticity appears to be much weaker that the effect of surface tension. Our simulations indicate that the effect of elasticity becomes larger for $Ca$ numbers close to the 'critical' value whereas its effect decreases for high values of $Ca$.

As was noticed above, in order to produce well-ordered polymeric micro-structures over large distances it is important to know under which conditions it is possible to get periodic structures. To examine the effect of elasticity on the fabrication limits of this process we produced the map shown in Fig. 36. Here each point in the graph represents a simulation for the given value of

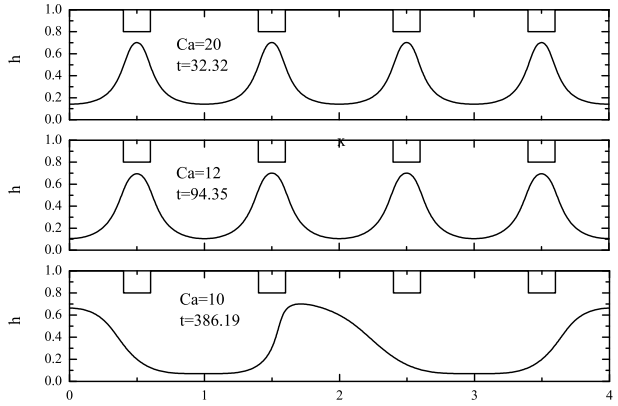


Figure 34: Long time profiles of the liquid-air interface for various Ca and for Wi = 1, $\beta = 0$, $a_{PTT} = 0.05$, $\epsilon_1 = 2.5$, $\epsilon_2 = 1$, $d = 0.3$, $s = 0.8$, $p = 0.2$, $w = 0.2$, $L = 4$.

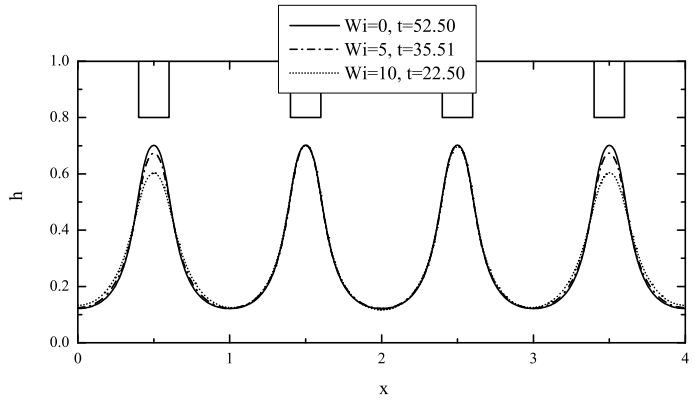


Figure 35: Long time profiles of the liquid-air interface for various Wi and for Ca = 15, $\beta = 0$, $a_{PTT} = 0.05$, $\epsilon_1 = 2.5$, $\epsilon_2 = 1$, $d = 0.3$, $s = 0.8$, $p = 0.2$, $w = 0.2$, $L = 4$.

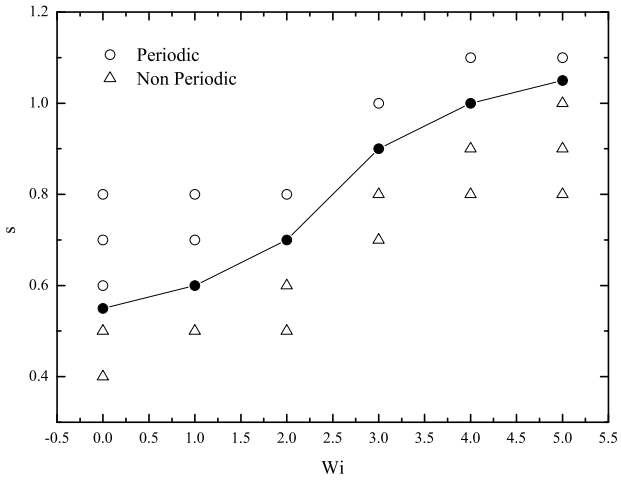


Figure 36: Flow map for Ca = 20, $\beta = 0$, $a_{PTT} = 0.05$, $\epsilon_1 = 2.5$, $\epsilon_2 = 1$, $d = 0.3$, $p = 0.2$, $w = 0.2$, $L = 4(s + w)$.

the distance between the protrusions, $s$, and the corresponding $Wi$ number. The open circles denote the case where we find solutions preserving the spatial periodicity whereas the triangles correspond to non-periodic solutions. The solid circles on the other hand denote near critical conditions; we used the same criterion for critical conditions as described in Fig. 29. From this figure we deduce that the spacing between the protrusions, $s$, that results in periodic structures increases significantly with $Wi$; this effect appears to saturate for high values of the $Wi$ number. The critical $s$ will impose a fabrication limit on the width of the channels that can be manufactured, and it appears from the above that the more elastic the material, the higher the minimum width of the channels that can be achieved.

At this point, we should note that early studies using linear theory for homogeneous electric fields were suggesting that viscoelasticity affects the growth rate but leaves unaffected the wavelength of the most dangerous mode. We find this to be true also for heterogeneous electric fields at early times when the amplitude of the disturbances is small. However, as the amplitude becomes larger and non-linear effects come into play this is no longer true for the case of heterogeneous electric fields. Viscoelasticity does affect the wavelength of the induced structures and needs to be taken into account for designing the process efficiently.

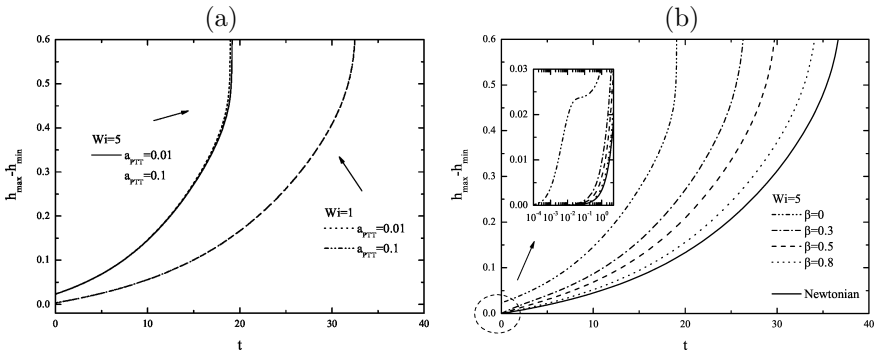


Figure 37: Evolution of the disturbance amplitude for (a) $\beta = 0$ and various $a_{PTT}$, (b) $a_{PTT} = 0.05$ and various $\beta$. The remaining parameters are Ca = 20, $\epsilon_1 = 2.5$, $\epsilon_2 = 1$, $d = 0.3$, $s = 0.8$, $p = 0.2$, $w = 0.2$, $L = 4$

### 3.3.3 Effect of rheological parameters $a_{PTT}$ and $\beta$ and dielectric constant, $\epsilon_1$

We continue our study by investigating the effect of the rheological parameters of the Phan-Thien Tanner model. Parameter $a_{PTT}$ controls the level of the elongational viscosity, and as it approaches zero the elongational viscosity increases to infinity. The influence of this parameter is more involved because it also affects the shear viscosity of the fluid. The predictions of the model for various values of this parameter can be found in [42]. To examine the effect of $a_{PTT}$, we have plotted in Fig. 37 the evolution of the amplitude of the maximum peak with time for two values of $Wi$ and for various values of $a_{PTT}$. For $Wi = 1$ the curves are found to be identical for all three values of $a_{PTT}$, which suggests that shear and elongational thinning do not have a significant effect in this case. On the other hand, for $Wi = 5$ the dynamics are slightly affected with regards to the time that exponential growth is initiated. Nevertheless, the long-time profiles are not affected significantly and remain almost identical for all values of $a_{PTT}$; not shown here for conciseness. This is a clear indication that shear and elongational thinning may affect to some extent the dynamics of the flow but do not have any significant effect on the induced structures and therefore do not have to be taken into account in the design process.

The ratio of the solvent viscosity to the total viscosity, $\beta$, is also an important parameter because it also influences the level of viscoelasticity in the momentum balance. The effect of $\beta$ is examined in Figs. 37b and 38. As it is shown, the solvent viscosity has a significant impact on the flow dynamics and for low values of $\beta$ leads to an acceleration of the pillar growth. However, increasing further $\beta$, the Newtonian contribution increases considerably with respect to the polymeric one and the behaviour of the film approaches the Newtonian limit. The inset in Fig. 37b depicts the early time dynamics where it is clearly shown that the growth rate for small disturbances depends monotonically on $\beta$

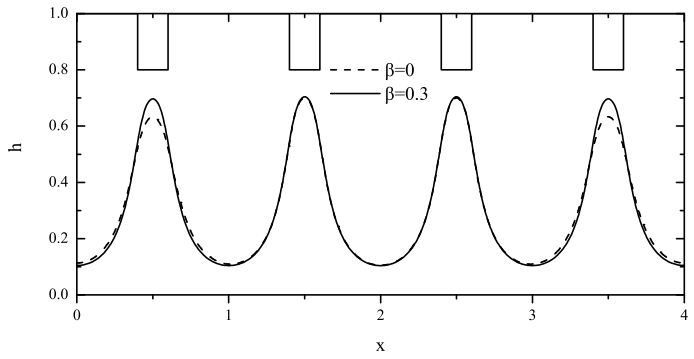


Figure 38: Long time profiles of the liquid-air interface for two different values of $\beta$ and for Wi = 5, Ca = 12, $a_{PTT} = 0.05$, $\epsilon_1 = 2.5$, $\epsilon_2 = 1$, $d = 0.3$, $s = 0.8$, $p = 0.2$, $w = 0.2$, $L = 4$.

in agreement with the results of linear theory presented in [67]. As it is shown in Fig. 38, for $\beta = 0$ and for the particular choice of the remaining parameters, the film deviates from the Newtonian case. The addition of some Newtonian contribution reduces the levels of elasticity in the fluid decreasing in turn the fabrication limit on the period of the protrusions of the top electrode.

Finally, the effect of the dielectric constant, $\epsilon_1$, is depicted in Fig. 39 where we have plotted the liquid-interface profiles at the time instant for each case that the height of the pillars becomes equal to 0.5. It is found that the pillars grow faster with increasing $\epsilon_1$ due to the higher intensity of the electric field that the liquid experiences. Regarding the shape of the formed pillars we find that with increasing $\epsilon_1$ the pillars become thinner at the peaks and flatter at the troughs; the pillars acquire a quasi triangular shape for the highest value of $\epsilon_1 = 5$.

### 3.3.4 AC electric field

We continue our study with an investigation of the effect of an AC electric field on the flow dynamics. The effect of AC field is introduced into our model by imposing the following boundary condition at the top electrode

$$\phi_2(t) = 1 + AC\,[\cos(\omega t) - 1] \tag{191}$$

where $AC$ and $\omega$ are the amplitude and oscillation frequency of the electric field, respectively. In Figure 40 we examine the effect of the oscillation amplitude, $AC$ on the evolution of the height of the columns of the viscoelastic layer. For zero value of $AC$ the electric field is DC and we observe a monotonic increase of the

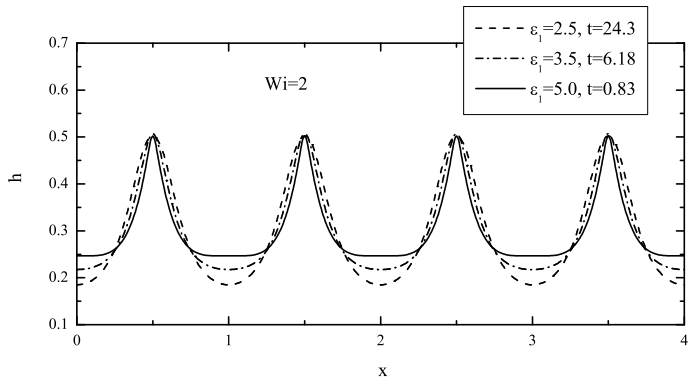


Figure 39: Profiles of the liquid-air interface for three different values of $\epsilon_1$ and for Wi = 2, Ca = 20, $a_{PTT} = 0.05$, $\beta = 0$, $\epsilon_2 = 1$, $d = 0.3$, $s = 0.8$, $p = 0.2$, $w = 0.2$, $L = 4$.

columnar height. For finite values of the electric field oscillation amplitude, $AC$, though we find that the liquid-air interface oscillates following the oscillation of the electric field. Increasing the value of $AC$ the oscillation amplitude of the interfacial disturbances increases as well resulting in turn in the increase of the number of cycles and the overall time that is needed for the columns to reach the top electrode.

Recently, Espin et al [68] performed a linear stability analysis for a similar system, using the Jeffreys viscoelastic model and have shown that besides the effect on the growth rate, the presence of an AC field may also affect the disturbance wavelength of the viscoelastic film. In order to investigate this effect in the non-linear regime we prepared fig. 41 where we depict the shape of the liquid-air interface at large times for two different values of the parameter $AC$ which correspond to the case of a DC ($AC = 0$) and an AC ($AC = 0.1$) electric field. Interestingly, we find that in the case of the AC field the liquid-air interface follows more closely the structure of the top electrode suggesting that it is possible to decrease the fabrication limit of this process by using AC instead of DC electric fields.

## 3.4 Conclusions

We carried out a numerical investigation of the flow of both a Newtonian and a viscoelastic film under the action of an heterogeneous electric field imposed by the presence of a patterned electrode. The mixed finite element method was used combined with a quasi-elliptic mesh generation scheme, which allows an accurate description of the large deformations of the liquid-air interface. The viscoelastic behaviour of the polymeric film was modelled using the PTT

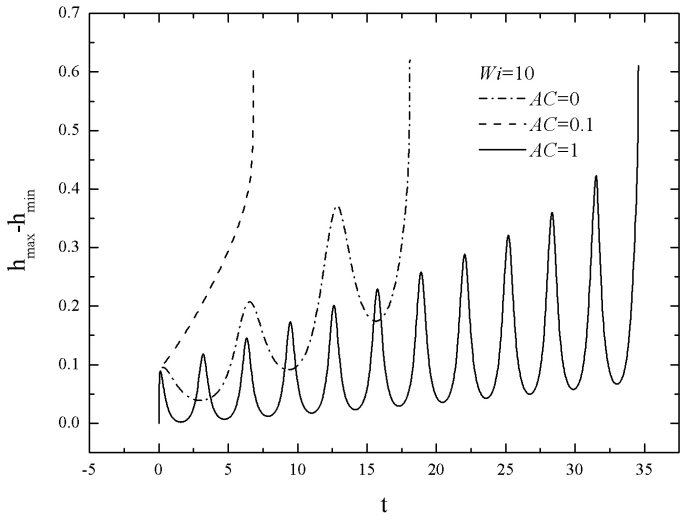


Figure 40: Evolution of the interfacial height disturbance amplitude for various amplitudes of the AC electric field for Ca = 20, $Wi = 10$ and $\omega = 1$. The remaining parameters are $a_{PTT} = 0.05$, $\beta = 0$, $\epsilon_1 = 2.5$, $\epsilon_2 = 1$, $d = 0.3$, $s = 0.8$, $p = 0.2$, $w = 0.2$, $L = 4$.

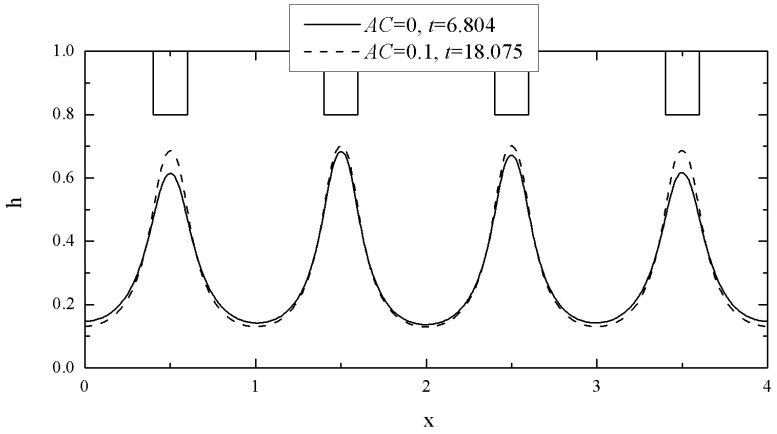


Figure 41: Profiles of the liquid-air interface for two different values of the amplitude of the AC field and for Ca = 20, $Wi = 10$ and $\omega = 1$. The remaining parameters are $a_{PTT} = 0.05$, $\beta = 0$, $\epsilon_1 = 2.5$, $\epsilon_2 = 1$, $d = 0.3$, $s = 0.8$, $p = 0.2$, $w = 0.2$, $L = 4$.

constitutive law. Simulations up to high Weissenberg numbers were successful by using the EVSS-G/SUPG formulation for the numerical discretization and weighting of the constitutive equations. Attention was focused on the non-linear dynamics of the flow, and it was interrogated in particular how the dynamics is influenced by the rheological characteristics of the material and how in turn it affects the fabrication limits of this process.

We have shown that for low values of the $Ca$ number a metastable state of finite amplitude interfacial deformation arises before eventually the perturbations grow until they reach the top electrode; during the late stages of the flow a coarsening process also takes place. Our non-linear simulations provide a better agreement with experimental observations for the amplitude of the pseudo-steady state in comparison to the earlier predictions of linear theory [53]. We have shown that under the influence of a patterned electrode the effect of elasticity is more involved than what is suggested by linear theory for the case of an homogeneous electric field. We find that shear polymeric stresses are destabilizing at early times, as predicted by linear theory, but become stabilizing at later stages of the flow. Normal stresses, on the other hand, become increasingly important as the liquid-air interface deforms, destabilizing the film. It is shown that at late times normal stresses become dominant and cannot be ignored, as it is usually done under the lubrication approximation, for the accurate prediction of the flow dynamics. We also find that the fabrication limit on the period of the electrode protrusions appears to depend on the elasticity

of the material, contrary to the predictions of linear theory of a constant most dangerous wavelength in the case of a flat electrode (homogeneous electric field). Finally, the amplitude of the pseudo-steady interfacial deformations appears to be unaffected by the elasticity of the material and the same is also true for the critical voltage below which these metastable states arise.

## 3.5 Appendix: Finite element formulation

The physical domain was discretized using triangular elements. We approximate the velocity vector, the position vector and the potential with six-node Lagrangian basis functions, $\psi^j$, and the pressure, the elastic stresses, as well as the velocity gradients with three-node Lagrangian basis functions, $\chi^j$.

For the momentum, mass balances and the Laplace equation for the potential, we employ the finite element/Galerkin method, which after applying the divergence theorem results in the following weak forms:

$$\int_V \left[ D_i \mathrm{Re} \left( \frac{\partial \mathbf{v}_i}{\partial t} + \mathbf{v}_i \cdot \nabla \mathbf{v}_i \right) \psi^j - P \nabla \psi^j + \nabla \psi^j \cdot \Sigma + 2 \nabla \psi^j \cdot \gamma_i + \mathrm{St} \psi^j \mathbf{e}_z \right] dV - \int_S \left[ \mathbf{n} \cdot T_i \right] \psi^j dS = 0, \quad (192)$$

$$\int_V \left[ \nabla \cdot \mathbf{v}_i \right] \chi^j dV = 0, \quad (193)$$

$$\int_V \left[ \epsilon_i \nabla \phi_i \cdot \nabla \psi^j \right] dV - \int_S \left[ \mathbf{n} \cdot \nabla \phi_i \right] \psi^j dS = 0. \quad (194)$$

where $dV$ and $dS$ are the differential volume and surface area, respectively. The surface integral that appears in the momentum equation is split into as many parts as the number of boundaries of the physical domain and the relevant boundary condition is applied therein.

The weak form of the mesh generation equations is derived similarly by applying the divergence theorem:

$$\int_V \left[ \alpha \cdot \nabla \eta \right] \cdot \nabla \psi^j dV = 0, \quad (195)$$

$$\int_V \left[ \left( \delta \sqrt{\frac{x_\xi^2 + y_\xi^2}{x_\eta^2 + y_\eta^2}} + (1 - \delta) \right) \nabla \xi \right] \cdot \nabla \psi^j dV = 0. \quad (196)$$

The continuous approximation for the components of the velocity gradient tensor is written as

$$\int_V \left[ G - \nabla \mathbf{v}_1 \right] \chi^j dV = 0. \quad (197)$$

The constitutive equation due to its hyperbolic character is discretized using the streamline upwind Petrov-Galerkin (SUPG) method proposed by [90]

$$\int_V \Big[ Y(\tau_{p,1})\Sigma + \mathrm{Wi}\hat{\Sigma} + 2\mathrm{Wi}(1-\beta)M_1\hat{\Pi} \\ -2(1-\beta)(1-Y(\tau_{p,1}))M_1\Pi \Big]\omega^j dV = 0, \quad (198)$$

where $\Pi = 1/2(G+G^T)$ and the definition of the Gordon-Schowalter derivative is given by

$$\hat{X} = \frac{\partial X}{\partial t} + \mathbf{v}_1 \cdot \nabla X - (\nabla \mathbf{v}_1 - \xi_s \Pi)^T \cdot X - X \cdot (\nabla \mathbf{v}_1 - \xi_s \Pi). \quad (199)$$

The weighting function $\omega^j$ is formed from the finite element basis function for the elastic stress components according to

$$\omega^j = \chi^j + \frac{h}{|\mathbf{v}_1|}\nabla\chi^j, \quad (200)$$

where $|\mathbf{v}_1|$ is the mean velocity and $h$ is a characteristic length in each element. The mean velocity $|\mathbf{v}_1|$ in an element is defined as the mean value of the velocity at the vertices of the corresponding element. As a characteristic length, $h$, we used the square root of the area of each triangular element.

# 4 Non-linear dynamics of electric field instabilities in liquid trilayers

## 4.1 Indroduction

The interaction of an externally applied electric field with a liquid can give rise to interfacial instabilities. Such instabilities can be exploited to provide a simple and versatile method for the fabrication of well-ordered polymer structures at the microscale and nanoscale with many technological applications. Naturally, this problem has attracted the interest of many experimental and theoretical studies; much of this research is summarized by Wu & Russel [91].

The electrically induced flow of single liquid films have been studied extensively [46, 47, 48, 49, 51, 50, 52, 54, 53, 74, 75] and is now well understood. It has been shown, though, that it is possible to produce more complex structures when applying the electrohydrodynamic process to polymer bilayers with an air gap between the bilayer and the mask. Morariu *et al.* [50] performed experiments on a polymer/polymer/air (PMMA/PS/air) trilayer and showed that the primary structures arise at the PS/air interface which destabilizes much faster than the PMMA/PS interface; the dynamics of the latter interface are affected significantly by the presence of highly viscous materials on both sides of the interface. In these experiments the intermediate layer deforms and pillars are formed while later the bottom layer encapsulates those pillars forming core-shell

structures [50, 92]. On the other hand, as was shown by Leach *et al.* [93] it is also possible to produce closed-cell structures when the electric effects are combined with dewetting forces.

From a theoretical point of view, Bandyopadhyay et al. [59] made the first attempt to investigate the stability of a viscous bilayer under air. Their work was followed by a more general paper by Bandyopadhyay et al. [60] who performed a linear stability analysis along with time-dependent simulations using the lubrication approximation. In the case of viscous bilayers, it was shown that two different modes of interfacial evolution are possible: (a) in phase bending and (b) antiphase squeezing; the mode type can be switched by tuning the dielectric properties of the films. The case of elastic solid bilayers has also been examined [60, 94]. The influence of topography of the electrode patterns was investigated by Reddy *et al.* [61] who also examined the conditions for the formation of ordered core-shell structures by performing 2D and 3D transient simulations using the lubrication approximation. The same authors extended their work by considering the general case of a trilayer substituting the top layer of air with another liquid [63]. Their results suggest that variation in the kinetics parameters such as the ratio of the viscosities of the films can also affect the modes of evolution and morphologies at the interfaces. Roberts & Kumar [62] employed the leaky dielectric model to investigate the effect of interfacial charge accumulation and AC electric fields on the dynamics and stability of the system through a linear stability analysis. It was shown that AC fields can be used to control the location of free charge drastically affecting system stability and enabling the creation of smaller pillars than possible with DC electric fields.

The majority of the aforementioned works has focused on the flow of Newtonian fluids which is now well understood. In the case of single film systems, the first attempt to take into account the complex rheology of a polymeric liquid, which are often used in this process, was made by Wu & Chou [66]. These authors performed a linear stability analysis for initially static thin polymeric films underneath a flat electrode and considered the case of a Maxwell liquid. Their results suggested that the polymer elasticity destabilizes the system and that for large enough Deborah number, a resonant phenomenon appears as a result of the interaction between the two destabilizing mechanisms (the electrostatic force and the polymer elasticity). Tomar *et al.* [67], though, recognised that the presence of even a small amount of inertia removes the singularity and leads to finite but large growth rates for all values of Deborah number. Moreover, it was found that in the linear regime the wavelength of the fastest growing mode (i.e. the dominant lengthscale of the instability) is independent of the rheological properties such as relaxation time and solvent viscosity. Their findings were confirmed by Espin *et al.* [68] using an asymptotic expansion. The latter authors also examined the viscoelastic effects under the influence of AC fields and noticed that the impact is largest when the relaxation time and oscillation time scale are comparable. In the case of AC fields, it is shown that the wavelength is also affected contrary to the predictions of linear theory for the case of DC fields [67]. Very recently, Karapetsas & Bontozoglou [95] examined the non-linear dynamics of a viscoelastic material under the influence of a spatially

periodic electric field. They performed two-dimensional transient numerical simulations and their results suggest that the effect of elasticity is more involved than what is suggested by linear theory for the case of an homogeneous electric field. Elasticity is destabilizing at early times, as predicted by linear theory, but actually retards the flow at later stages as the liquid-air interface deforms. Moreover, in the case of spatially periodic electric field, elasticity appears to affect both the critical voltage for instability and the fabrication limit on the period of the top electrode protrusions.

As noted above, most of the previous studies on bilayers considered either purely viscous or purely elastic films. An exception to this is the work of Bandyopadhyay *et al.* [69] who considered viscoelastic bilayers composed either of Maxwell fluids or soft elastic solids obeying the Kelvin-Voigt model. These authors performed a linear stability analysis and found that in the case of viscoelastic liquid (Maxwell fluid) the length and time scale was shown to depend significantly on the relaxation time of the films even in the case of flat electrodes, in contrast to the single film systems. These results indicate that in the case of bilayers the effect of the rheological characteristics on the evolution of two coupled interfaces is more involved than a purely kinetic role.

The scope of this work is to investigate the effect of viscoelasticity on the non-linear dynamics of a polymeric bilayer under the influence of an electric field. We avoid to make any assumptions, such as using lubrication theory, in order to describe the flow dynamics as accurately as possible; as was shown by [95] lubrication approximation is not valid at late stages of the flow. We perform two-dimensional transient numerical simulations, using the finite element method combined with an elliptic grid generation scheme for the determination of the unknown position of the interface. The viscoelasticity of the polymeric bilayer is taken into account using the affine Phan-Thien Tanner model. We investigate the effects of the various rheological parameters on the dominant wavelength and non-linear dynamics of the two interfaces.

The remainder of this chapter is organized as follows. In Section 4.2, we describe the system of governing equations and outline the numerical method used for its numerical solution. The results are presented and discussed in Section 4.3. Finally, the concluding remarks are given in Section 4.4.

## 4.2 Problem formulation

We consider the dynamics of three perfect dielectric fluids sandwiched between two rigid, flat and impermeable electrodes (see Fig. 42). The bilayer consists of two immiscible polymeric viscoealstic liquids and is considered to be surrounded by a Newtonian liquid. All fluids, which are initially stationary, are taken to be incompressible with the lower ('1'), middle ('2') and upper fluid ('3') having density $\rho_i$ and dielectric constants $\epsilon_i$, $(i = 1 - 3)$; these properties are assumed to be constant. The viscosity of the upper fluid is also constant and denoted by $\mu_3$. The viscoelastic liquids of the bilayer (fluids '1' and '2') have a zero shear viscosity $\mu_i = \mu_{s,i} + \mu_{p,i}$ where $\mu_{s,i}$ and $\mu_{p,i}$ are the viscosities of the solvent and the polymer, respectively, and relaxation time $\lambda_i$, $(i = 1, 2)$. The surface tension

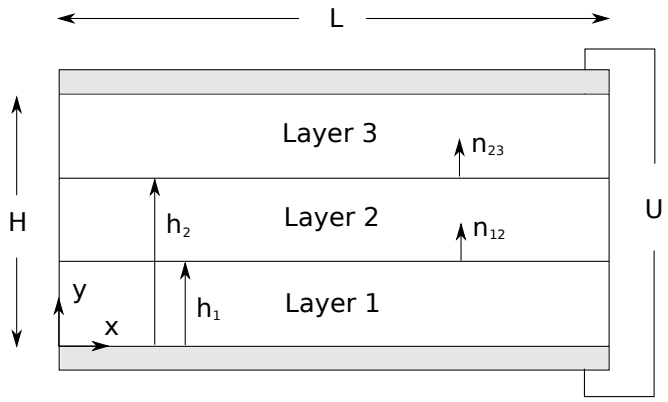


Figure 42: Schematic of the flow geometry

of the liquid-liquid interface ('12'), $\sigma_{12}$, and the liquid-air interface ('23'), $\sigma_{23}$, are assumed to be constant. The top and bottom electrodes are maintained at constant potentials $\phi_2(y = H) = U$ and $\phi_1(y = 0) = 0$, respectively.

We scale all lengths with the distance between the top and bottom electrodes, $H$, velocities with $V^* = \epsilon_o U^2/(\mu_1 H)$, pressure and stresses with $\mu_1 V^*/H$ and electric potential with the potential difference $U$. Substituting this scaling into the governing equations and boundary conditions, the following dimensionless groups emerge

$$\begin{gathered} \mathrm{Re} = \frac{\rho_1 V^* H}{\mu_1},\ \mathrm{St} = \frac{\rho_1 g H^2}{\mu_1 V^*},\ \mathrm{Wi}_i = \frac{\lambda_i V^*}{H},\ \mathrm{Ca}_i = \frac{\mu_1 V^*}{\sigma_i} \\ \mathrm{D}_i = \frac{\rho_i}{\rho_1},\ M_i = \frac{\mu_i}{\mu_1},\ \beta_i = \frac{\mu_{s,i}}{\mu_1} \end{gathered} \tag{201}$$

Inserting the previously defined characteristic quantities into the momentum and mass conservation equations, we obtain:

$$D_i \mathrm{Re}\left(\frac{\partial \mathbf{v}_i}{\partial t} + \mathbf{v}_i \cdot \nabla \mathbf{v}_i\right) - \nabla \cdot T_i + \mathrm{St}\mathbf{e}_z = 0, \tag{202}$$

$$\nabla \cdot \mathbf{v}_i = 0, \tag{203}$$

where $\nabla$ denotes the gradient operator, subscript $i$ indicates the corresponding fluid, $\mathbf{v}_i$ is the velocity vector and $T_i$ is the total stress tensor given by

$$T_i = -P_i I + \tau_i + m_i. \tag{204}$$

Here $P_i$ denotes the pressure, $I$ is the identity tensor and $\tau_i$ the extra stress tensor

$$\tau_i = \tau_{p,i} + 2\beta_i M_i \gamma_i,\ (i = 1, 2) \tag{205}$$

$$\tau_3 = 2M_3\gamma_3. \tag{206}$$

Note that for the viscoelastic materials the extra stress tensor is split into a purely viscous part, $2\beta M_i\gamma_i$, and a polymeric contribution, $\tau_{p,i}$. $\gamma_i$ denotes the rate of strain tensor

$$\gamma_i = \frac{1}{2}\left(\nabla \mathbf{v}_i + \nabla \mathbf{v}_i^T\right). \tag{207}$$

The Maxwell stress tensor, denoted by $m_i$, describes the interaction of fluid $i$ with the electric field, $\mathbf{E}_i$, and is defined as

$$m_i = \epsilon_i \mathbf{E}_i \mathbf{E}_i - \frac{1}{2}\epsilon_i \mathbf{E}_i \cdot \mathbf{E}_i I. \tag{208}$$

Note that due to the absence of free charge from the bulk of the fluid and since $\epsilon_i$, $(i = 1 - 3)$ are spatially independent, $\nabla \cdot m_i = 0$. Therefore it becomes evident that Maxwell stresses will do not have any contribution in eq. (202) but will nevertheless enter the problem through the interfacial boundary conditions. The Maxwell stresses depend on the local intensity of the electric field. Under the electrostatic approximation and for an electrically neutral fluid, Maxwell's equations reduce to the following set of equations

$$\nabla \cdot (\epsilon_i \mathbf{E}_i) = 0, \tag{209}$$

$$\nabla \times \mathbf{E}_i = 0. \tag{210}$$

Since the electrical field is irrotational, we can define a potential function $\phi_i$ such that

$$\mathbf{E}_i = -\nabla \phi_i. \tag{211}$$

By combining eq. (209) and eq. (211) we get the following equation

$$\nabla \cdot (\epsilon_i \nabla \phi_i) = 0. \tag{212}$$

To complete the description, a constitutive equation that describes the rheology of the viscoelastic material is required in order to determine the polymeric part of the extra stress tensor. As such, we use the following differential model that has been proposed by [76]

$$Y(\tau_{p,i})\tau_{p,i} + \mathrm{Wi}_i \hat{\tau}_{p,i} = 2(1-\beta_i)M_i\gamma_i, \ (i = 1, 2). \tag{213}$$

The symbol $\hat{}$ over the viscoelastic stress denotes the Gordon-Schowalter derivative defined as

$$\hat{X} = \frac{\partial X}{\partial t} + \mathbf{v}_i \cdot \nabla X - (\nabla \mathbf{v}_1 - \xi_{s,i}\gamma_i)^T \cdot X - X \cdot (\nabla \mathbf{v}_i - \xi_{s_i}\gamma_i), \ (i = 1, 2), \tag{214}$$

where $X$ is any second order tensor. In the present study we have used the exponential form of the PTT model [77]

$$Y(\tau_{p,i}) = \exp\left[\frac{a_{PTT,i}\mathrm{Wi}_i}{(1-\beta)M_i} tr(\tau_{p,i})\right], \ (i = 1, 2). \tag{215}$$

This model has two parameters, $\xi_{s,i}$ and $a_{PTT,i}$. The first one is related to the non-affine motion of the polymer chains with respect to the macroscopic motion of the continuum. By setting $\xi_{s,i}$ equal to zero no such motion or slip is allowed; for the rest of the paper $\xi_{s,i}$ will be considered to be zero. The Gordon-Schowalter derivative reduces to the upper convective one and the fluid model is referred to as the affine PTT model. The second parameter, $a_{PTT,i}$, imposes an upper limit to the elongational viscosity, which increases as this parameter decreases, while it introduces elongational thinning. Moreover $a_{PTT,i}$ is related to the shear-thinning behavior of the model. The predictions for the elongational and shear viscosity of this model for various values of $a_{PTT,i}$ appear in Fig. 9 of [42]. By setting both $a_{PTT,i} = 0$ and $\xi_{s,i} = 0$, the PTT model reduces to the Oldroyd-B model. Retaining the zero values for $a_{PTT,i}$ and $\xi_{s,i}$ and additionally setting $\beta_i = 0$, the PTT model reduces to the UCM model.

In order to solve accurately and efficiently the flow inside the viscoelastic material we employ the elastic viscous split stress EVSS-G formulation [78, 79]. This method consists of splitting the polymeric part of the extra stress tensor into a purely elastic and a viscous part

$$\tau_{p,i} = \Sigma_i + 2(1 - \beta_i)M_i\gamma_i. \tag{216}$$

Moreover, an independent interpolation of the components of the velocity gradient tensor is introduced

$$G_i = \nabla \mathbf{v}_i. \tag{217}$$

The former splitting ensures the elliptic nature of the momentum equations even in the absence of a solvent ($\beta = 0$), while the latter substitution makes the approximations in the constitutive equation of the elastic stress and the velocity gradient compatible to each other. This scheme has been used with success in the past [42, 80, 81] permitting the calculations up to very high Weissenberg numbers.

### 4.2.1 Boundary conditions

Solution of the above set of equations is determined subject to the following boundary conditions.

On the solid walls we apply the usual no-slip and no-penetration boundary conditions while on the two edges of the physical domain ($x = 0, L$) we apply periodic conditions.

Along the liquid-liquid ($y = h_1$) and the the liquid-air ($y = h_2$) interfaces the velocity is continuous

$$\mathbf{v}_1 = \mathbf{v}_2 \text{ at } y = h_1, \tag{218}$$

$$\mathbf{v}_2 = \mathbf{v}_3 \text{ at } y = h_2, \tag{219}$$

and the flow field satisfies the local interfacial force balance between the stresses

$$\mathbf{n}_{12} \cdot T_1 = \mathbf{n}_{12} \cdot T_2 + \frac{2\mathcal{H}_{12}\mathbf{n}_{12}}{\mathrm{Ca}_{12}} \text{ at } y = h_1 \tag{220}$$

$$\mathbf{n}_{23} \cdot T_2 = \mathbf{n}_{23} \cdot T_3 + \frac{2\mathcal{H}_{23}\mathbf{n}_{23}}{\mathrm{Ca}_{23}} \text{ at } y = h_2 \tag{221}$$

where $\mathbf{n}_{12}$ and $\mathbf{n}_{23}$ denote the unit normal pointing towards the middle and upper liquid, respectively, and $2\mathcal{H}_i$ is the mean curvature of the corresponding interface

$$2\mathcal{H}_i = -\nabla_{s,i} \cdot \mathbf{n}_i, \; i = 12, 23, \tag{222}$$

and $\nabla_{s,i}$ is the surface gradient operator, defined as

$$\nabla_{s,i} = (I - \mathbf{n}_i\mathbf{n}_i)\,\nabla, \; i = 12, 23. \tag{223}$$

In addition, along the moving interface we impose the kinematic boundary condition,

$$\frac{\partial f_i}{\partial t} + \mathbf{v}_2 \cdot \nabla f_i = 0, \; i = 12, 23, \tag{224}$$

where $f_i$ describes the position of corresponding the interface. A balance of the normal and tangential component of the electric field gives the continuity of the potentials and the electric displacement across both interfaces

$$\phi_1 = \phi_2, \; \mathbf{n}_{12} \cdot (\epsilon_1 \nabla\phi_1) = \mathbf{n}_{12} \cdot (\epsilon_2 \nabla\phi_2) \text{ at } y = h_1, \tag{225}$$

$$\phi_2 = \phi_3, \; \mathbf{n}_{23} \cdot (\epsilon_2 \nabla\phi_2) = \mathbf{n}_{23} \cdot (\epsilon_3 \nabla\phi_3) \text{ at } y = h_2, \tag{226}$$

Finally to complete our model we have to set a datum pressure and as such, we impose a zero value to the pressure at a node of the top electrode, $P(x = 0, y = 1) = 0$.

### 4.2.2 Elliptic grid generation

The above set of equations is combined with an elliptic grid generation scheme capable of following the deformations of the physical domain. This method has been successfully applied in flows that exhibit large deformations in steady state [80] and transient calculations [82, 83, 84, 95]. The grid generation scheme consists of a system of quasi-elliptic partial differential equations, capable of generating a boundary fitted discretization of the deforming domain occupied by the liquid. With this scheme the physical domain $(x, y)$ is mapped onto a computational one $(\eta, \xi)$. A fixed computational mesh is generated in the latter domain while, through the mapping, the corresponding mesh in the physical domain follows its deformations. The mapping is based on the solution of the following system of quasi-elliptic partial differential equations

$$\nabla \cdot (\alpha \cdot \nabla\eta) = 0 \tag{227}$$

$$\nabla \cdot \left[ \left( \delta \sqrt{\frac{x_\xi^2 + y_\xi^2}{x_\eta^2 + y_\eta^2}} + (1 - \delta) \right) \nabla\xi \right] = 0 \tag{228}$$

where

$$\alpha = \begin{pmatrix} 1 & 0 \\ 0 & a \end{pmatrix}, \; a \geq 1. \tag{229}$$

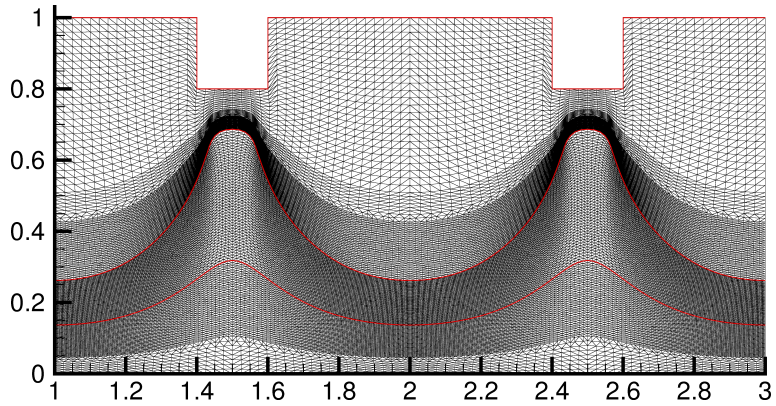


Figure 43: (Color online) Typical grid with 2 levels of local refinement adjacent to the liquid-liquid and liquid-air interfaces for $\mathrm{Wi}_1 = Wi_2 = 0$, $\mathrm{Ca}_1 = 10$, $\mathrm{Ca}_2 = 20$, $d_1 = d_2 = 0.2$, $s = 0.8$, $p = 0.2$, $w = 0.2$ at time $t = 11.83$.

The subscripts denote differentiation with respect to the indicated variable. The parameter $a$ forces the $\xi$-coordinate lines to be equidistant in the $y$-direction and $\delta$ is a parameter that controls the smoothness of the mapping relative to the degree of orthogonality of the mesh lines. These parameters are adjusted by trial and error; here we set $a = 100$ and $\delta = 0.1$. For a more detailed description of this method the interested reader may refer to [85, 86, 87].

In order to solve the above system of differential equations, appropriate boundary conditions must be imposed. On the fixed boundaries, we impose the equations that define their position, and the remaining degrees of freedom are used for optimally distributing the nodes along these boundaries. Along the moving interfaces we simply impose the corresponding kinematic equation. We should note here that special care was taken for the mesh near the interface. In order to resolve adequately the flow, a more refined mesh around this region is needed. To this end, we have introduced a local refinement scheme using the h-method [88]. In order to illustrate the quality of the resulting mesh produced following our method we present in Fig. 43 a typical grid; here we show for clarity the domain $0.8 < x < 2.4$.

In order to solve numerically the governing equations along with the elliptic grid equations, we used the mixed finite element method and detailed information about the weak formulation of all the equations is given in the 4.5.

## 4.3 Results

Figure 44 shows a 2D non-linear simulation of a liquid bilayer under air in the case of flat electrodes. The instability starts as a bending mode of the interfaces with a larger deformation at the liquid-air interface. As the evolution progresses, the liquid-air interface develops into columnar structures. At the late evolution stages, the lower layer also grows stronger toward the top electrode

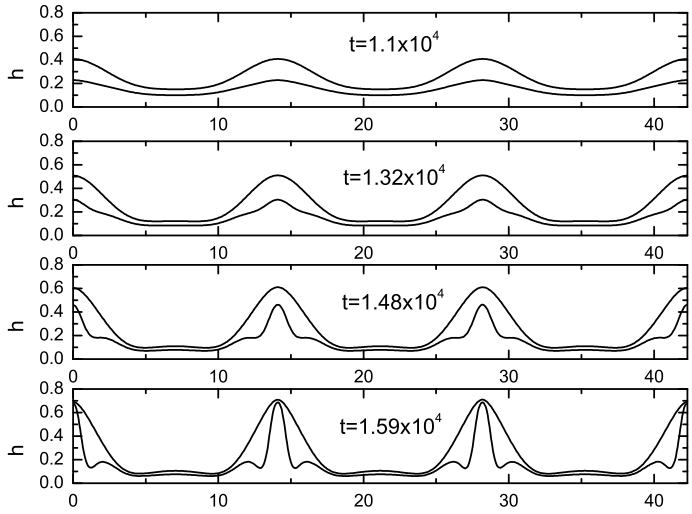


Figure 44: Evolution of the shapes of the liquid-air and liquid-liquid interfaces with time for $\mathrm{Wi}_1 = 0$, $\mathrm{Wi}_2 = 10$, $\mathrm{Ca}_1 = 0.74$, $\mathrm{Ca}_2 = 31.6$, $a_{PTT} = 0.05$, $\beta = 0$, $\epsilon_1 = 3$, $\epsilon_2 = 2$, $\epsilon_3 = 1$, $d_1 = 0.15$, $d_2 = 0.1$, $L = 42.3$.

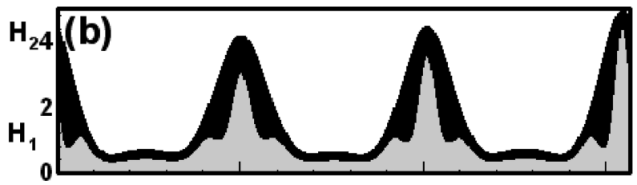


Figure 45: Long time shapes of the liquid-air and liquid-liquid interfaces with time for Newtonian liquids taken from Bandyopadhyay et al. [60]. The remaining paarmeters are the same with Fig. 44

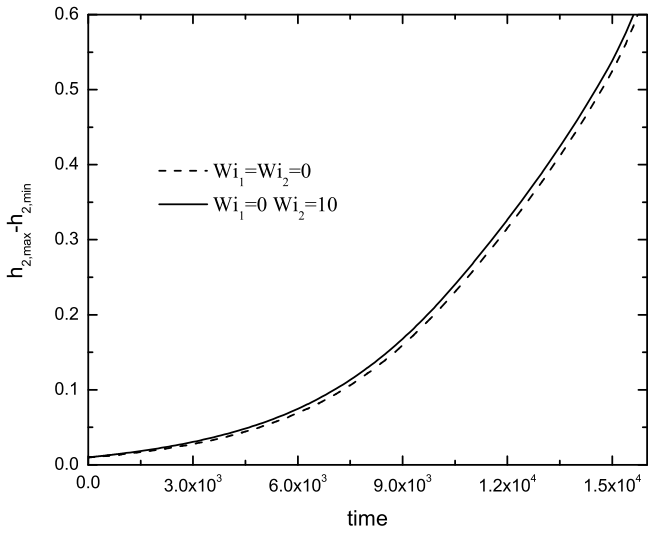


Figure 46: Evolution of the disturbance amplitude of the liquid-air interface for (a) $\mathrm{Wi}_1 = \mathrm{Wi}_2 = 0$ and (b) $\mathrm{Wi}_1 = 0$, $\mathrm{Wi}_2 = 10$. The remaining parameters are $\mathrm{Ca}_1 = 0.74$, $\mathrm{Ca}_2 = 31.6$, $a_{PTT} = 0.05$, $\beta = 0$, $\epsilon_1 = 3$, $\epsilon_2 = 2$, $\epsilon_3 = 1$, $d_1 = 0.15$, $d_2 = 0.1$, $L = 42.3$.

and, consequently, forms columnar structures. The final morphology shows an array of concentric columnar structures with a lower layer core and an outer-shell composed of the upper layer liquid. These findings are in accordance with the results of Bandyopadhyay et al. [60] who employed the lubrication approximation and examined the case of a viscous bilayer (see Fig. 45 for a case of a viscous bilayer). We note that the differences in the resulting morphology of the columns between the case of a viscous bilayer and the viscoelastic bilayer are very small indicating that the effect of elasticity is rather small in the case of a homogeneous electric field. This is also reflected on the overall time that is needed for the columns to grow which is not affected significantly with the elasticity of the middle layer (see Fig. 46).

We continue our study with by focusing on the more interesting case of patterned electrodes. In this case and assuming that both liquids that form the bilayer are Newtonian ($Wi_1 = Wi_2 = 0$) the presence of a heterogeneous electric field destabilizes the interfaces sooner and the process takes significantly less time. In Fig. 47 we present contour plots for the velocity field, pressure and electric potential at $t = 12.03$; for clarity we present here only part of our computational domain ($1 \leq x \leq 3$). Both liquid films are initially flat and quiescent. Upon the application of voltage the liquid experiences non-uniform

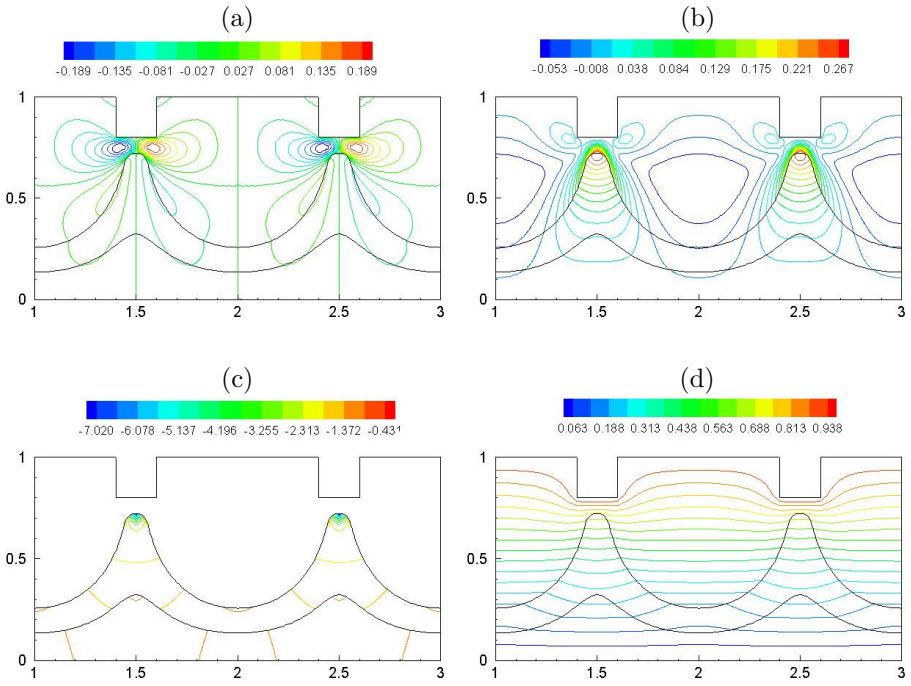


Figure 47: (Color online) Contour plots of (a) $v_x$, (b) $v_y$, (c) $P$ and (d) electric potential at $t = 12.03$ for $\mathrm{Wi}_1 = \mathrm{Wi}_2 = 0$. The remaining parameters are $\mathrm{Ca}_1 = \mathrm{Ca}_2 = 20$, $a_{PTT} = 0.05$, $\beta = 0$, $\epsilon_1 = 2$, $\epsilon_2 = 3$, $\epsilon_3 = 1$, $d_1 = 0.2$, $d_2 = 0.2$, $s = 0.8$, $p = 0.2$, $w = 0.2$, $L = 4$.

electrostatic forces, due to the spatial heterogeneity of the electric field that is created by the top electrode, and liquid is drawn towards the protrusions, destabilizing the liquid-liquid and liquid-air interfaces. The flow field appears to be symmetric around the protrusions giving rise to symmetric structures that follow closely the geometrical characteristics of the top electrode. The pressure varies mainly inside the liquid phases (see Fig. 47c) whereas in the gas phase (top layer) it remains almost constant (approximately equal to the datum pressure) due to the fact that the viscosity of the gas is very small. The contour lines of the electric potential are depicted in Fig. 47d. The deflection of the equipotential lines at the liquid-air interface is due to the difference of dielectric properties of the materials.

## 4.4 Conclusions

We have developed a robust numerical algorithm for the study of systems with multiple phases under the presence of electric fields. To this end, we combined the mixed finite element method with a quasi-elliptic mesh generation scheme, which allows an accurate description of liquid-air and liquid-liquid interfaces that may undergo large deformations. The viscoelastic behaviour of the polymeric film was modelled using the PTT constitutive law. This scheme is quite robust for modelling viscoelastic flows and simulations up to high Weissenberg numbers were successful by using the EVSS-G/SUPG formulation for the numerical discretization and weighting of the constitutive equations.

We validated the code against earlier results in the literature and carried out a numerical investigation of the flow of both a Newtonian and a viscoelastic bilayer under the action of a homogeneous or a heterogeneous electric field imposed by the presence of either a flat or patterned electrode. Attention is focused on the non-linear dynamics of the flow, and the investigation of how the dynamics are influenced by the rheological and electrical properties of the materials and how in turn these may affect the morphological characteristics and the fabrication limits of this process. This work is still in progress.

## 4.5 Appendix: Finite element formulation

The physical domain was discretized using triangular elements. We approximate the velocity vector, the position vector and the potential with six-node Lagrangian basis functions, $\psi^j$, and the pressure, the elastic stresses, as well as the velocity gradients with three-node Lagrangian basis functions, $\chi^j$.

For the momentum, mass balances and the Laplace equation for the potential, we employ the finite element/Galerkin method, which after applying the divergence theorem results in the following weak forms:

$$\int_V \Big[ D_i \mathrm{Re} \left( \frac{\partial \mathbf{v}_i}{\partial t} + \mathbf{v}_i \cdot \nabla \mathbf{v}_i \right) \psi^j - P \nabla \psi^j + \nabla \psi^j \cdot \Sigma + 2 \nabla \psi^j \cdot \gamma_i + \mathrm{St} \psi^j \mathbf{e}_z \Big] \, dV - \int_S \left[ \mathbf{n} \cdot T_i \right] \psi^j dS = 0, \quad (230)$$

$$\int_V \left[\nabla \cdot \mathbf{v}_i\right] \chi^j dV = 0, \tag{231}$$

$$\int_V \left[\epsilon_i \nabla\phi_i \cdot \nabla\psi^j\right] dV - \int_S \left[\mathbf{n} \cdot \nabla\phi_i\right] \psi^j dS = 0. \tag{232}$$

where $dV$ and $dS$ are the differential volume and surface area, respectively. The surface integral that appears in the momentum equation is split into as many parts as the number of boundaries of the physical domain and the relevant boundary condition is applied therein.

The weak form of the mesh generation equations is derived similarly by applying the divergence theorem:

$$\int_V \left[\alpha \cdot \nabla\eta\right] \cdot \nabla\psi^j dV = 0, \tag{233}$$

$$\int_V \left[\left(\delta\sqrt{\frac{x_\xi^2 + y_\xi^2}{x_\eta^2 + y_\eta^2}} + (1-\delta)\right)\nabla\xi\right] \cdot \nabla\psi^j dV = 0. \tag{234}$$

The continuous approximation for the components of the velocity gradient tensor is written as

$$\int_V \left[G_i - \nabla\mathbf{v}_i\right] \chi^j dV = 0. \tag{235}$$

The constitutive equation due to its hyperbolic character is discretized using the streamline upwind Petrov-Galerkin (SUPG) method proposed by [90]

$$\int_V \Big[Y(\tau_{p,i})\Sigma_i + \mathrm{Wi}_i\hat{\Sigma}_i + 2\mathrm{Wi}_i(1-\beta_i)M_i\hat{\Pi}_i \\ -2(1-\beta_i)(1-Y(\tau_{p,i}))M_1\Pi_i\right] \omega^j dV = 0, \tag{236}$$

where $\Pi_i = (G_i + G_i^T)/2$ and the definition of the Gordon-Schowalter derivative is given by

$$\hat{X} = \frac{\partial X}{\partial t} + \mathbf{v}_i \cdot \nabla X - (\nabla\mathbf{v}_i - \xi_{s,i}\Pi_i)^T \cdot X - X \cdot (\nabla\mathbf{v}_i - \xi_{s,i}\Pi_i). \tag{237}$$

The weighting function $\omega^j$ is formed from the finite element basis function for the elastic stress components according to

$$\omega^j = \chi^j + \frac{h}{|\mathbf{v}_i|}\nabla\chi^j, \tag{238}$$

where $|\mathbf{v}_i|$ is the mean velocity in fluid $i$ and $h$ is a characteristic length in each element. The mean velocity $|\mathbf{v}_i|$ in an element is defined as the mean value of the velocity at the vertices of the corresponding element. As a characteristic length, $h$, we used the square root of the area of each triangular element.

# 5 Development of Navier-Stokes/Cahn-Hilliard (NS/CH) solver for the simulation of 3D two-phase flows in the presence of electric fields

## 5.1 Introduction

The development of a Navier-Stokes/Cahn-Hilliard (NS/CH) solver for the simulation of two-phase flows in the presence of electric field is described. The governing equations and numerical methods are presented, including the projection scheme, time-stepping algorithms and spatial discretization. Representative results obtained from several verification tests are shown, such as damped oscillations of a capillary wave between two superposed viscous fluids with the same dynamic viscosity, Rayleigh-Taylor instability, the rise of a gas bubble in air, and the two-dimensional (2d) and three-dimensional (3d) two-phase flow of Newtonian film in the presence of a spatially periodic electric field.

## 5.2 Navier-Stokes Solver

### 5.2.1 Equations for constant density and variable viscosity

The flow governing equations for constant density $\rho$ and variable viscosity $\eta$ in non-dimensional form are:

$$\nabla \cdot \mathbf{v} = 0 \tag{239}$$

$$\mathbf{v}_t + \mathbf{v} \cdot \nabla \mathbf{v} = -\nabla p + \frac{1}{\mathrm{Re}} \nabla \cdot \left[ \eta(c) \left( \nabla \mathbf{v} + \nabla \mathbf{v}^T \right) \right] \tag{240}$$

$$\eta = \eta' / \eta^* = c + (1 - c)\lambda_\eta, \tag{241}$$

where $\mathbf{v}$ is the fluid velocity, $p$ is the fluid pressure, $\rho^*$, $\eta^*$, $V^*$, $L^*$ are the reference values of the fluid density, the kinematic viscosity, and the characteristic velocity and length, respectively, and $Re = \rho^* V^* L^* / \eta^*$. The kinematic viscosity $\eta$ depends on the concentration field $c$, where $\lambda_\eta$ is the viscosity ratio between the two phases.

### 5.2.2 Equations for variable density and variable viscosity

The governing equations for variable density and variable viscosity are:

$$\mathbf{v}_t + \mathbf{v} \cdot \nabla \mathbf{v} = -\frac{1}{\rho} \nabla p + \frac{1}{\rho \mathrm{Re}} \nabla \cdot \left[ \eta(c) \left( \nabla \mathbf{v} + \nabla \mathbf{v}^T \right) \right] \tag{242}$$

$$\rho = \rho' / \rho^* = c + (1 - c)\lambda_\rho, \tag{243}$$

where the fluid density $\rho$ also depends on the concentration field $c$, $\rho^*$ is the reference value of the fluid density, and $\lambda_\rho$ is the density ratio between the two phases.

### 5.2.3 Numerical methods

*4.2.3.1 Time-stepping algorithms - Constant density, constant or variable viscosity*

The numerical algorithm used to solve the NS equations (239)-(241) is based on a semi-implicit, fractional step method. All spatial derivatives are discretized using a second-order central differencing scheme on a staggered grid. The time integration scheme CNRK2 incorporates an implicit second-order Crank–Nicolson method for the diffusion terms, and an explicit third-order Runge–Kutta method for the convection terms and the external body forces. The time integration is performed in three time steps $n-1$, $n$ and $n+1$. The first step $n$ is

$$\frac{\hat{u}_i^k - u_i^n}{\Delta t} = \gamma^k H_i^n + \rho^k H_i^{n-1} + \frac{\alpha^k}{2\mathrm{Re}} L_{jj}(\hat{u}_i^k + u_i^n) - \alpha^k G_i(p^n \sigma_1) \tag{244}$$

where $\gamma$, $\rho$, $\alpha$, $\sigma_1$ are the constants of the low storage third-order Runge–Kutta method $\rho_1 = 0$, $\rho_2 = -17/60$, $\rho_3 = -5/12$, $\gamma_1 = 8/15$, $\gamma_2 = 5/12$, $\gamma_3 = 3/4$, $\sigma_1 = 1$, $H_i$ are the nonlinear convection terms written in conservative form and the external Lorentz force, $L_{jj}$ is the Laplacian operator, and $G_i$ indicates the discrete pressure gradient operator, and $k$ is the intermediate time step between $n$ and $n+1$. Equation (244) can be rewritten for the difference of the fluid velocities $\Delta u_i = (u^k - u^n)_i$

$$\Delta u_i - \beta^k L_{jj} \Delta u_i = (\gamma^k H_i^n + \rho^k H_i^{n-1} - \alpha^k G_i p^n \sigma_1)\Delta t + 2\beta^k L_{jj} u_i^n \tag{245}$$

where $\beta^k = (\alpha^k/(2\mathrm{Re}))$. The intermediate velocity fluid velocity field at $k$-time step is globally divergence-free but it does not satisfy the continuity mass locally. In the second step, a globally and locally divergence-free fluid velocity field is predicted. This is achieved by using a scalar quantity $\phi$ (pseudo-pressure), which permits the evaluation of the fluid velocity at $n+1$ time step through the equation

$$\frac{u_i^{n+1} - \hat{u}_i^k}{\Delta t} = -\alpha^k G_i \phi \sigma_2 \tag{246}$$

If the discrete divergence operator is applied in Equation (246) and impose the mass continuity for the fluid velocity field at $n+1$ time step, $D_i u_i^{n+1} = 0$, an elliptic partial equation which permits the calculation of the pseudo-pressure $\phi$ is obtained

$$L_{jj}\phi = \frac{\sigma_2}{\alpha^k \Delta t} D_i \hat{u}_i^k \tag{247}$$

By solving numerically Equation (247) and substituting the quantity $\phi$ in Equation (246) the new fluid velocity field at $n+1$ time step is obtained, which satisfies the fluid mass continuity equation.

In the previous procedure, the knowledge and therefore the calculation of the fluid pressure were not necessary. However, in cases for which the knowledge of the pressure is required, the pressure can be determined by using the pseudo-presssure $\phi$

$$p^{n+1} = p^n + \phi - \beta L_{jj}\phi \tag{248}$$

and, therefore, the pressure gradient in Equation (244) is

$$-G_i \left[ p^n(\sigma_1 - \sigma_2) + p^{n+1}\sigma_2 \right] \tag{249}$$

In the case for which the time integration is based on 2nd order Adams-Bashforth method, the procedure is the same as that described above, with the exception that only two intermediate steps are needed and the constants $\rho$ and $\gamma$ are: $\rho_1 = -0.5$, $\rho_2 = 0$, $\rho_3 = 0$, $\gamma_1 = 1.5$, $\gamma_2 = 0$, $\gamma_3 = 0$. If $\sigma_1 = \sigma_2 = 1$, the pressure gradient is evaluated at $n+1$ time step, on the other hand for $\sigma_1 = 1$ and $\sigma_2 = 1/2$, the pressure gradient is evaluated at $n+1/2$ time step. In the former case, the accuracy is $\mathrm{O}(\Delta t)$, while in the latter is $\mathrm{O}(\Delta t^2)$. It has been found that the reduced accuracy gives a more stable scheme and it is more appropriate for time dependent simulations.

#### *4.2.3.2 Approximate factorization technique*

If the right hand side of Equation (245) is indicated for simplicity by $RHS_i$, it becomes

$$\left[ 1 - \beta^k (L_{i1} - L_{i2} - L_{i3}) \Delta u_i \right] = RHS_i \tag{250}$$

The approximate factorization technique consists of the replacement of the left hand side by the product of three matrices. By defining $A_{ij} = \beta^k L_{jj}$, Equation (250) becomes

$$(1 - A_{i1})(1 - A_{i2})(1 - A_{i3})\Delta u_i = RHS_i \tag{251}$$

It can be shown that, at order $\Delta t^3$, the left hand side of Equation (251) approximates the large sparse matrix in Equation (250). This approximation leads to the advantage of inverting tridiagonal matrices. Equation (251) can be written as

$$(1 - A_{i1})\Delta u_i^{**} = RHS_i \tag{252}$$

$$(1 - A_{i2})\Delta u_i^{*} = \Delta u_i^{**} \tag{253}$$

$$(1 - A_{i3})\Delta u_i = \Delta u_i^{*} \tag{254}$$

where $\Delta u_i^{**}$ and $\Delta u_i^{*}$ are intermediate quantities without any physical meaning.

#### *4.2.3.3 Projection - Pressure and velocity correction*

The fluid velocity field must satisfy the fluid mass continuity equation in every time step. The equation for the pseudo-pressure $\phi$ is

$$L_{jj}\phi = \frac{\sigma_2}{\alpha^k \Delta t} D_i \hat{u}_i^k \tag{255}$$

or

$$(L_{11} + L_{22} + L_{33})\phi_{ijl} = \frac{\sigma_2}{\alpha^k \Delta t} \Lambda_{ijl} \tag{256}$$

where $\Lambda_{ijl}$

$$\Lambda_{ijl} = \frac{\partial \hat{u}^k}{\partial x}\Big|_{i+\frac{1}{2},j+\frac{1}{2},l+\frac{1}{2}} + \frac{\partial \hat{v}^k}{\partial y}\Big|_{i+\frac{1}{2},j+\frac{1}{2},l+\frac{1}{2}} + \frac{\partial \hat{w}^k}{\partial z}\Big|_{i+\frac{1}{2},j+\frac{1}{2},l+\frac{1}{2}} \tag{257}$$

Equation (257) in discretized form using second-order central finite differences for the second derivatives becomes

$$\begin{aligned}
&\frac{\phi_{i+\frac{3}{2},j+\frac{1}{2},l+\frac{1}{2}} - 2\phi_{i+\frac{1}{2},j+\frac{1}{2},l+\frac{1}{2}} + \phi_{i-\frac{1}{2},j+\frac{1}{2},l+\frac{1}{2}}}{\Delta x^2} + \\
&\frac{\phi_{i+\frac{1}{2},j+\frac{3}{2},l+\frac{1}{2}} - 2\phi_{i+\frac{1}{2},j+\frac{1}{2},l+\frac{1}{2}} + \phi_{i+\frac{1}{2},j-\frac{1}{2},l+\frac{1}{2}}}{\Delta y^2} + \\
&\frac{\phi_{i+\frac{1}{2},j+\frac{1}{2},l+\frac{3}{2}} - 2\phi_{i+\frac{1}{2},j+\frac{1}{2},l+\frac{1}{2}} + \phi_{i+\frac{1}{2},j+\frac{1}{2},l-\frac{1}{2}}}{\Delta z^2} = \\
&\frac{\sigma_2}{\alpha^k \Delta t}\left(\frac{\hat{u}_{i+1,j+\frac{1}{2},l+\frac{1}{2}} - \hat{u}_{i,j+\frac{1}{2},l+\frac{1}{2}}}{\Delta x} + \right. \\
&\frac{\hat{v}_{i+\frac{1}{2},j+1,l+\frac{1}{2}} - \hat{v}_{i+\frac{1}{2},j,l+\frac{1}{2}}}{\Delta y} + \\
&\left.\frac{\hat{w}_{i+\frac{1}{2},j+\frac{1}{2},l+1} - \hat{w}_{i+\frac{1}{2},j+\frac{1}{2},l}}{\Delta z}\right)
\end{aligned} \tag{258}$$

Due to the periodicity, Fourier series can be used in the $x$ and $z$ directions for the $\phi$ and $\Lambda$ quantities

$$\begin{aligned}
\phi_{i,j,l} = &\sum_{k_1=-N_1/2}^{N_1/2+1}\sum_{k_3=0}^{N_3} \hat{\phi}(k_1,j,k_3) e^{\frac{t2\pi k_1 x}{L_x}} e^{\frac{t2\pi k_3 z}{L_z}} = \\
&\sum_{k_1=-N_1/2}^{N_1/2+1}\sum_{k_3=0}^{N_3} \hat{\phi}(k_1,j,k_3) e^{\frac{t2\pi k_1 i}{N_1}} e^{\frac{t2\pi k_3 i}{N_3}}
\end{aligned} \tag{259}$$

$$\begin{aligned}
\Lambda_{i,j,l} = &\sum_{k_1=-N_1/2}^{N_1/2+1}\sum_{k_3=0}^{N_3} \hat{\Lambda}(k_1,j,k_3) e^{\frac{t2\pi k_1 x}{L_x}} e^{\frac{t2\pi k_3 z}{L_z}} = \\
&\sum_{k_1=-N_1/2}^{N_1/2+1}\sum_{k_3=0}^{N_3} \hat{\Lambda}(k_1,j,k_3) e^{\frac{t2\pi k_1 i}{N_1}} e^{\frac{t2\pi k_3 i}{N_3}}
\end{aligned} \tag{260}$$

Equation (258) finally becomes

$$\sum_{k_1=-N_1/2}^{N_1/2+1}\sum_{k_3=0}^{N_3} \hat{\phi}(k_1'^2,j,k_3'^2) = \hat{\Lambda}(k_1',j,k_3') e^{\frac{t2\pi k_1 i}{N_1}} e^{\frac{t2\pi k_3 i}{N_3}} \tag{261}$$

where $k_1'^2, k_3'^2$ are the modified wavenumbers due to the use of the central finite differences for the second derivate

$$k_1^{'2} = \frac{2\left(cos(\frac{2\pi k_1}{N_1} - 1\right)}{\Delta x_1^2}, k_3^{'2} = \frac{2\left(cos(\frac{2\pi k_3}{N_3} - 1\right)}{\Delta x_3^2} \tag{262}$$

The Poisson equations for the pseudopressure is solved with FFT in the periodic directions and tridiagonal matrix inversion in the direction normal to the walls. The Poisson equation for the electric potential is solved in a similar manner.

*4.2.3.4 Time-stepping algorithms - Variable density, variable viscosity*

The projection method in the case with variable density and variable viscosity (Equations 242-243) is similar to that described above in Section 4.2.3.1. The first step for the Adams-Bashforth/Crank-Nikolson (CNAB2) scheme is

$$\begin{aligned} \frac{\hat{u}_i^k - u_i^n}{\Delta t} = \frac{1}{\rho^{n+1/2}} H_i^{n+1/2} + \frac{\alpha^k}{2\mathrm{Re}} L_{jj}(\mu^k, u_i^n) + \\ \frac{\alpha^k}{2\mathrm{Re}} L_{jj}(u_i^n, \mu^n) - \alpha^k G_i(p^{n-1/2}\sigma_1) \end{aligned} \tag{263}$$

where $H_i$ denotes the discrete convection operator and $L_{jj}$ the discrete diffusion operator. The intermediate velocity is corrected according to

$$\frac{u_i^{n+1} - \hat{u}_i^k}{\Delta t} = -\alpha^k G_i \phi \sigma_2 / \rho^{n+1/2} \tag{264}$$

The pressure is obtained from the requirement that the velocity field at time step $n+1$ is divergence-free constraint, i.e.,

$$D_i(G_i\phi/\rho_i^{n+1/2}) = \frac{\sigma_2}{\alpha^k \Delta t} D_i \hat{u}_i^k \tag{265}$$

The pressure is obtained by

$$p^{n+1/2} = p^{n-1/2} + \phi \tag{266}$$

The Poisson equation (265) is solved numerically by the succesive over-relaxation method (SSOR). In order ot speed up the convergence rate, the relaxation coeeficient is set larger than unity. All spatial discretizations are central finite difference schemes on a staggered grid.

*4.2.3.5 Summary of the time-stepping algorithms*

The NS/CH code implements the following different time-stepping algorithms:

– CNFE1 or SBDF1: 1st-order Crank-Nicolson, Foward-Euler or 1st-order Semi-implicit Backward Differentiation Formula. This algorithm is extremely

simple and needs no initialization need, but its 1st-order error scaling makes it practically worthless, except for initializing other algorithms.

– CNAB2 2nd-order Crank-Nicolson, Adams-Bashforth. A popular algorithm, but higher-frequency modes are poorly damped. It requires one initialization step.

– CNRK2: a three-substep, 2nd-order semi-implicit Crank-Nicolson/Runge-Kutta algorithm. It has 3rd-order scaling when applied to low-viscosity flows, even though it is theoretically 2nd-order. It requires no initialization.

– SBDF2: 2nd order, Semi-implicit Backward Differentiation Formulae, requiring 1 initialization step.

All the verification tests have been performed using the CNRK2 scheme. In the case of the two-phase flow of Newtonian film in the presence of a spatially periodic electric field, the SBDF2 scheme was also used.

## 5.3 Cahn-Hilliard Solver

### 5.3.1 Equations

The flow of two incompressible immiscible fluids (A and B) of different density and viscosity is considered here. Assuming that the fluid components are incompressible, the non-dimensional CH equation based on concentration $c$ formulation is

$$c_t + \mathbf{v} \cdot \nabla c = \frac{1}{\mathrm{Pe}} \nabla \cdot [M(c) \nabla \mu] \tag{267}$$

where $\mu$ and $M$ are the chemical potential and the mobility given by

$$\mu = f(c) - Cn \Delta c \tag{268}$$

$$M(c) = c(1 - c) \tag{269}$$

$Cn$ is the Cahn number and Pe is the Peclet number defined as

$$Cn = \epsilon^2 / \mu_* \tag{270}$$

$$\mathrm{Pe} = L_* V_* / (M_* \mu_*) \tag{271}$$

where $f(c) = F'(c)$ is the quartic free energy $F(c) = c^2(c-1)^2/4$.

### 5.3.2 Numerical methods

*4.3.2.1 Time integration*

*4.3.2.1.1 Explicit schemes of the CH solver*

In the explicit schemes, the following equation is numerically solved

$$\frac{c^{n+1} - c^n}{\delta t} = \left( -u_j \frac{\partial c}{\partial x_j} \right)^{n+1/2} + \frac{1}{\mathrm{Pe}} \left( \frac{\partial}{\partial x_j} M \frac{\partial \mu}{\partial x_j} \right)^{n+1/2} \tag{272}$$

where all the terms at the $n+1/2$ time step are explicitly calculated based on the values at the time steps $n$ and $n-1$ using the Adams-Bashforth (CHAB2) scheme or the 3rd order Runge-Kutta (CHRK2) scheme, similarly to the time integration schemes of the NS solver.

*4.3.2.1.2 Semi-implicit schemes of the CH solver*

In the semi-implicit schemes, the following equation is numerically solved

$$\begin{aligned}\frac{\frac{3}{2}c^{n+1}-2c^{n}+\frac{1}{2}c^{n-1}}{\delta t} &= \left(-u_j\frac{\partial c}{\partial x_j}\right)^{n+1/2}+\\ \frac{1}{\mathrm{Pe}}\frac{\partial}{\partial x_j}\left[M\frac{\partial}{\partial x_j}\left(F'-Cn^2\frac{\partial^2 c}{\partial x_i\partial x_j}\right)\right]^{n+1/2} &-\\ \frac{1}{\mathrm{Pe}}\frac{\partial}{\partial x_j}\left[M\frac{\partial}{\partial x_j}\left(Cn^2\frac{\partial^2 c}{\partial x_i\partial x_j}\right)\right]^{n+1}&\end{aligned} \tag{273}$$

where all terms at $n+1/2$ time step are explicitly calculated either using the Adams-Bashforth scheme (CHSIAB2) or the 3rd order Runge-Kutta scheme (CHSIRK2). Equation (273) is solved based on an iterative SSOR solver. In order to speed up the convergence rate, the relaxation coeeficient is set larger than unity. In general, a significanlty larger time time step $\Delta t$ can be used when solving the semi-implicit formulations of the CH solver as compared with the fully explicit schemes.

*4.3.2.2 Spatial discretization*

All terms related with chemical potential $\mu$ are descritized spatially based on second order central finite difference scheme. The convection terms can be discretized based on the 2nd order central finite differences (CD2), the 2nd order TVD upwind scheme (TVD2) and the 5th order WENO scheme (WENO5).

*4.3.2.2.1 TVD upwind scheme*

The TVD method for the advection of $\phi$ (or $c$) using the upwind scheme together with a piecewise linear reconstruction can be summarized as follows: A piecewise linear reconstruction is made:

$$\Phi(x,y)=\Phi_{i,j}+s^x_{i,j}(x-x_{i,j})+s^y_{i,j}(y-y_{i,j}) \tag{274}$$

The slopes $s^x_{i,j}$ and $s^y_{i,j}$ are calculated by:

$$s^x_{i,j}=\mathrm{Lim}(\frac{\Phi_{i+1,j}-\Phi_{i,j}}{\Delta x},\frac{\Phi_{i,j}-\Phi_{i-1,j}}{\Delta x}) \tag{275}$$

$$s^y_{i,j} = \mathrm{Lim}(\frac{\Phi_{i,j+1} - \Phi_{i,j}}{\Delta x}, \frac{\Phi_{i,j} - \Phi_{i,j-1}}{\Delta y}) \tag{276}$$

where $\mathrm{Lim}(x, y)$ defines the limiter. The Superbee limiter is defined as:

$$\mathrm{Lim}(x,y) = \begin{cases} \mathrm{sign}(x)\max(|x|,|y|) & \text{if } |x| \le |y| \le 0 \text{ and } xy > 0 \\ 2\mathrm{sign}(x)\min(|x|,|y|) & \text{if } |x|/2 \ge |y| \text{or } |y| \ge 2|x| \text{ and } xy > 0 \\ 0 & \text{if } xy < 0 \end{cases} \tag{277}$$

The fluxes $F = uc$ and $G = vc$ are approximated using the upwind scheme for the linear reconstruction defined by the

$$F_{i+\frac{1}{2},j} = \max(u_{i+\frac{1}{2},j}, 0)\Phi^-_{i+\frac{1}{2},j} + \min(u_{i+\frac{1}{2},j}, 0)\Phi^+_{i+\frac{1}{2},j} \tag{278}$$

$$G_{i,j+\frac{1}{2}} = \max(v_{i,j+\frac{1}{2}}, 0)\Phi^-_{i,j+\frac{1}{2}} + \min(v_{i,j+\frac{1}{2}}, 0)\Phi^+_{i,j+\frac{1}{2}} \tag{279}$$

where

$$\Phi^-_{i+\frac{1}{2},j} = \Phi_{i,j} + \frac{\Delta x}{2} s^x_{i,j},\ \Phi^-_{i,j+\frac{1}{2}} = \Phi_{i,j} + \frac{\Delta y}{2} s^y_{i,j} \tag{280}$$

$$\Phi^+_{i+\frac{1}{2},j} = \Phi_{i+1,j} + \frac{\Delta x}{2} s^x_{i+1,j},\ \Phi^+_{i,j+\frac{1}{2}} = \Phi_{i,j+1} + \frac{\Delta y}{2} s^y_{i,j+1} \tag{281}$$

*4.3.2.2.2 5th order WENO scheme*

In the 5th order WENO scheme, the numerical fluxes $F = uc$ (or $u\phi$) and $G = vc$ (or $v\phi$) are defined as

$$\begin{aligned} F_{i+\frac{1}{2},j} &= \int_{y_{i,j-\frac{1}{2}}}^{y_{i,j+\frac{1}{2}}} u_{i+\frac{1}{2},j}\phi_{i+\frac{1}{2},j} dy \\ G_{i,j+\frac{1}{2}} &= \int_{x_{i-\frac{1}{2},j}}^{x_{i+\frac{1}{2},j}} v_{i,j+\frac{1}{2}}\phi_{i,j+\frac{1}{2}} dx \end{aligned} \tag{282}$$

A numerical approximation for the fluxes (282) can be written:

$$\begin{aligned} F_{i+\frac{1}{2},j} &\approx \begin{cases} u_{i+\frac{1}{2},j}\bar{\phi}^+_{i-\frac{1}{2},j} & \text{, if } u_{i+\frac{1}{2},j} > 0 \\ u_{i+\frac{1}{2},j}\bar{\phi}^-_{i+\frac{1}{2},j} & \text{, if } u_{i+\frac{1}{2},j} < 0 \end{cases} \\ G_{i,j+\frac{1}{2}} &\approx \begin{cases} v_{i,j+\frac{1}{2}}\bar{\phi}^+_{i,j-\frac{1}{2}} & \text{, if } v_{i,j+\frac{1}{2}} > 0 \\ v_{i,j+\frac{1}{2}}\bar{\phi}^-_{i,j+\frac{1}{2}} & \text{, if } v_{i,j+\frac{1}{2}} < 0 \end{cases} \end{aligned} \tag{283}$$

where

$$\phi^\pm_{i+\frac{1}{2},j} = \sum_{k=1}^{3} \omega_k \phi^{\pm,k}_{i+1/2,j} \tag{284}$$

and

$$\begin{aligned}\phi^{\pm,1}_{i+1/2,j} &= +\frac{1}{3}q^{\pm}_1 - \frac{7}{6}q^{\pm}_2 + \frac{11}{6}q^{\pm}_3 \\ \phi^{\pm,2}_{i+1/2,j} &= -\frac{1}{6}q^{\pm}_2 + \frac{5}{6}q^{\pm}_3 + \frac{1}{3}q^{\pm}_4 \\ \phi^{\pm,3}_{i+1/2,j} &= +\frac{1}{3}q^{\pm}_3 + \frac{5}{6}q^{\pm}_4 - \frac{1}{6}q^{\pm}_5\end{aligned} \tag{285}$$

and

$$q^k_+ = \bar{\phi}_{i-4+k,j} q^k_- = \bar{\phi}_{i+5+k,j} \tag{286}$$

The coefficients $\omega_k$ are a convex combination ($\omega_1 + \omega_2 + \omega_3 = 1$) and are computed for $\omega^{\pm}$ by the following expression of $\alpha^{\pm}$

$$\omega^{\pm}_k = \alpha^{\pm}_k / \sum_{i=1}^{3} \alpha^{\pm}_i \tag{287}$$

with the $\alpha_k$ defined as

$$\begin{aligned}\alpha^{\pm}_1 &= \frac{1}{10}\left(\frac{1}{\epsilon + IS^{\pm}_1}\right)^2 \\ \alpha^{\pm}_2 &= \frac{6}{10}\left(\frac{1}{\epsilon + IS^{\pm}_2}\right)^2 \\ \alpha^{\pm}_3 &= \frac{3}{10}\left(\frac{1}{\epsilon + IS^{\pm}_3}\right)^2\end{aligned} \tag{288}$$

where $\epsilon$ ensures the denominator to be different from zero and the IS some Level Set "regularity" given by:

$$\begin{aligned}IS^{\pm}_1 &= \frac{13}{12}(q^{\pm}_1 - 2q^{\pm}_2 + q^{\pm}_3)^2 + \frac{1}{4}(q^{\pm}_1 - 4q^{\pm}_2 + 3q^{\pm}_3)^2 \\ IS^{\pm}_2 &= \frac{13}{12}(q^{\pm}_2 - 2q^{\pm}_6 + q^{\pm}_4)^2 + \frac{1}{4}(q^{\pm}_2 - q^{\pm}_4)^2 \\ IS^{\pm}_3 &= \frac{13}{12}(q^{\pm}_3 - 2q^{\pm}_4 + q^{\pm}_5)^2 + \frac{1}{4}(3q^{\pm}_3 - 4q^{\pm}_4 + q^{\pm}_5)^2\end{aligned} \tag{289}$$

Another possible choice would be the so-called "optimum" WENO, where the $\omega_k$ are fixed to the values $(\omega_1, \omega_2, \omega_3) = (0.1, 0.6, 0.3)$.

*4.3.2.3 Surface tension force formulation*

The following three models of surface tension force have been included in the NS/CH solver:

$$F_{st} = \frac{\sigma\alpha}{\epsilon}\mu\nabla c \ \text{ (Model-1)} \tag{290}$$

$$F_{st} = -\frac{\sigma\alpha}{\epsilon}c\nabla\mu \ \text{ (Model-2)} \tag{291}$$

$$F_{st} = -\sigma\nabla\cdot\left(\frac{\nabla c}{|\nabla c|}\right)\epsilon\alpha|\nabla c|^2\frac{\nabla c}{|\nabla c|} \ \text{ (Model-3)} \tag{292}$$

where $\alpha = 6\sqrt{2}$, $\epsilon$ is a small positive parameter and $\sigma$ is the surface tension coefficient.

## 5.4 Code validation

### 5.4.1 Verification test #1

The governing equation in the absence of flow is the Cahn-Hilliard equation:

$$\frac{\partial c(\mathbf{x},t)}{\partial t} = \nabla \cdot [M(c(\mathbf{x},t))\nabla\mu(c(\mathbf{x},t))] \tag{293}$$

where $c$ is the mass concentration, $M$ is the variable mobility, and $\mu$ is the chemical potential given by:

$$\mu(c(\mathbf{x},t)) = F'(c(\mathbf{x},t)) - \epsilon^2\Delta c(\mathbf{x},t) \tag{294}$$

where $\epsilon$ is a positive constant and $F(c)$ is the Helmholtz free energy given by

$$F(c) = \frac{1}{4}c^2(1-c)^2 \tag{295}$$

The initial data is

$$c_0(x,y) = 0.5 + 0.12cos(2\pi x)cos(2\pi y) + 0.2cos(2\pi x)cos(3\pi y) \tag{296}$$

Equations (293) and (294) are solved on a square domain $[0,1]\times[0,1]$ using a uniform mesh of $33\times33$ grid points ($h = 1/32$). The time step is $\Delta t = 5\times10^{-6}$ and $\epsilon = 0.01$. Zero Neumann boundary conditions are imposed at $x = 0, 1$, and $y = 0, 1$. A constant mobility $M$ is considered. Figure 48 shows a comparison of the present model against the results of Kim et al. [96] based on a mesh of $256\times256$ grid points. It can be seen that the energy is non-increasing and tends to a constant value. The concentration phase separates and depletes the center region of the domain. The phase accumulates at the y boundaries, which then straighten to lower the energy and to subsequently form two horizontal bands.

### 5.4.2 Verification test #2

In this verification test, Equations (293) and (294) are solved together with the following flow equations:

$$\nabla \cdot \mathbf{v} = 0 \tag{297}$$

$$\mathbf{v}_t + \mathbf{v}\cdot\nabla\mathbf{v} = -\nabla p - \frac{We_s^{-1}}{\epsilon}c\nabla\mu + \frac{1}{\mathrm{Re}}\nabla\cdot\left[\eta(c)\left(\nabla\mathbf{v} + \nabla\mathbf{v}^T\right)\right] \tag{298}$$

where the extra stress due to the concentration gradients (i.e., interfaces) is $-We_s^{-1}/\epsilon c\nabla\mu$, Re is the Reynolds number, $We_s$ is proportional to $We$ number given by

$$We = We_s/\int_0^1 \sqrt{2F(c)}dc \tag{299}$$

and $\eta$ is the non-dimensional viscosity, which is assumed to depend on the mass concentration $c$. The same initial concentration as in Eq. (296) is considered, while the initial velocity is taken to be:

$$u(x,y) = -sin^2(\pi x)sin(2\pi y) \tag{300}$$

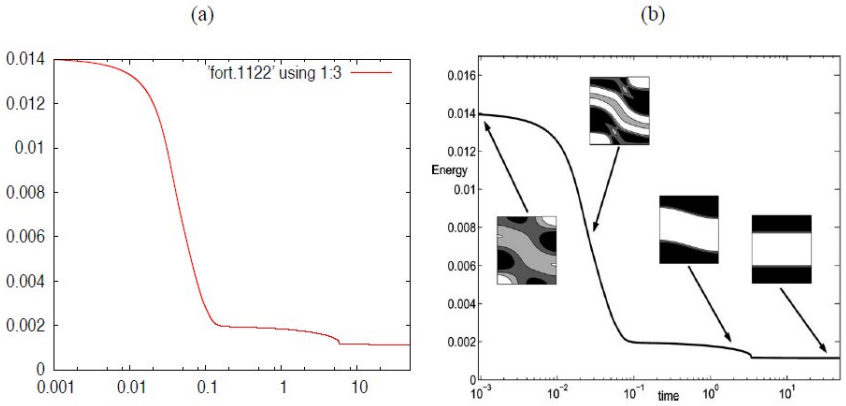


Figure 48: Time evolution of energy predicted by the present model (a) compared with the results of Kim et al. [96] (b).

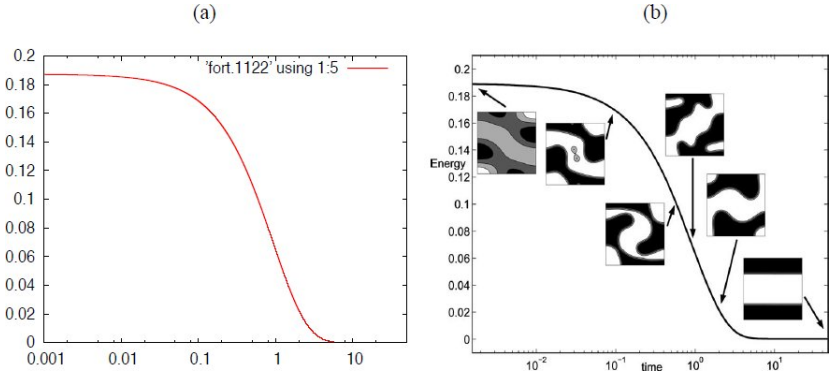


Figure 49: Time evolution of the total energy in the presence of flow predicted by the present model (a) compared with the results of Kim et al. [96] (b).

$$v(x,y) = sin^2(\pi y)sin(2\pi x) \tag{301}$$

The viscosity $\eta$ is constant and Re = 100, and $We_s = 100$, which corresponds to the physical Weber number $We = 848.5$. No-slip boundary conditions are imposed at the boundaries of the domain. Figure 49 shows the time evolution of the total energy predicted by the present model and by Kim et al. [96]. The total energy is decreased to a constant value.

### 5.4.3 Verification test #3: Surface tension force formulation

In this verification test, a drop placed within another fluid. The concentration is defined as

$$c(x,y) = \frac{1}{2}(1 + tanh\frac{1-\sqrt{x^2+y^2}}{2\sqrt{2}\epsilon}) \tag{302}$$

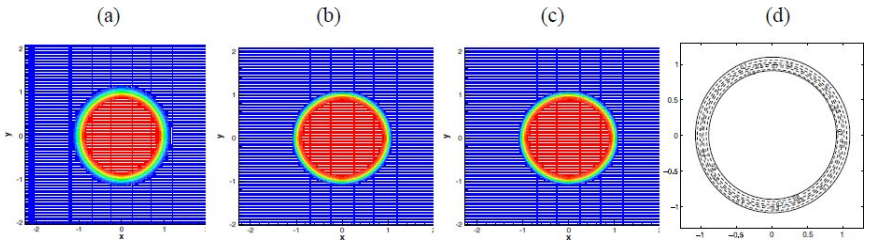


Figure 50: Contours plot of the pressure field obtained by the Model-1 (a), Model-2 (b) and Model-3 (c) of the surface tension force formulation compared with the results of Kim et al. [96] (d).

In the equilibrium state of the droplet, the velocity vanishes and therefore the pressure gradient should balance the surface tension force:

$$\nabla P = F_{st,i} \tag{303}$$

By taking divergence operator to Eq. (303), the resulting equation is solved numerically by with $R = \sigma = 1$, $256 \times 256$ mesh, the computational domain $[4, 4] \times [4, 4]$, and $\epsilon = 0.03$. Figure 50 shows the isocontours of the pressure field (at $p = 0.1, 0.3, 0.5, 0.7, 0.9$) along with the concentration (solid circles) at $c = 0.1$ and 0.9 obtained by the the three models of surface tension force formulation. It can be seen that the pressure changes within interface region and Laplace law is well verified for all models, in agreement with the numerical results of Kim [97].

#### 5.4.4 Verification test #4: Capillary wave, matched density $\rho_1 = \rho_2$ case

The capillary wave problem was used as a verification test. The lighter fluid (fluid A) resides in the top half of the domain, and the heavier fluid (fluid B) is in the bottom half of the domain, $g$ denotes the magnitude of the gravitational acceleration, which points downward, $\sigma$ denotes the surface tension, and $\nu$ denotes the kinematic viscosity of the two fluids. The two fluids may have different densities and dynamic viscosities, but must have the same kinematic viscosity. In this case, Prosperetti [98] obtained an exact standing-wave solution to the initial-value problem associated with the small-amplitude waves on the interface between two incompressible viscous fluids in an infinite domain.

The computational domain is $\Omega = \{(x, y) : 0 \leq x \leq 1, -1 \leq y \leq 1\}$. The equilibrium position of the fluid interface coincides with the $x$-axis, and the capillary wavelength equals the dimension of the domain in $x$-direction. The initial amplitude of the perturbation wave is $H_0 = 0.01$. Zero initial velocity is assumed and the initial phase concentration is given by the following hyperbolic tangent function:

$$c(x, y) = \frac{1}{2}\left(1 - tanh\frac{y - 0.5 - 0.01cos(2\pi x}{2\sqrt{2}\epsilon}\right) \tag{304}$$

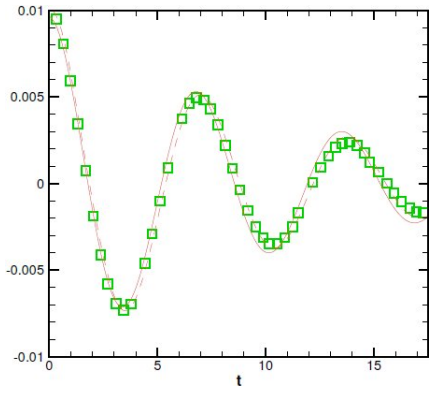


Figure 51: Capillary wave with matched density $\rho_1 = \rho_2 = 1$. Comparison of time histories of capillary wave amplitude obtained by different computational meshes ($32 \times 32$ solid line, $64 \times 64$ dashed line) against the capillary-wave exact solution by Prosperetti [98] (taken from Gueyffier et al. [99]).

Two uniform computational meshes of $32 \times 32$ and $64 \times 64$ grid points were used. Periodic conditions were imposed along the $x$-direction for both the velocity and the concentration. In the $y$-direction, no-slip conditions for the velocity and zero Neumann for the concentration were imposed at the walls $y = 0, 1$. A case with matched density for the two fluids, $\rho_1 = \rho_2 = 1$ was assumed, $\mu_1 = \mu_2 = \rho_1\nu = \rho_2\nu = 0.01$. A constant mobility of $M = 10^{-5}$ was used, while $g = 0$, $\sigma = 1$, and $\epsilon = 0.02$ ($32 \times 32$) and $\epsilon = 0.01$ ($64 \times 64$).

Figure 51 shows a comparison of the present model against the analytical results for the two meshes. A good agreement can be seen.

### 5.4.5 Verification test #5: Rayleigh-Taylor instability

The Rayleigh–Taylor instability would occur for any perturbation along the interface between a heavy fluid (A) on top of a lighter fluid (B), and is characterized by the density difference between the two fluids. The density difference is represented by the Atwood ratio $At = (\rho_A - \rho_B)/(\rho_A + \rho_B)$. The initial growth and long-time evolution of Rayleigh-Taylor instability has been investigated by Tryggvason [100] for inviscid incompressible flows with zero surface tension at $At = 0.50$. Guermond et al. [101] studied this stability problem at the same value of $At$ but accounted for viscous effects.

The governing equations are:

$$\frac{\partial C}{\partial t} + \mathbf{v} \cdot \nabla C - \frac{1}{\mathrm{Pe}} \nabla \cdot (M \nabla \phi) = 0 \tag{305}$$

$$\phi = \frac{\delta F}{\delta C} = \epsilon^{-1} \sigma \alpha \psi'(C) - \epsilon \sigma \alpha \Delta C \tag{306}$$

$$\nabla \cdot \mathbf{v} = 0 \tag{307}$$

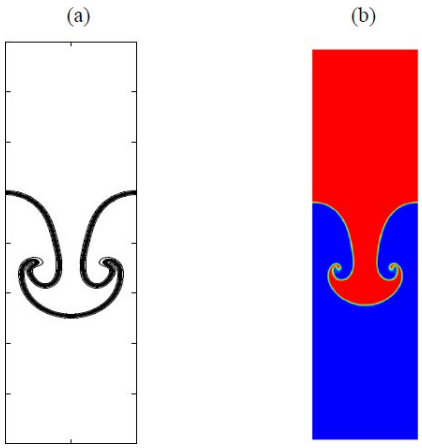


Figure 52: Rayleigh-Taylor instability simulation at $t = 1.5$ produced by the present model (a) compared with the results of Ding et al. [102].

$$\rho\left[\frac{\partial \mathbf{v}}{\partial t} + \mathbf{v}\cdot\nabla\mathbf{v}\right] = -\nabla p + \frac{1}{\mathrm{Re}}\nabla\cdot\left[\mu(\nabla\mathbf{v} + \nabla v^T)\right] + \bar{\mathbf{f}} \tag{308}$$

$$\bar{\mathbf{f}} = \frac{\phi\nabla C}{\mathrm{ReCa}} \tag{309}$$

$$\bar{\rho} = \rho/\rho_A = C + (1-C)\lambda_\rho \tag{310}$$

$$\bar{\mu} = \mu/\mu_A = C + (1-C)\lambda_\mu \tag{311}$$

where the density ratio and viscosity ratio are $\rho = \rho_A/\rho_B$ and $\mu = \mu_A/\mu_B$, respectively, $\mathrm{Re} = \rho_A LU/\mu_A$ is the Reynolds number, $\mathrm{Ca} = \mu_A U/\sigma$ is the capillary number, $\mathrm{Pe} = LU/(M_c\phi_c)$ is the Peclet number, and $Cn = \epsilon/L$ is the a Cahn number, where $L$ is a global characteristic length scale and $U$ is a characteristic velocity, and $M_c$ and $\phi_c$ are the characteristic values of mobility and chemical potential.

The same case as in Guermond et al. [101] and Ding et al. [102] is considered, i.e., at $At = 0.5$ and $\mathrm{Re} = 3000$, with the initial interface being located in a rectangular domain $[0, L] \times [0, 4L]$ at $y(x) = 2L + 0.1Lcos(2\pi x/L)$, which represents a planar interface superimposed by a perturbation of wave number $k = 1$ and amplitude $0.1L$. In the present case of zero surface tension, the Cahn-Hilliard equation is used for interface tracking only. The simulation is carried out on $100 \times 400$ grid points, the Cahn number is proportional to the mesh size $h$ as $Cn = 0.3h = 0.003$ and the time step $\Delta t = 3.5 \times 10^{-6}$.

Figure 52 shows the interface at $t = 1.5$. A good agreement with the results of Ding et al. [102] is observed.

Figure 53 shows the effect of grid size on the numerical solution. Three meshes were examined $32 \times 64$ ($Cn = 0.009375$), $64 \times 128$ ($Cn = 0.0046875$), $128 \times 256$ ($Cn = 0.00234375$) and in a smaller rectangular domain $[0, L] \times [0, 2L]$. The advection terms were discretized based on WENO5 scheme. It can be seen

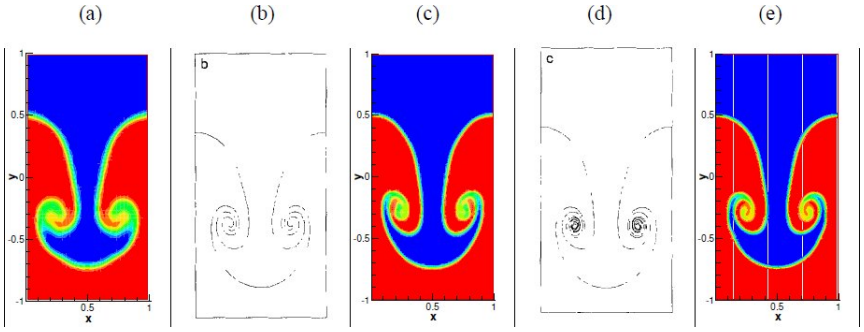


Figure 53: Rayleigh–Taylor instability simulation at $t = 1.75$ produced by the present model based on $32 \times 64$ (a), $64 \times 128$ (c), $128 \times 256$ (e) mesh, compared with the results of Tryggvason [100] on $32 \times 64$ (b), $64 \times 128$ (d) mesh.

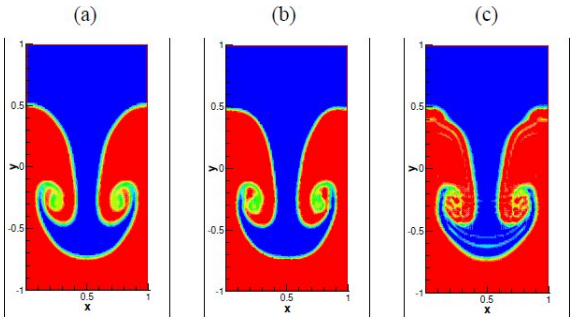


Figure 54: Rayleigh–Taylor instability simulation at $t = 1.75$ produced by the present model based on WENO5 scheme (a), TVD2 upwind scheme (b), and 2nd order central finite differences (c).

that as the grid size gets finer, more detailed structures appear. The present results are also in good qualitative agreement with those of Tryggvason [100] using level set method.

Figure 54 shows the effect of the spatial discretization of the advection terms of the CH equation. It can be seen that WENO5 scheme is slightly better than TVD2 upwind scheme, and both are significantly better than 2nd order central finite differences. The simulations were conducted on a $64 \times 128$ mesh in a smaller rectangular domain $[0, L] \times [0, 2L]$.

### 5.4.6 Verification test #6: Rising bubble

The rise of a gas bubble in a liquid is computed in order to validate the capability of the NS/CH solver to simulate high density and viscosity ratio two-phase flows. The bubble radius is $R$, the densities of air and water are $\rho_{air}$ and $\rho_{water}$, respectively. The viscosities are $\eta_{air}$ and $\eta_{water}$. The non-dimensional

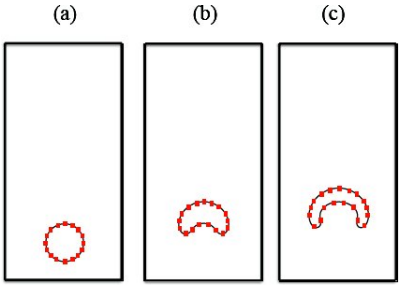


Figure 55: Evolution of a rising bubble with Re = 100, $B = 200$, a mesh $128 \times 256$, $h = \pi/128$, $\epsilon = 0.015$, density ratio $\rho_{water}/\rho_{air} = 1000$, and viscosity ratio $\eta_{water}/\eta_{air} = 100$, at times $t = 0, 2.1, and 3$, compared with the results of Kim [97].

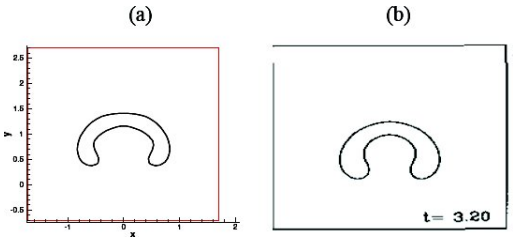


Figure 56: Comparison of the present results with diffuse interface (a) with those produced with level set method Sussman et al. [103].

parameters are the Bond number $B = 4\rho_{water}gR/\sigma$ and the Reynolds number $\mathrm{Re} = (2R)^{3/2}g^{1/2}\rho_{water}/\eta_{water}$, and $g$ represents a unit gravitational force. Figure 55 shows the evolution of a rising bubble with $Re = 100$, $B = 200$, a mesh $128 \times 256$, $h = \pi/128$, $\epsilon = 0.015$, density ratio $\rho_{water}/\rho_{air} = 1000$, and viscosity ratio $\eta water/\eta air = 100$. The present results with diffuse-interface model qualitatively compares well to the results from Kim [97].

Figure 56 shows a comparison of the present results with diffuse-interface model those produced using level set method by Sussman et al. [103] at non-dimensional time $t = 3.2$. The mesh size is $41 \times 41$ while it is $141 \times 141$ in Sussman et al. (1988). Once again, a reasonably acceptable agreement is observed.

### 5.4.7 Verification test #7: 2D Newtonian film in the presence of a spatially periodic electric field

.

Figure 57 shows the geometry and flow configuration of the problem under investigation, consisting of two perfect dielectric fluids between two rigid, and impermeable electrodes. $w$ and $p$ denote the width and the height of the protrusions, respectively, and $s$ denotes the spacing between the protrusions.

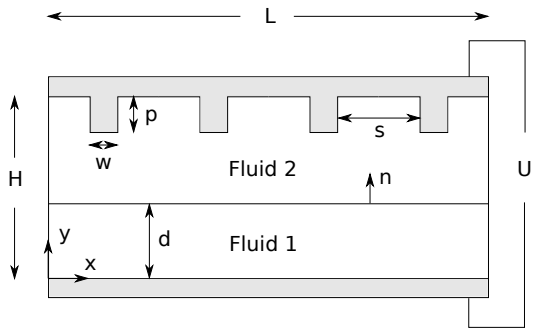


Figure 57: Geometry and flow configuration of the verification test #7.

The bottom fluid is considered to be a water film surrounded by air, with initial thickness, $d$. Both fluids, which are initially stationary, are taken to be incompressible with the lower (upper) fluid having a density $\rho_1$ ($\rho_2$), dielectric constants $\epsilon_1$ ($\epsilon_2$), and viscosity $\mu_1$ ($\mu_2$). The surface tension of the water-air interface, $\sigma$, is assumed to be constant. The top and bottom electrodes are maintained at constant potentials $V(y = H(x)) = U$ and $V(y = 0) = 0$, respectively.

The governing equations are:

$$\nabla \cdot (\epsilon_0 \epsilon_r(C) \nabla V) = 0 \tag{312}$$

$$\frac{\partial C}{\partial t} + \mathbf{v} \cdot \nabla C - \frac{1}{\mathrm{Pe}} \nabla \cdot (M \nabla \phi) = 0 \tag{313}$$

$$\phi = F'(C) - Cn^2 \nabla^2 C \tag{314}$$

$$\nabla \cdot \mathbf{v} = 0 \tag{315}$$

$$\rho \left[ \frac{\partial \mathbf{v}}{\partial t} + \mathbf{v} \cdot \nabla \mathbf{v} \right] = -\nabla p + \frac{1}{\mathrm{Re}} \nabla \cdot \left[ \mu (\nabla \mathbf{v} + \nabla v^T) \right] + \bar{\mathbf{f}} \tag{316}$$

$$\bar{\mathbf{f}} = \frac{\phi \nabla C}{\mathrm{ReCa}} - \frac{1}{2} \epsilon_0 E^2 \nabla \epsilon_r(C)$$

or (317)

$$\bar{\mathbf{f}} = -\frac{1}{\mathrm{ReCa}} \nabla \cdot \left( \frac{\nabla c}{|\nabla c|} \right) \epsilon \alpha |\nabla c|^2 \frac{\nabla c}{|\nabla c|} - \frac{1}{2} \epsilon_0 E^2 \nabla \epsilon_r(C)$$

$$\bar{\rho} = \rho / \rho_1 = C + (1 - C) \lambda_\rho \tag{318}$$

$$\bar{\mu} = \mu / \mu_1 = C + (1 - C) \lambda_\mu \tag{319}$$

$$\bar{\epsilon} = \epsilon / \epsilon_1 = C + (1 - C) \lambda_\epsilon \tag{320}$$

All quantities are scaled using as characteristic length the maximum distance between the top and bottom electrodes, $H_m$, the characteristic velocity $V* = \epsilon_0 U^2 / \mu_1 H_m$ and the electric potential is scaled with the potential difference $U$. The relevant dimensionless groups that emerge are the Reynolds

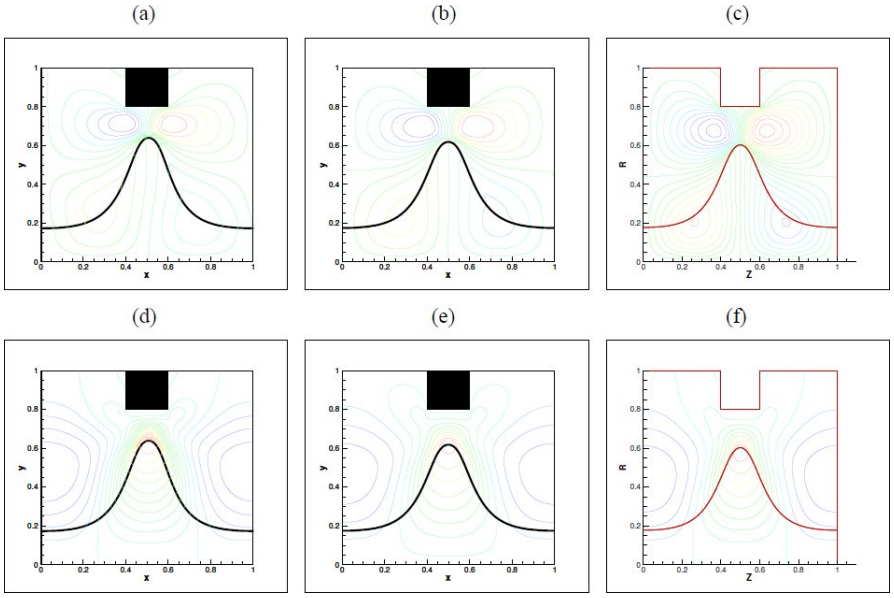


Figure 58: Contours of $u$ (a), (b),(c), $v$ (d),(e),(f) at $t = 26.4$ for $Re = 10$, $Ca = 30$, $Cn = 0.0025$, $d = 0.3$, $s = 0.8$, $p = 0.2$, $w = 0.2$, $L = 1$, $\lambda_\rho = 0.001$, $\lambda_\mu = 0.001$, and $\lambda_\epsilon = 2.5$, (a),(d) Pe = 800, (b),(e) Pe = 100, (c),(f) results of Karapetsas & Bontozoglou [95].

number, $\mathrm{Re} = \rho_1 V * H_m/\mu_1$, the capillary number, $Ca = \mu_1 V */\sigma$, the density ratio, $\lambda_\rho = \rho_2/\rho_1$, the viscosity ratio, $\lambda_m u = \mu_2/\mu_1$, the dielectric constants ratio $\lambda_\epsilon = \epsilon_1/\epsilon_2$, $\mathrm{Pe} = H_m V^*/(M^*\phi^*)$ is the Peclet number, and $Cn = \epsilon/H_m$ is the Cahn number. $\epsilon_0$ is the permittivity of vacuum, $\epsilon_r(C)$ the dielectric constant, $V$ the electric potential, and $\bar{E} = -\nabla V$ is the electric strength. The 2d/3d roughness elements are numerically treated by an immersed boundary method, which consists of imposing zero values to all fluid velocity components on the stationary boundary surface that does not necessarily coincide with the computational grid (see, for details, Fadlun et al. [104]). In accordance with the aforementioned studies, zero velocities are imposed in the grid points within the roughness elements. At the first grid point outside each roughness element, all the convection and viscous derivatives are discretized by using the distance between the grid point and the boundary of the wall disturbance and not the actual mesh size.

Figure 58 shows the distributions of the velocity components $u$ and $v$ predicted by the diffuse interface model and Figure 59 shows the distributions of pressure $p$ and electric potential $V$. The present results are compared with the corresponding results of Karapetsas & Bontozoglou [95]. The non-dimensional time is $t = 26.4$ (26.3 in Karapetsas & Bontozoglou [95]), $Re = 10$, $Ca = 30$, $Cn = 0.0025$, $d = 0.3$, $s = 0.8$, $p = 0.2$, $w = 0.2$, $L = 1$, $\lambda_\rho = 0.001$, $\lambda_\mu = 0.001$,

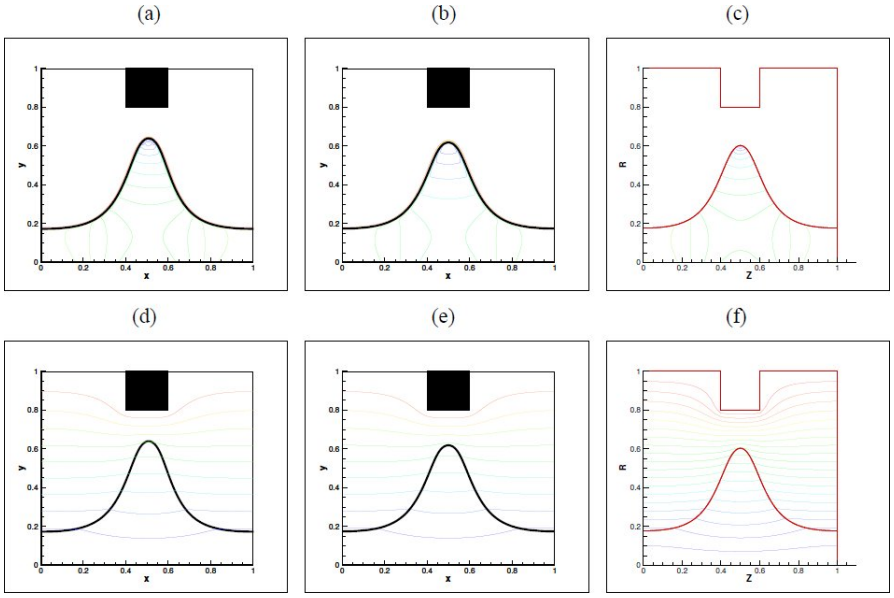


Figure 59: Contours of $p$ (a), (b),(c), $V$ (d),(e),(f) at $t = 26.4$ for $Re = 10$, $Ca = 30$, $Cn = 0.0025$, $d = 0.3$, $s = 0.8$, $p = 0.2$, $w = 0.2$, $L = 1$, $\lambda_\rho = 0.001$, $\lambda_\mu = 0.001$, and $\lambda_\epsilon = 2.5$, (a),(d) Pe = 800, (b),(e) Pe = 100, (c),(f) results of Karapetsas & Bontozoglou [95].

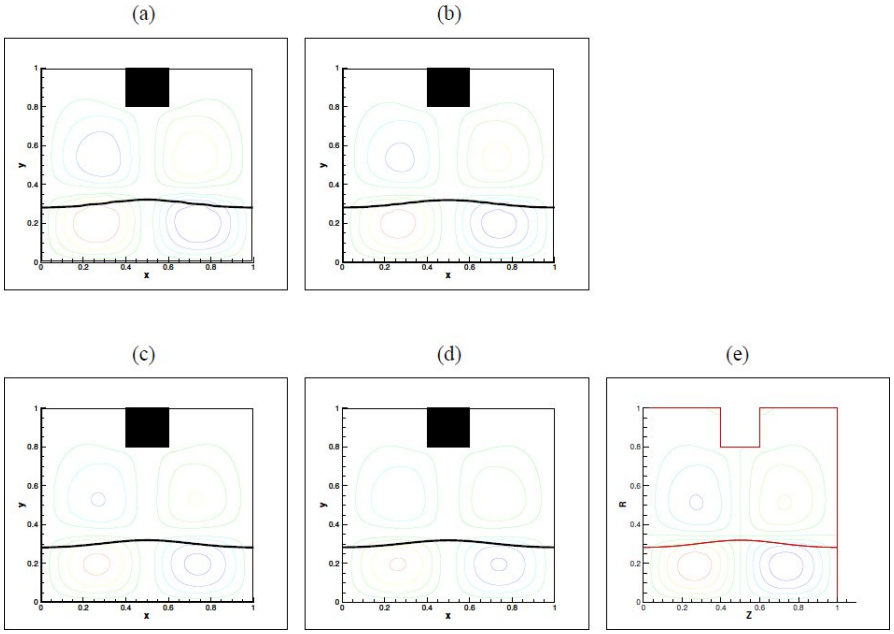


Figure 60: Contours of $u$ produced by a mesh of $80 \times 80$ (a), $120 \times 120$ (b), $160 \times 160$ (c), $240 \times 240$ (d), results from Karapetsas & Bontozoglou [95] (e) at $t = 7.8$ for Re $= 10$, Ca $= 30$, Pe $= 800$, $Cn = 0.0025$, $d = 0.3$, $s = 0.8$, $p = 0.2$, $w = 0.2$, $L = 1$, $\lambda_\rho = 0.001$, $\lambda_\mu = 0.001$, and $\lambda_\epsilon = 2.5$.

and $\lambda_\epsilon = 2.5$ for two values of Pe $= 800$ and 100. The computational mesh is $160 \times 160$. It can be seen that both the features of the interface predicted by the diffuse interface model, as well as the distributions of $u$, $v$, $p$, $V$ are in good qualitative agreement with the results of Karapetsas & Bontozoglou [95].

Figures 60 and 61 shows the effect of grid refinement on the distributions of the velocity components $u$ and $v$ produced by the diffuse interface model at non-dimensional time $t = 7.8$. Four meshes were examined, $80 \times 80$, $120 \times 120$, $160 \times 160$, and $240 \times 240$. The parameters are Re $= 10$, Ca $= 30$, Pe $= 800$, $Cn = 0.0025$, $d = 0.3$, $s = 0.8$, $p = 0.2$, $w = 0.2$, $L = 1$, $\lambda_\rho = 0.001$, $\lambda_\mu = 0.001$, and $\lambda_\epsilon = 2.5$. It can be seen that, for all meshes, the qualitative characteristics of the distributions are in good agreement with the results of Karapetsas & Bontozoglou [95]. However, a small distortion can be observed in the small size meshes $80 \times 80$, $120 \times 120$ near the interface, which is eliminated with further grid refinement. In contrast, the interface seems to be little affected by the grid resolution, and it is well captured by all grids used.

Figure 62 shows the time evolution of the maximum and minimum amplitude of the interfacial perturbation for various meshes and values of Peclet number. A very good agreement is observed with grid refinement. A reduction in Pe leads to an improvement of the predictions based on the present diffuse interface

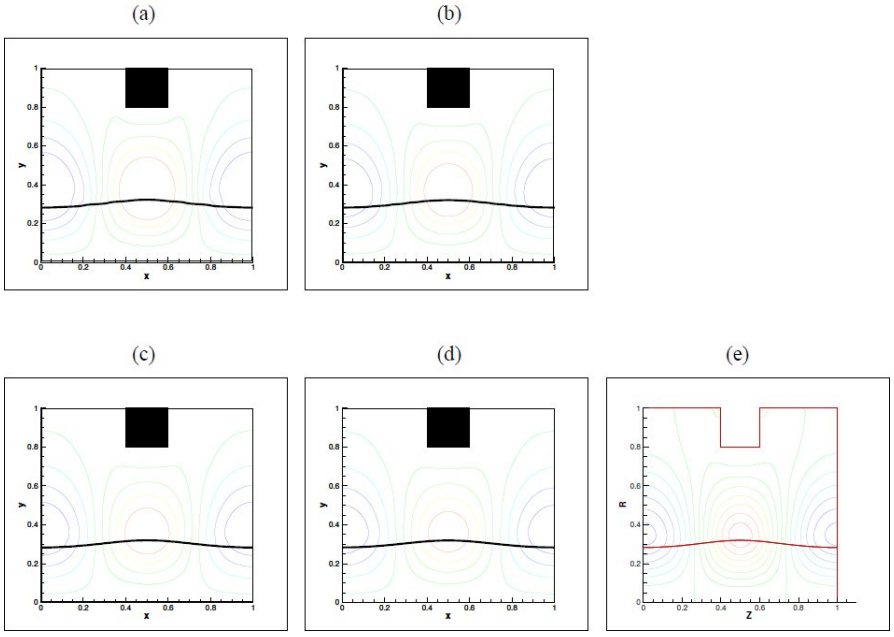


Figure 61: Contours of $v$ produced by a mesh of $80 \times 80$ (a), $120 \times 120$ (b), $160 \times 160$ (c), $240 \times 240$ (d), results from Karapetsas & Bontozoglou [95] (e) at $t = 7.8$ for Re $= 10$, Ca $= 30$, Pe $= 800$, $Cn = 0.0025$, $d = 0.3$, $s = 0.8$, $p = 0.2$, $w = 0.2$, $L = 1$, $\lambda_\rho = 0.001$, $\lambda_\mu = 0.001$, and $\lambda_\epsilon = 2.5$.

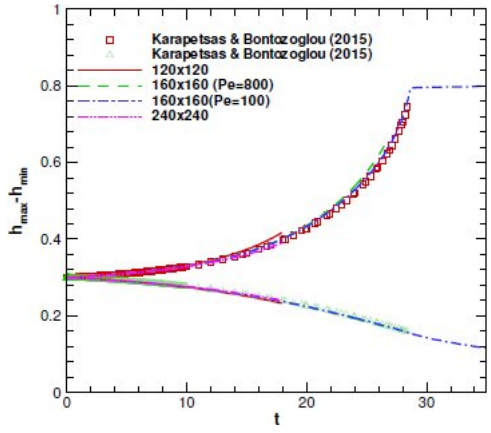


Figure 62: Evolution of the amplitude for $Re = 10$, $Ca = 30$, Pe $= 800$, $Cn = 0.0025$, $d = 0.3$, $s = 0.8$, $p = 0.2$, $w = 0.2$, $L = 1$, $\lambda_\rho = 0.001$, $\lambda_\mu = 0.001$, and $\lambda_\epsilon = 2.5$.

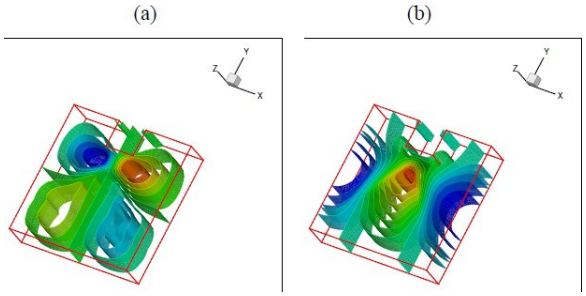


Figure 63: Contours of $u$ (a) and $v$ (b) at $t = 26.4$ produced by the present 3d diffuse interface model using a mesh of $80 \times 80 \times 16$ grid points for Re $= 10$, Ca $= 30$, Pe $= 200$, $Cn = 0.01$, $d = 0.3$, $s = 0.8$, $p = 0.2$, $w = 0.2$, $L = 1$, $\lambda_\rho = 0.001$, $\lambda_\mu = 0.001$, and $\lambda_\epsilon = 2.5$.

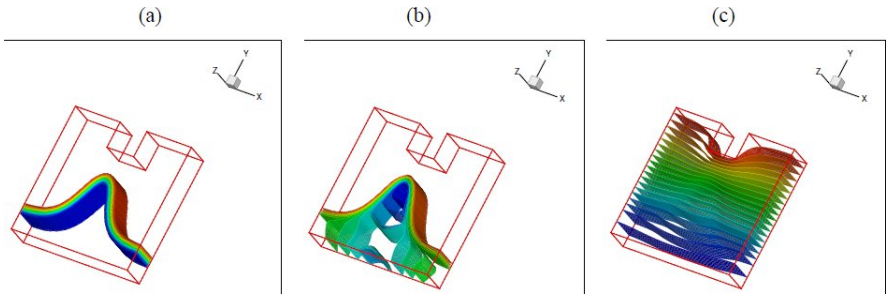


Figure 64: Contours of $c$ (a), $p$ (b), and $V$ (b) at $t = 26.4$ produced by the present 3D diffuse interface model using a mesh of $80 \times 80 \times 16$ grid points for Re $= 10$, Ca $= 30$, Pe $= 200$, $Cn = 0.01$, $d = 0.3$, $s = 0.8$, $p = 0.2$, $w = 0.2$, $L = 1$,$\lambda_\rho = 0.001$, $\lambda_\mu = 0.001$, and $\lambda_\epsilon = 2.5$.

model.

## 5.5 Simulation of 3D Newtonian film in the presence of a spatially periodic electric field.

A number of 3d simulations were also performed using the present diffuse interface model. Figures 63 and 64 show iso-surfaces of $u$ and $v$ velocity components, concentration $c$, pressure $p$, and electric potential $V$ in a representative case with Re $= 10$, Ca $= 30$, Pe $= 200$, $Cn = 0.01$, $d = 0.3$, $s = 0.8$, $p = 0.2$, $w = 0.2$, $L = 1$, $\lambda_\rho = 0.001$, $\lambda_\mu = 0.001$, and $\lambda_\epsilon = 2.5$. The computational domain was $1 \times 1 \times 0.2$ and the mesh was $80 \times 80 \times 16$. The magnitude of the spanwise velocity component $w$ was smaller than $10^{-10}$, indicating that for the present geometric arrangement and configuration the flow can be considered two-dimensional.

## 5.6 Conclusions

The development of a Navier-Stokes/Cahn-Hilliard (NS/CH) solver for the simulation of two-phase flows in the presence of electric field was described in this report. The governing equations and numerical methods were presented including constant density, variable viscosity and variable density, variable viscosity formulations. Several time-stepping algorithms, spatial discretization, the projection algorithm, and numerical details were also provided. Representative results obtained from several verification tests were shown, which exhibited a reasonably good agreement against other published results. These tests included damped oscillations of a capillary wave between two superposed viscous fluids with the same dynamic viscosity, Rayleigh-Taylor instability, the rise of a gas bubble in a liquid, and the two-dimensional (2d) and three-dimensional (3d) two-phase flow of Newtonian film in the presence of a spatially periodic electric field. In order to improve the efficiency of the present 2d/3d diffuse interface model, the implementation of multigrid solvers, parallelization (MPI, OpenMP), and adaptive mesh refinement are suggested.

# References


[1] H. Chang, Wave evolution on a falling film, Annual review of fluid mechanics 26 (1) (1994) 103136.

[2] A. Oron, S. H. Davis, S. G. Bankoff, Long-scale evolution of thin liquid films, Reviews of Modern Physics 69 (3) (1997) 931980.

[3] R. V. Craster, O. K. Matar, Dynamics and stability of thin liquid films, Reviews of Modern Physics 81 (3) (2009) 1131.

[4] S. Kalliadasis, C. Ruyer-Quil, B. Sheid, M. Velarde, Falling Liquid Films, Vol. 176 of Applied Mathematical Sciences, Springer London, 2012.

[5] T. B. Benjamin, Wave formation in laminar flow down an inclined plane, Journal of Fluid Mechanics 2 (1957) 554–573.

[6] C.-S. Yih, Stability of liquid flow down an inclined plane, Physics of Fluids 6 (1963) 321–334.

[7] R. E. Kelly, D. A. Goussis, S. P. Lin, F. K. Hsu, The mechanism for surface wave instability in film flow down an inclined plane, Phys. Fluids A 1 (1989) 819.

[8] M. K. Smith, The mechanism for the long-wave instability in thin liquid films, J. Fluid Mech. 217 (1990) 469–485.

[9] E. J. Hinch, A note on the mechanism of the instability at the interface between two shearing fluids, J. Fluid Mech. 144 (1984) 463–465.

[10] J. Liu, J. D. Paul, J. P. Gollub, A note on the mechanism of the instability at the interface between two shearing fluids, J. Fluid Mech. 250 (1993) 69–101.

[11] A. Georgantaki, J. Vatteville, M. Vlachogiannis, V. Bontozoglou, Measurements of liquid film flow as a function of fluid properties and channel width: Evidence for surface-tension-induced long-range transverse coherence, Phys. Rev. E 84 (2011) 026325. doi:10.1103/PhysRevE.84.026325.

[12] T. Pollak, A. Haas, N. Aksel, Side wall effects on the instability of thin gravity-driven filmsfrom long-wave to short-wave instability, Phys. Fluids 23 (2011) 094110.

[13] M. Hameed, M. Siegel, Y. Young, J. Li, M. Booty, D. Papageorgiou, Influence of insoluble surfactant on the deformation and breakup of a bubble or thread in a viscous fluid, Journal of Fluid Mechanics 594 (2008) 307–340.

[14] D. Conroy, O. Matar, R. Craster, D. Papageorgiou, Breakup of an electrified viscous thread with charged surfactants, Physics of Fluids 23 (2) (2011) 022103.

[15] R. E. Emmert, P. R. L., A study of gas absorption in falling liquid films, Chem. Eng. Prog. (1954) 87–93.

[16] C. Stirba, D. M. Hurt, Turbulence in falling liquid films, AIChE Journal 1 (2) (1955) 178184.

[17] S. R. Tailby, S. Portalski, The optimum concentration of surface active agents for the suppression of ripples, Trans. Inst. Chem. (1961) 328–336.

[18] S. Whitaker, Effect of surface active agents on the stability of falling liquid films, Industrial & Engineering Chemistry Fundamentals 3 (2) (1964) 132–142.

[19] T. B. Benjamin, Arch. Mech. Stos. 16 (1964) 615.

[20] S. Whitaker, L. O. Jones, Stability of falling liquid films. effect of interface and interfacial mass transport, AIChE Journal 12 (3) (1966) 421431.

[21] S. P. Lin, Stabilizing effects of surface-active agents on a film flow, AIChE Journal 16 (3) (1970) 375379.

[22] B. E. Anshus, A. Acrivos, The effect of surface active agents on the stability characteristics of falling liquid films, Chemical Engineering Science 22 (3) (1967) 389393.

[23] W. J. Strobel, S. Whitaker, The effect of surfactants on the flow characteristics of falling liquid films, AIChE Journal 15 (4) (1969) 527532.

[24] R. L. Cerro, S. Whitaker, Entrance region flows with a free surface: the falling liquid film, Chemical Engineering Science 26 (6) (1971) 785798.

[25] W. Ji, F. Setterwall, On the instabilities of vertical falling liquid films in the presence of surface-active solute, J. Fluid Mech. 278 (1994) 297–323.

[26] S. G. Yiantsios, B. G. Higgins, A mechanism of marangoni instability in evaporating thin liquid films due to soluble surfactant, Phys. Fluids 22 (2010) 022102.

[27] V. Y. Shkadov, M. G. Velarde, V. P. Shkadova, Falling films and the marangoni effect, Physical Review E 69 (5) (2004) 056310.

[28] C. Pozrikidis, Effect of surfactants on film flow down a periodic wall, Journal of Fluid Mechanics 496 (1) (2003) 105127.

[29] M. G. Blyth, C. Pozrikidis, Effect of surfactant on the stability of film flow down an inclined plane, Journal of Fluid Mechanics 521 (2004) 241–250. doi:10.1017/S0022112004001909.

[30] H.-H. Wei, Effect of surfactant on the long-wave instability of a shear-imposed liquid flow down an inclined plane, Physics of Fluids 17 (2005) 012103.

[31] H.-H. Wei, On the flow-induced marangoni instability due to the presence of surfactant, Journal of Fluid Mechanics 544 (2005) 173.

[32] A. Pereira, S. Kalliadasis, Dynamics of a falling film with solutal marangoni effect, Physical Review E 78 (2008) 036312. doi:10.1103/PhysRevE.78.036312.

[33] A. Georgantaki, M. Vlachogiannis, V. Bontozoglou, The effect of soluble surfactants on liquid film flow, Journal of Physics: Conference Series 395 (1) (2012) 012165.

[34] H. Fruhner, K.-D. Wantke, K. Lunkenheimer, Relationship between surface dilational properties and foam stability, Colloids and Surfaces A: Physicochemical and Engineering Aspects 162 (1999) 193–202.

[35] B. D. Edmonstone, R. V. Craster, O. K. Matar, Surfactant-induced fingering phenomena beyond the critical micelle concentration, Journal of Fluid Mechanics 564 (2006) 105–138. doi:10.1017/S0022112006001352.

[36] G. Karapetsas, R. V. Craster, O. K. Matar, On surfactant-enhanced spreading and superspreading of liquid drops on solid surfaces, Journal of Fluid Mechanics 670 (2011) 5–37. doi:10.1017/S0022112010005495.

[37] G. Karapetsas, R. V. Craster, O. K. Matar, Surfactant-driven dynamics of liquid lenses, Physics of Fluids 23 (12) (2011) 122106. doi:doi:10.1063/1.3670009.

[38] D. A. Edwards, H. Brenner, D. T. Wasan, Interfacial Transport Processes and Rheology, Butterworth-Heinemann, 1991.

[39] A. Sheludko, Thin liquid films, Adv. Colloid Interface Sci. 1 (1967) 391–464.

[40] D. P. Gaver, J. B. Grotberg, The dynamics of a localized surfactant on a thin film, Journal of Fluid Mechanics 213 (1990) 127–148. doi:10.1017/S0022112090002257.

[41] O. E. Jensen, J. B. Grotberg, The spreading of heat or soluble surfactant along a thin liquid film, Physics of Fluids A: Fluid Dynamics 5 (1993) 58. doi:10.1063/1.858789.

[42] G. Karapetsas, J. Tsamopoulos, On the stick-slip flow from slit and cylindrical dies of a Phan-Thien and Tanner fluid model. II. Linear stability analysis, Physics of Fluids 25 (9) (2013) 093105.

[43] A. Pereira, S. Kalliadasis, On the transport equation for an interfacial quantity, Eur. Phys. J. Appl. Phys. 44 (2008) 211–214. doi:10.1051/epjap:2008103.

[44] D. J. Benney, Long waves on liquid films, J. Math. Phys. 45 (1966) 150.

[45] S. Y. Chou, L. Zhuang, Lithographically induced self-assembly of periodic polymer micropillar arrays, Journal of Vacuum Science & Technology B: Microelectronics and Nanometer Structures 17 (6) (1999) 31973202.

[46] E. Schäffer, T. Thurn-Albrecht, T. P. Russell, U. Steiner, Electrically induced structure formation and pattern transfer, Nature 403 (6772) (2000) 874–877.

[47] E. Schäffer, T. Thurn-Albrecht, T. P. Russell, U. Steiner, Electrohydrodynamic instabilities in polymer films, Europhysics Letters (EPL) 53 (4) (2001) 518–524.

[48] Z. Lin, T. Kerle, S. M. Baker, D. A. Hoagland, E. Schäffer, U. Steiner, T. P. Russell, Electric field induced instabilities at liquid/liquid interfaces, The Journal of Chemical Physics 114 (5) (2001) 2377.

[49] Z. Lin, T. Kerle, T. P. Russell, E. Schäffer, U. Steiner, Structure formation at the interface of Liquid/Liquid bilayer in electric field, Macromolecules 35 (10) (2002) 3971–3976.

[50] M. D. Morariu, N. E. Voicu, E. Schäffer, Z. Lin, T. P. Russell, U. Steiner, Hierarchical structure formation and pattern replication induced by an electric field, Nature Mater. 2 (1) (2003) 48–52.

[51] L. F. Pease, W. B. Russel, Linear stability analysis of thin leaky dielectric films subjected to electric fields, Journal of Non-Newtonian Fluid Mechanics 102 (2) (2002) 233–250.

[52] V. Shankar, A. Sharma, Instability of the interface between thin fluid films subjected to electric fields, J. Colloid Interface Sci. 274 (2004) 294–308.

[53] J. Heier, J. Groenewold, U. Steiner, Pattern formation in thin polymer films by spatially modulated electric fields, Soft Matter 5 (2009) 3997.

[54] R. V. Craster, O. K. Matar, Electrically induced pattern formation in thin leaky dielectric films, Phys. Fluids 17 (2005) 032104.

[55] D. Merkt, A. Pototsky, M. Bestehorn, U. Thiele, Long-wave theory of bounded two-layer films with a free liquid-liquid interface: Short- and long-time evolution, Phys. Fluids 17 (2005) 064104.

[56] R. Verma, A. Sharma, K. Kargupta, J. Bhaumik, Electric field induced instability and pattern formation in thin liquid films, Langmuir 21 (8) (2005) 3710–3721.

[57] N. Wu, L. F. Pease, W. B. Russel, Electric-field-induced patterns in thin polymer films: weakly nonlinear and fully nonlinear evolution, Langmuir 21 (26) (2005) 12290–12302.

[58] N. Wu, W. B. Russel, Dynamics of the formation of polymeric microstructures induced by electrohydrodynamic instability, Applied Physics Letters 86 (24) (2005) 241912.

[59] D. Bandyopadhyay, A. Sharma, Electric field induced instabilities in thin confined bilayers, Journal of Colloid and Interface Science 311 (2) (2007) 595–608.

[60] D. Bandyopadhyay, A. Sharma, U. Thiele, P. D. S. Reddy, Electric-field-induced interfacial instabilities and morphologies of thin viscous and elastic bilayers, Langmuir 25 (16) (2009) 91089118.

[61] P. D. S. Reddy, D. Bandyopadhyay, A. Sharma, Self-organized ordered arrays of core-shell columns in viscous bilayers formed by spatially varying electric fields, The Journal of Physical Chemistry C 114 (49) (2010) 21020–21028.

[62] S. A. Roberts, S. Kumar, Electrohydrodynamic instabilities in thin liquid trilayer films, Physics of Fluids 22 (12) (2010) 122102.

[63] P. D. S. Reddy, D. Bandyopadhyay, A. Sharma, Electric-field-induced instabilities in thin liquid trilayers confined between patterned electrodes, The Journal of Physical Chemistry C 116 (43) (2012) 2284722858.

[64] S. A. Roberts, S. Kumar, AC electrohydrodynamic instabilities in thin liquid films, Journal of Fluid Mechanics 631 (2009) 255.

[65] P. Gambhire, R. M. Thaokar, Linear stability analysis of electrohydrodynamic instabilities at fluid interfaces in the small feature limit, The European Physical Journal E 34 (8) (2011) 1–12.

[66] L. Wu, S. Chou, Electrohydrodynamic instability of a thin film of viscoelastic polymer underneath a lithographically manufactured mask, Journal of Non-Newtonian Fluid Mechanics 125 (2-3) (2005) 91–99.

[67] G. Tomar, V. Shankar, A. Sharma, G. Biswas, Electrohydrodynamic instability of a confined viscoelastic liquid film, Journal of Non-Newtonian Fluid Mechanics 143 (2-3) (2007) 120–130.

[68] L. Espín, A. Corbett, S. Kumar, Electrohydrodynamic instabilities in thin viscoelastic films  AC and DC fields, Journal of Non-Newtonian Fluid Mechanics 196 (2013) 102–111.

[69] D. Bandyopadhyay, P. Dinesh Sankar Reddy, A. Sharma, Electric field and van der waals force induced instabilities in thin viscoelastic bilayers, Physics of Fluids 24 (7) (2012) 074106–074106–29.

[70] L. F. Pease, W. B. Russel, Electrostatically induced submicron patterning of thin perfect and leaky dielectric films: A generalized linear stability analysis, The Journal of Chemical Physics 118 (8) (2003) 3790–3803.

[71] L. F. Pease, W. B. Russel, Limitations on length scales for electrostatically induced submicrometer pillars and holes, Langmuir 20 (3) (2004) 795–804.

[72] D. Kim, W. Lu, Interface instability and nanostructure patterning, Computational Materials Science 38 (2) (2006) 418–425.

[73] H. K. Yeoh, Q. Xu, O. A. Basaran, Equilibrium shapes and stability of a liquid film subjected to a nonuniform electric field, Physics of Fluids 19 (11) (2007) 114111.

[74] Q. Yang, B. Q. Li, Y. Ding, A numerical study of nanoscale electrohydrodynamic patterning in a liquid film, Soft Matter 9 (2013) 3412.

[75] H. Li, W. Yu, L. Zhang, Z. Liu, K. E. Brown, E. Abraham, S. Cargill, C. Tonry, M. K. Patel, C. Bailey, M. P. Desmulliez, Simulation and modelling of sub-30 nm polymeric channels fabricated by electrostatic induced lithography, RSC Advances 3 (2013) 11839.

[76] N. Phan-Thien, R. I. Tanner, A new constitutive equation derived from network theory, Journal of Non-Newtonian Fluid Mechanics 2 (4) (1977) 353–365.

[77] N. Phan-Thien, A nonlinear network viscoelastic model, Journal of Rheology 22 (3) (1978) 259–283.

[78] D. Rajagopalan, R. C. Armstrong, R. A. Brown, Finite element methdos for calculation of steady, viscoelastic flow using constitutive equations with a newtonian viscosity, Journal of Non-Newtonian Fluid Mechanics 36 (1990) 159192.

[79] R. A. Brown, M. J. Szady, P. J. Northey, R. C. Armstrong, On the numerical stability of mixed finite-element methods for viscoelastic flows governed by differential constitutive equations, Theoretical and Computational Fluid Dynamics 5 (2) (1993) 77106.

[80] G. Karapetsas, J. Tsamopoulos, Steady extrusion of viscoelastic materials from an annular die, J. Non Newt. Fluid Mech. 154 (2008) 136152.

[81] G. Karapetsas, J. Tsamopoulos, On the stick-slip flow from slit and cylindrical dies of a phan-thien and tanner fluid model. i. steady state, Physics of Fluids 21 (12) (2009) 123101.

[82] G. Karapetsas, J. Tsamopoulos, Transient squeeze flow of viscoplastic materials, J. Non Newt. Fluid Mech. 133 (2006) 35–56.

[83] J. Papaioannou, G. Karapetsas, Y. Dimakopoulos, J. Tsamopoulos, Injection of a viscoplastic material inside a tube or between two parallel disks: Conditions for wall detachment of the advancing front, Journal of Rheology 53 (5) (2009) 1155–1191.

[84] G. Karapetsas, O. K. Matar, P. Valluri, K. Sefiane, Convective rolls and hydrothermal waves in evaporating sessile drops, Langmuir 28 (31) (2012) 11433–11439.

[85] K. Tsiveriotis, R. A. Brown, Boundary-conforming mapping applied to computations of highly deformed solidification interfaces, International Journal for Numerical Methods in Fluids 14 (8) (1992) 9811003.

[86] K. Christodoulou, L. Scriven, Discretization of free surface flows and other moving boundary problems, Journal of Computational Physics 99 (1) (1992) 39–55.

[87] Y. Dimakopoulos, J. Tsamopoulos, A quasi-elliptic transformation for moving boundary problems with large anisotropic deformations, Journal of Computational Physics 192 (2) (2003) 494522.

[88] N. Chatzidai, A. Giannousakis, Y. Dimakopoulos, J. Tsamopoulos, On the elliptic mesh generation in domains containing multiple inclusions and undergoing large deformations, Journal of Computational Physics 228 (6) (2009) 1980–2011.

[89] N. Wu, M. E. Kavousanakis, W. B. Russel, Coarsening in the electrohydrodynamic patterning of thin polymer films, Phys. Rev. E 81 (2010) 020306.

[90] A. N. Brooks, T. J. Hughes, Streamline upwind/Petrov-Galerkin formulations for convection dominated flows with particular emphasis on the incompressible navier-stokes equations, Computer Methods in Applied Mechanics and Engineering 32 (13) (1982) 199–259.

[91] N. Wu, W. B. Russel, Micro- and nano-patterns created via electrohydrodynamic instabilities, Nanotoday 4 (2009) 180–192.

[92] M. D. Dickey, S. Gupta, K. A. Leach, E. Collister, C. G. Willson, T. P. Russell, Novel 3-d structures in polymer films by coupling external and internal fields, Langmuir 22 (9) (2006) 4315–4318.

[93] K. A. Leach, S. Gupta, M. D. Dickey, C. G. Willson, T. P. Russell, Electric field and dewetting induced hierarchical structure formation in polymer/polymer/air trilayers, Chaos: An Interdisciplinary Journal of Nonlinear Science 15 (4) (2005) 047506.

[94] D. Bandyopadhyay, A. Sharma, V. Shankar, Electric-field and contact-forceinduced tunable patterns in slipping soft elastic films, EPL (Europhysics Letters) 89 (2010) 36002.

[95] G. Karapetsas, V. Bontozoglou, Non-linear dynamics of a viscoelastic film subjected to a spatially periodic electric field, Journal of Non-Newtonian Fluid Mechanics 217 (2015) 1–13.

[96] J. Kim, K. Kang, J. Lowengrub, Conservative multigrid methods for cahn–hilliard fluids, Journal of Computational Physics 193 (2004) 511–543.

[97] J. Kim, A continuous surface tension force formulation for diffuse-interface models, Journal of Computational Physics 204 (2005) 784–804.

[98] A. Prosperetti, Motion of two superposed viscous fluids, Phys. Fluids 24 (1981) 1217–1223.

[99] D. Gueyffier, J. Li, A. Nadim, R. Scardovelli, Z. S., Volume-of-fluid interface tracking with smoothed surface stress methods for three-dimensional flows, J. Comput. Phys. 152 (199) 423–456.

[100] G. Tryggvason, Numerical simulations of the rayleigh–taylor instability, J. Comput. Phys. 75 (1988) 253–282.

[101] J. Guermond, L. Quartapelle, A projection fem for variable density incompressible flows, J. Comput. Phys. 165 (2000) 167–188.

[102] H. Ding, P. Spelt, C. Shu, Diffuse interface model for incompressible two-phase flows with large density ratios, J. Comput. Phys. 226 (2007) 2078–2095.

[103] M. Sussman, P. Smereka, S. Osher, A level set approach for computing solutions to incompressible two-phase flow, J. Comput. Phys. 114 (1994) 146–159.

[104] E. Fadlun, R. Verzicco, P. Orlandi, J. Mohd-Yusof, Combined immersed boundary finite difference methods for three-dimensional complex flow simulations, J. Comput. Phys. 161 (200) 35–60.